Modelling And Data Analysis of Protein Dynamics applied to a Fission Yeast Mechanosensor

Enrico Lorenzetti

INSTITUT POLYTECHNIQUE DE PARIS

NNT : 2024IPPAX093

Thèse de doctorat

ÉCOLE POLYTECHNIQUE

IP PARIS

Modelling and Data Analysis of Protein Dynamics Applied to a Fission Yeast Mechanosensor

Thèse de doctorat de l'Institut Polytechnique de Paris
préparée à l'École polytechnique

École doctorale n°626 École doctorale de l'Institut Polytechnique de Paris (EDIPP)
Spécialité de doctorat : Mécanique des fluides et des solides, acoustique

Thèse présentée et soutenue à Palaiseau, le 5 Novembre 2024, par

ENRICO LORENZETTI

Composition du Jury :

Catherine Villard Directrice de Recherche, Université Paris Cité (LIED)	Presidente
François Graner Directeur de Recherche, Université Paris Cité (MSC)	Rapporteur
Karin John Chargée de Recherche, Université Grenoble Alpes (LiPhy)	Rapporteure
Martin Genet Professeur, École Polytechnique (LMS)	Examinateur
Arezki Boudaoud Professeur, École Polytechnique (LadHyX)	Directeur de thèse
Antoine Fruleux Chargé de Recherche, Université Paris-Saclay (LPTMS)	Co-directeur de thèse

ABSTRACT IN ENGLISH

Intracellular dynamics is fundamental for cells to maintain homeostasis and respond to environmental stimuli. Among these, mechanical forces can be a potential source of damage as they can compromise the integrity of the cell. To cope with this risk, living organisms are endowed with mechanosensors, i.e. receptor at the sub-cellular level able to trigger a biological pathway by a mechanical signal. In fission yeast, a mechanosensor, Wsc1 protein, perceives excessive stress on the cell wall and activates the glucan synthesis to keep this layer reinforced. More interestingly, Wsc1 concentration increases in the compressed region of the cell wall forming clusters. This work investigates this mechanosensitive clustering behaviour by advancing models and inference method for experimental data of protein dynamics.

By setting a mathematical framework based on deterministic partial differential equations, I describe the Wsc1 dynamics along the cell wall. In this model, I consider two possible protein recruitment mechanisms for shaping clusters, either from the sides due to diffusion along the cell wall and from the cytoplasm by exocytotosis. Moreover, following chemical considerations, I suppose an affinity between the cell wall and the protein that increases with the cell wall compression. The resulting reaction-diffusion equations obtained by this model are able to reproduce the clustering behaviour after cell wall compression. In addition, the model correctly predicts a longer time-scale of the dynamics in the compressed region of the cell wall. This result is in agreement with the outcomes of FRAP (Fluorescence Recovery After Photobleaching) experiment, whose analysis is based on the study of time-lapse images that reflects the spatial-temporal concentration of the molecule.

However, it is not clear yet if the protein recruitment is due to diffusion, exchange with cytoplasm, or both. For this reason, in my work I also develop a new inference method for FRAP experiment capable of discerning different types of dynamics. My analysis aims at quantifying kinetic parameters, such as diffusion coefficient and exchange rate, by minimising the distance between the reaction-diffusion model prediction and actual data. The specificity of my approach is the use of dimensional reduction to efficiently perform computation without having knowledge of the initial bleached profile. This new method is then tested and validated on artificial data. The results show that this analysis is flexible since it can work with imperfect data, where the signal-to-noise ratio is low, the number of frames is reduced and the spatial window is restricted. Moreover, this approach can be potentially generalised to complex geometries, for instance curved surface. This versatility is well-suited for studying protein dynamics in the fission

yeast cell wall. The inference method is applied to experimental data of another mechanosensor in the cell wall, Mtl2, yielding reasonable values of diffusion coefficient. Nevertheless, it still needs to be tested on real data of Wsc1 protein. Overall, this study offers novel methodologies for quantifying and understanding intricate protein dynamics within cells and tissues.

ABSTRACT IN FRENCH

La dynamique intracellulaire des molécules est fondamentale pour que les cellules maintiennent l'homéostasie et répondent aux stimuli environnementaux. Parmi ceux-ci, les forces mécaniques peuvent constituer une source potentielle de dommages en compromettant l'intégrité de la cellule. Pour faire face à ce risque, les organismes vivants sont dotés de mécanosenseurs, des récepteurs subcellulaires capables de déclencher une voie de signalisation biologique par un signal mécanique. Chez la levure à fission fissipare, un mécanosenseur, la protéine Wsc1, peut percevoir une contrainte excessive sur la paroi cellulaire et activer la synthèse de glucane pour renforcer la paroi. Notablement, la concentration de Wsc1 augmente dans la région comprimée de la paroi, formant des agrégats. Ce travail de thèse explore ce comportement de formation d'agrégat mécanosensible en développant des modèles et des méthodes d'inférence pour les données expérimentales de dynamique des protéines. En établissant un cadre mathématique basé sur des équations aux dérivées partielles déterministes, je décris la dynamique de Wsc1 le long de la paroi cellulaire. Dans ce modèle, je considère deux mécanismes possibles de recrutement des protéines pour former des agrégats : soit par diffusion le long de la paroi cellulaire, soit par exocytose depuis le cytoplasme. De plus, en suivant des considérations chimiques, je suppose que l'affinité entre la paroi et la protéine Wsc1 augmente avec la compression de la paroi. Les équations de réaction-diffusion résultant de ce modèle reproduisent la formation d'agrégats après compression de la paroi cellulaire. De plus, le modèle prédit une échelle de temps plus longue pour la dynamique dans la région comprimée de la paroi cellulaire, en accord avec les résultats de l'expérience FRAP (*Fluorescence Recovery After Photobleaching*, redistribution de fluorescence après photoblanchiment), dont l'analyse est basée sur l'étude des images en temps réel reflétant la concentration spatio-temporelle de la molécule. Cependant, il n'est pas encore clair si le recrutement des protéines est dû à la diffusion, à l'échange avec le cytoplasme, ou aux deux. Pour cette raison, dans mon travail, je développe également une nouvelle méthode d'inférence pour l'expérience FRAP capable de distinguer différents types de dynamique. Mon analyse vise à quantifier les paramètres cinétiques, tels que le coefficient de diffusion et le taux d'échange, en minimisant la distance entre la prédiction du modèle de réaction-diffusion et les données réelles, en faisant varier les valeurs des paramètres cinétiques. La spécificité de mon approche réside dans l'utilisation de la réduction dimensionnelle pour calculer efficacement les paramètres sans avoir connaissance du profil initial après photoblanchiment, dont la forme n'est pas exactement contrôlée par les expérimentateurs. Cette nouvelle méthode est ensuite testée et validée sur des données artificielles générées par des

simulations. Les résultats montrent que cette méthode d'analyse est flexible, car elle peut fonctionner avec des données imparfaites où le rapport signal/bruit est faible, le nombre d'images est réduit et la fenêtre spatiale est restreinte. De plus, cette approche peut potentiellement être généralisée à des géométries complexes, telles que les surfaces courbées. Cette polyvalence est bien adaptée pour étudier la dynamique des protéines dans la paroi cellulaire de la levure fissipare. La méthode d'inférence est appliquée aux données expérimentales d'un autre mécanosenseur dans la paroi cellulaire, Mtl2, fournissant des valeurs raisonnables de coefficient de diffusion. Cependant, elle doit encore être testée sur des données réelles de la protéine Wsc1.
Dans l'ensemble, cette étude propose des méthodologies novatrices pour quantifier et comprendre la dynamique complexe des protéines au sein des cellules et des tissus, adéquates pour mieux comprendre comment les forces mécaniques au niveau subcellulaire peuvent affecter la mobilité des molécules.

ACKNOWLEDGMENTS

This work marks the culmination of a three-year journey through my IP Paris doctoral program. During this period, I conducted research between two laboratories, LadHyX (École Polytechnique) and LPTMS (Université Paris-Saclay). In these places, I have had the privilege of meeting and sharing experiences with many incredible people. Their support, friendship, and shared moments have enriched this part of my life. I am grateful for all the memories and connections we have created together.

First and foremost, I would like to express my deep gratitude to my supervisor and co-supervisor, Arezki Boudaoud and Antoine Fruleux, for giving me the opportunity to experience the world of scientific research. Their guidance, support, and encouragement throughout my Ph.D. have been invaluable, and I am profoundly grateful for their mentorship. Their insightful advice and willingness to answer all my questions and concerns with patience and precision were always present. Our shared passion for scientific discussion enabled us to overcome many challenges together.
Next, I would like to thank my collaborators, Celia and Nicola. Working with them was a pleasure and I greatly benefited from their experimental expertise, which enriched my understanding and significantly contributed to our research.
Afterward, I would like to thank those who enhanced this manuscript: the reviewers, François Graner and Karin John, as well as the other members of the jury, Catherine Villard and Martin Genet. Thanks to their valuable feedback, the quality of this work has improved significantly.
Moreover, I would like to thank all the members of both my laboratories, LadHyX and LPMS. In particular, the administrative heads of the labs, respectively, Sandrine and Claudine, for efficient assistance in many practical aspects.
At LadHyX, I want to extend my heartfelt thanks to the wonderful students and colleagues I had the privilege of working alongside. I am particularly grateful to my officemates—Olivier, Pierre-Antoine, Valentin, Anis, Datong and Vincent—who made every day enjoyable. I also deeply appreciate all the members of Arezki's group: Elise, Abdilah, Ana, Stéphanie, Jordan and Doron. This laboratory provided an incredible environment where diverse backgrounds, ranging from biology to physics, came together to inspire and enrich each other. It was truly a unique and stimulating place to work and grow.
LPTMS was no less exceptional. I want to thank my office mates Federico, Vincenzo, Alireza and João for their constant support and positive energy they brought to our workspace. Beyond our friendship, I must also acknowledge that

many new ideas for the project emerged from the stimulating discussions and brainstorming sessions we shared.

I also want to thank two special professors who have been determinant to orient my research towards biophysics. My professor in Padua, Enzo Orlandini, with whom I work for my Bachelor and Master degree, and my professor in Strasbourg, Daniel Riveline, head of the interdisciplinary master Cell Physics, where I spent 6 months thanks to the Erasmus+ studio program.

Beyond scientific research, these years were also dedicated to continuing my hobbies, such as football. I would like to thank all the CSX members at École Polytechnique, in particular Daniel, Jean-François, Sami, Taha and Thomas, for the joyous matches we played together.

Moreover, I would like to thank my dear friends in Verona, Davide, Francesco, Nicolò and Andrea. Despite being long-distance, we always get in touch and organize trips together spending really nice moments. A special thanks also goes to Father Giampaolo, who gave me a DVD about string theory when I was a child, sparking my fascination with the science of nature. In addition, I thank him and all the Cambonian community for hosting me and my friends in Padua during my last summer holidays, where this manuscript was conceived.

To conclude, I thank my family for their unwavering support, love, and belief in me, which have been my greatest strength and encouragement. And finally, I want to thank my soulmate, Martina.

Per l'amore dei miei nonni, Mario e Albino

CONTENTS

INTRODUCTION

Intracellular dynamics play a fundamental role in life by facilitating vital processes involved in the maintenance of homeostasis or in response to environmental stimuli like mechanical forces (Municio-Diaz et al., 2022). From the movement of molecules and ions across membranes to vesicle trafficking, motion inside the cell is fundamental in regulating many cellular activities (Buda et al., 2016; Martinac, 2004). Concerning proteins, dynamics is crucial for their proper functioning and is intimately linked to their structure. From changes in a protein's single conformation to the collective behavior of entire domains, the description of protein dynamics can encompass a wide range of kinetics and timescales (Nam and Wolf-Watz, 2023). To obtain quantitative insights into these biological phenomena, new experimental techniques have recently been designed (Ferrand et al., 2011; Lippincott-Schwartz et al., 2018). However, the data generated from these experiments can be complex and present challenges in interpretation. Thus, a thorough understanding of the underlying biological processes is crucial in order to advance the development of models and protocols for data analysis.

In this work, conducted in collaboration with Minc's Lab at the Institute Jacques Monod, I present a study on the dynamics of a particular protein in fission yeast cell wall (CW), Wsc1. The latter is considered from recent research as a putative mechanosensor, i.e. a receptor at the subcellular level which is able to translate a mechanical signal, in this case of stress or compression on the CW, into a biological pathway. More interestingly, the protein seems to exhibit a clustering behavior triggered by mechanical forces. This phenomenon is the focus of our investigation. By setting a mathematical model to describe the protein dynamics, I would like to shed new light on the fundamental biological mechanisms underlying this collective motion. Moreover, by the analysis of experimental data, I would like to test the predictions of the model on the mobility of the proteins, which is expected to be related to the mechanosensitive clustering capability of the protein.

The following manuscript is structured into four chapters.
The first two chapters review the literature. In particular, in the first chapter, I present an overview of the various types of molecular movements within the cell and examine the dynamic nature of molecular behavior, which can change in response to external stimuli. Moreover, I present experimental techniques to study intracellular dynamics.
In the second chapter, which also reviews the literature, I describe the importance of mechanosensing, the ability of living organisms to perceive mechanical cues,

and I present an example of protein dynamics that was recently discovered to be sensitive to mechanical signals (Neeli-Venkata et al., 2021). This protein, Wsc1, is localized on the fission yeast cell wall, and it can form clusters as the cell wall get compressed. At the end of this chapter, I expose the motivations and challenges of my PhD project.
The following chapters, 3 and 4, describe my three-year work focused on developing theoretical models and data analysis methods. These tools aim to help experimentalists gain quantitative insights into protein dynamics and better understand the processes behind Wsc1 clustering. In particular, in chapter 3, I present my research on theoretical modelling of Wsc1 dynamics, which further develops the work from my master's thesis (Lorenzetti, 2021). The mathematical model is based on protein-cell-wall interaction and is able to predict the experimental observations on Wsc1 clustering. However, the current analysis methods are not able to test my model with FRAP experiments to discern different mechanisms of protein recruitment to form the clusters, either from lateral diffusion along the cytoplasm, or by exchange with the cytoplasm, due to the absence of an appropriate method to infer the kinetic parameters.
For this reason, in chapter 4, I develop a novel and versatile inference method on FRAP experiment, which is able to discern the different molecule dynamics inside the cell, even with significant experimental limitations. This method is tested on artificial data, generated by simulations of the diffusion-exchange model, and experimental data yielded by the Minc's lab.

CHAPTER

ONE

INTRACELLULAR DYNAMICS: THEORY AND EXPERIMENTS

In this chapter, I review the literature to explore various types of molecular dynamics within the cell, ranging from passive transport, such as thermal diffusion, to active mechanisms driven by molecular motors. Additionally, I illustrate the variability of molecular behavior, including changes in chemical states and interactions with cellular structures.
Afterward, I explain how molecular dynamics can be investigated using well-established fluorescence experimental techniques. First, I outline how fluorescence signals from molecules are emitted and detected by the associated instruments. Then, I present an important application, Fluorescence Recovery After Photobleaching (FRAP), a method used to measure the kinetic parameters of molecules. At the end, I outline the key questions and the main challenges of this thesis.

1.1 Origins of motion

1.1.1 Diffusion

It was in 1827 when the Scottish botanist Robert Brown observed pollen grains suspended in water under microscope. The scientist noted that the grains exhibited a jittery and erratic movement, which he initially attributed to some form of life activity intrinsic to the pollen. However, upon further investigation, Brown observed that this motion was also present in inanimate particles, such as dust or dead pollen, leading him to question the origin of this phenomenon.
The explanation for this seemingly random motion was not fully understood until later, when Albert Einstein and Marian Smoluchowski provided a theoretical framework (Góra, 2006; Piasecki, 2007; Renn, 2005). Based on Boltzmann's kinetic theory, both scientists proposed that the random motion of particles was the result of countless collisions between the particles and the thermally agitated molecules of the solvent. This collision-based mechanism causes the particles to move in a random manner.
Brownian motion is not limited to pollen grains observed by Brown, but it is a universal phenomenon that applies to any type of particle, with wide-ranging implications across various contexts. For example, it can describe cosmic ray dif-

fusion in the interstellar medium (Erlykin et al., 2003) or dispersion of pollutants in the air (Sharan et al., 1996) or dissolving a sugar cube in a liquid (Ferrari and Hubinger, 2008).
Similarly, Brownian motion is also present in biological systems, in particular at the cellular level. In the cytoplasm, enzymes and other larger molecules are continuously jostled by surrounding water molecules, facilitating the random interactions needed for biochemical reactions to occur efficiently (Schavemaker et al., 2018). Similarly, on the cell membrane, receptor proteins undergo Brownian motion, allowing them to encounter signaling molecules to trigger the cellular response (Radhakrishnan et al., 2012). In the nucleus, this type of motion is equally vital. DNA, RNA, and various nuclear proteins move through the nucleoplasm via diffusion. This random movement allows transcription factors to locate specific DNA sequences, RNA molecules to find ribosomes for translation, and other essential processes to occur efficiently within the highly crowded nuclear environment (Récamier, 2013).
To characterize the Brownian motion of a single particle, as the simulated trajectory in figure 1.1.1 (panel A), Einstein proposed a quantitative parameter, the mean squared displacement (MSD), which is the average of the squared distances between the initial and later time position. In the case of isotropic and homogeneous media, the MSD is linear with time as $MSD(t) = 2dDt$, where D is the so-called diffusion coefficient and d the dimension of the system.
Instead, at the population level, the concentration of particle c defined as the number of particle per solvent volume obeys Fick's law:

$$J = -D\nabla c \tag{1.1}$$

where J is the flux of particles, i.e. the number of particles that crosses a surface per unit of time, and ∇ is the gradient operator. This means that whenever a concentration difference appears, the random motion of particles will tend to create a net flux of particles from the region of higher concentration to the region of lower concentration. It is important to remark that this equation is not stochastic but deterministic, since fluctuation in the concentration are irrelevant when the number of particles considered is high. Examples of Fick's law solutions coupled with the continuity equation $\partial_t c = -\nabla \cdot J$, where ∂_t is the temporal derivative and $\nabla\cdot$ the divergence operator, are shown in figure 1.1.1 (panel B)
In special cases, D, which incorporates the interaction between the solvent and the moving particle, can be directly linked with the rheological properties of the system. For example, for a spherical particle through a liquid with low Reynolds number, D is given by Stokes-Einstein's relation (Cappelezzo et al., 2007)

$$D = \frac{k_{\mathrm{B}}T}{6\pi\nu r} \tag{1.2}$$

where k_{B} is the Boltzmann's constant, T the absolute temperature, ν the viscosity of the fluid and r the radius of the sphere.
In the biological context, a similar relation describes the diffusion of transmembrane proteins along the cell membrane (Saffman and Delbrück, 1975). Considering the lipid bilayer as a liquid sheet of viscosity ν_{l}, the surrounding environment as a liquid of lower viscosity η_{w} and the protein as a cylindrical object of radius

R and height h, as described in figure 1.1.2, it yields the following formula

$$D = \frac{k_b T}{6\pi\nu_l h} \log\left(\frac{\nu_l h}{\nu_w R} - \gamma_e\right) \tag{1.3}$$

where $\gamma_e \approx 0.577$ is the Eulero constant. In this case, the dependence on the radius is rather weak $\sim \log(\frac{1}{R})$. In more realistic modeling, where the effect of crowding or membrane tension is accounted for, a behavior similar to the Einstein relationship $D \sim \frac{1}{R}$ is found (Quemeneur et al., 2014; Javanainen et al., 2017).

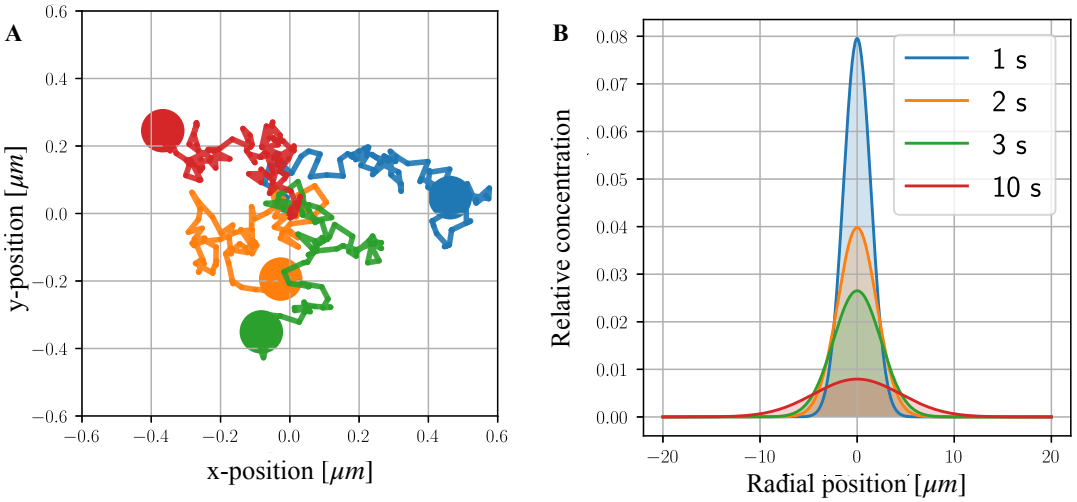

Figure 1.1.1: From single particle Brownian motion to the collective behavior. Panel A: Example of 4 simulated Brownian motion trajectories (blue, orange, green and red) with the same initial condition $(0, 0)$. The end point is marked by a circle. Panel B: Analytical solution of Fick's law for the concentration of particles subjected to Brownian motion as function of the radial distance $\sqrt{x^2 + y^2}$ sampled at different time. The spatial integral of the relative concentration is normalized to 1. The initial concentration is a point-like source at $(0, 0)$ position. The diffusion coefficient was set to $D = 1\ \mu m^2/s$

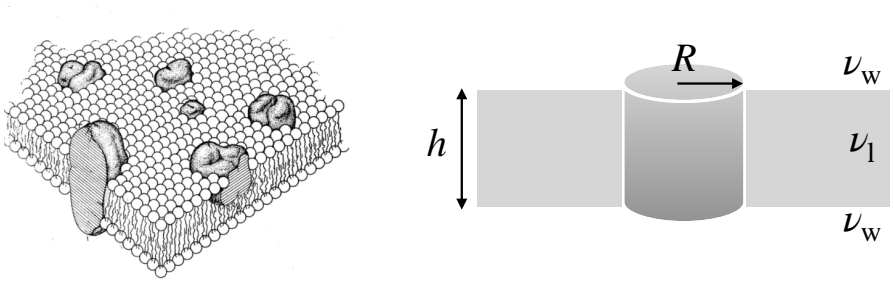

Figure 1.1.2: Transmembrane protein diffusion model. On the left: Fluid mosaic model (Singer and Nicolson, 1972) where the membrane is depicted as a liquid phospholipid bilayer with transmembrane protein inside. On the right: Saffman's model (Saffman and Delbrück, 1975) for computing the diffusion coefficient of transmembrane protein; the latter is depicted as a cylinder of radius R, height H and in contact with a liquid bilayer of viscosity ν_l and an external liquid of lower viscosity ν_w

.

To summarize, diffusion and random motion due to thermal agitation contribute to motion of all molecules, such as proteins.

1.1.2 Active transport

Although diffusion plays a crucial role in cellular processes, this motion driven only by thermal fluctuations can be too slow and inadequate for rapid and long-distance transport (Ahmed and Saif, 2014). For example, vesicles transports in neural cells, with a typical diffusion value $D \sim 1\ \mu m^2/s$ (Wojcieszyn et al., 1981), would take several hours to cover a distance of $\sim 0.1\ \mu m$, the typical axon length, if only diffusion contributed to its motion. Nevertheless, living systems are endowed with a metabolism that produces energy in the form of ATP (adenosine triphosphate) by breaking down nutrients and oxygen. Therefore, this "fuel" can be exploited for active transport mechanisms, allowing cells to move molecules efficiently (MacKintosh and Schmidt, 2010).
Molecular motors such as myosin, kinesin, and dynein are central to this process (Cai et al., 2007; Li et al., 2018; Pilling et al., 2006). These molecular machines can utilize the cytoskeleton, i.e., protein structures that constitute the cell's internal framework, to efficiently transport vesicles, organelles, and other cellular cargo within the cell. Because of the energy released by ATP hydrolysis, these molecular motors undergo a series of conformational changes that allow them to "walk" along the cytoskeleton filaments. Kinesin and dynein exploit the microtubules, rigid structures of the cytoskeleton, which enable long-range cargo transport. Kinesin generally directs the cargo toward the cell's periphery, while dynein moves it toward the cell's interior. Myosin motors operate along actin filaments, which are flexible structures that allow, for example, for short-range transport.
Figure 1.1.3 illustrates how active transport in *Aspergillus nidulans* delivers essential materials to support cell growth at the tip (Taheri-Talesh et al., 2012). This process relies on two key mechanisms: endocytosis, when materials are brought into the cell by forming vesicles from the membrane, and exocytosis, when vesicles fuse with the membrane to release their contents outside the cell. Dynein, kinesin and myosin motors transport these vesicles along cytoskeleton, ensuring that the necessary components reach the actively growing regions. These mechanisms ensure the continuous supply and recycling of materials required for cellular expansion.
In addition to molecular motors, other types of active transport rely on selective channels of molecules that consume energy to move specific substances, such as ions, across the cell membrane (Alberts et al., 2002). In passive transport, the molecules pass through this channel according to gradient concentration, moving from an area of higher concentration to an area of lower concentration, or by osmotic pressure, when the solvent molecules pass from an area of low solute concentration to an area of high solute concentration. In active transport, instead, the consumption of energy allows molecules to go against these gradients. An example of this mechanism occurs when the target molecule binds to the channel, triggering ATP to supply energy for a conformational change that moves molecules across the membrane (Cooper, 2009). This process allows the cell to generate electrochemical gradients, i.e. differences in both the molecule concentration and the electrical charge across the membrane. This process can be essential

for storing potential energy, which the cell can use to power various processes, such as signal transmission or nutrient transport. For example, the sodium-potassium pump actively transports sodium ions out of the cell and potassium ions into the cell, creating an electrochemical gradient that is crucial for nerve impulses (Skou, 1998). Similarly, proton pumps in mitochondria move hydrogen ions across the membrane, helping generate the proton concentration gradient necessary for ATP production in cellular respiration (Wikström et al., 2015).
Overall, active transport is advantageous because motion can be directed, allowing precise movement of cellular components, even against a concentration gradient (Brangwynne et al., 2009). This enables cells to achieve fast transport over long distances.

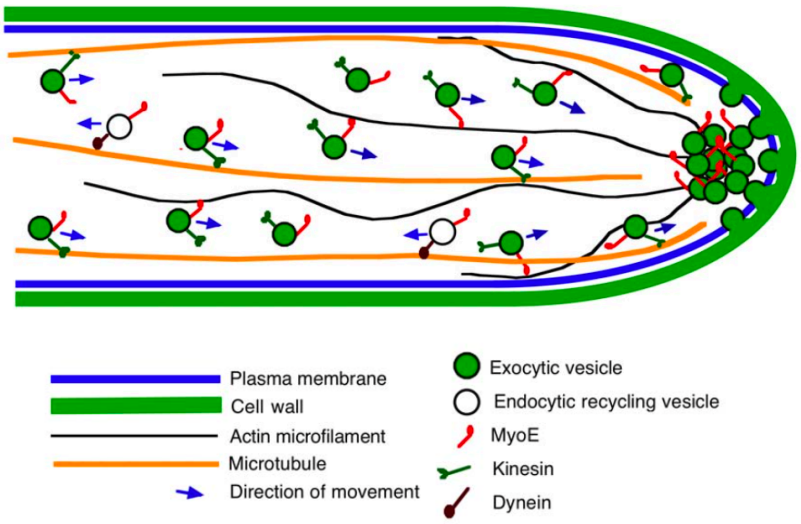

Figure 1.1.3: Active transport for exocytosis and endocytosis of vesicles. An *A. nidulans* cell, where vesicles are transported by microtubules toward the tip driven by kinesin molecules and along actin filaments by myoE, a type of myosin. At the end, the versicles reach the Spitzenkorper, an organelle important for morphogenesis. At this point, the vesicles fuse with the plasma membrane and release their contents for cell growth in the cell wall, a polymeric layer. Afterwards, the cellular components are moved in retrograde direction by dynein where they will be reused. Image taken from Taheri-Talesh et al., 2012

.

1.1.3 Chemical reaction and conformational changes

In addition to thermal agitation and active transport, the dynamics of molecules within the cell is significantly influenced by chemical reactions. For instance, different species of molecules, a ligand and a receptor, can interact to form a complex (Long et al., 2006). This interaction often results in a structure with altered mobility, such as a different diffusion coefficient. For example, when a protein binds to a specific target compound, as shown in Figure 1.1.4 (on the left), it may become immobile (Ali et al., 2011). Another example of a chemical bond can derive from protein-protein interactions, as depicted in 1.1.4 (on the right), which may lead to the formation of clusters within the cell (Greenfield et al., 2009).

These molecular interactions can arise from various forces, including electrostatic interactions between ions or covalent bonds between atoms. Covalent bonds are particularly strong, with a typical associated energy of 10^2 k_BT (Frieden, 1975). For this reason, these bonds are essential to maintaining the structural integrity of biological molecules. For example, peptide bonds link amino acids together in proteins through a covalent interaction between the carboxyl group of one amino acid and the amino group of another. This type of bond forms the backbone of proteins and ensures their stability (Berg et al., 2015). Another important covalent interaction is the disulfide bond, which forms between the sulfur atoms of two cysteine residues in proteins. Disulfide bonds play a critical role in stabilizing the three-dimensional structure of proteins, particularly those that function outside the cell, such as insulin (Qian et al., 2000).
In contrast, non-covalent interactions -such as hydrogen bonds or van der Waals forces-are weaker, with an associated energy of the order of 1 k_BT, and generally less stable and more transient (Frieden, 1975). For example, in DNA, hydrogen bonds hold the two strands of the double helix together by connecting complementary base pairs (adenine to thymine, and guanine to cytosine) (Alberts et al., 2014). These hydrogen bonds are easily broken during DNA replication, allowing the strands to separate temporarily so they can be copied. Once the process is finished, the strands re-form their hydrogen bonds. In antibody-antigen interactions, instead, Van der Waals forces help the antibody bind to the antigen (Giannini et al., 2011). When the antibody and antigen come close, weak transitory attractions form between their atoms, due to fluctuations in electron density that create temporary dipoles. These interactions are short-lived, allowing the antibody to release the antigen after it has been neutralized or marked for destruction.
It is crucial to note that interactions between molecules can be triggered by conformational changes in proteins, which are often induced by external stimuli or the binding of an effector molecule (Nam and Wolf-Watz, 2023). In fact, proteins are dynamic structures and their functions depend heavily on their three-dimensional shape. When an external signal, such as a change in pH, temperature, or the presence of a ligand, causes a protein to undergo a conformational change, it can expose or hide active sites, alter binding affinities, or enable new interactions with other molecules. These structural changes can modulate the protein's function and, in many cases, initiate or regulate key cellular processes. For example, in signal transduction pathways, the binding of a hormone or neurotransmitter to a cell surface receptor often triggers a conformational change in the receptor. This alteration can activate or deactivate the receptor, which in turn initiates a cascade of intracellular signaling events. G-protein coupled receptors (GPCRs), a family of cell surface receptors, are a well-known example of this mechanism: When a ligand binds to the GPCR, the receptor undergoes a conformational change that activates associated G-proteins, leading to downstream effects such as changes in gene expression or enzyme activity (Lebon et al., 2012). Another example of these processes is allosteric regulation, where an effector molecule binds to a site other than the enzyme's active site, causing a conformational change that enhances or inhibits the enzyme's catalytic activity. This allows for precise control of metabolic pathways, as enzymes can be regulated according to the needs of the cell (Monod et al., 1965).
These conformational changes are essential not only for initiating specific functions

but also for enabling proteins to respond dynamically to environmental changes, maintaining homeostasis within the cell.

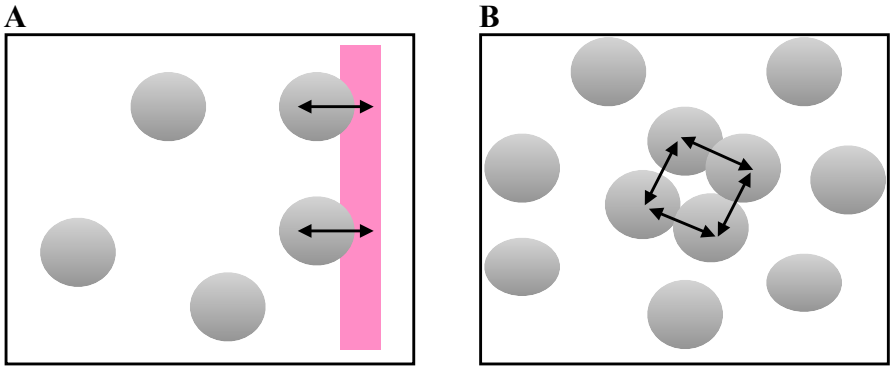

Figure 1.1.4: Examples of chemical bonds. On the left: freely diffusing molecules (in gray) form a bound (drawn with a double arrow) with a specific target compound (in pink). On the right: freely diffusing molecules can form bonds between each other and initiate a cluster.

.

To recapitulate, molecular dynamics inside the cell does not include only passive processes, such as diffusion, but it can be active and dynamic and change in relation to external stimuli.

1.2 Experimental methods

After having shown the different dynamics molecules experienced inside the cell, in the following section, I illustrate how it is possible to study these phenomena by fluorescence experiments.

1.2.1 Principle of fluorescence

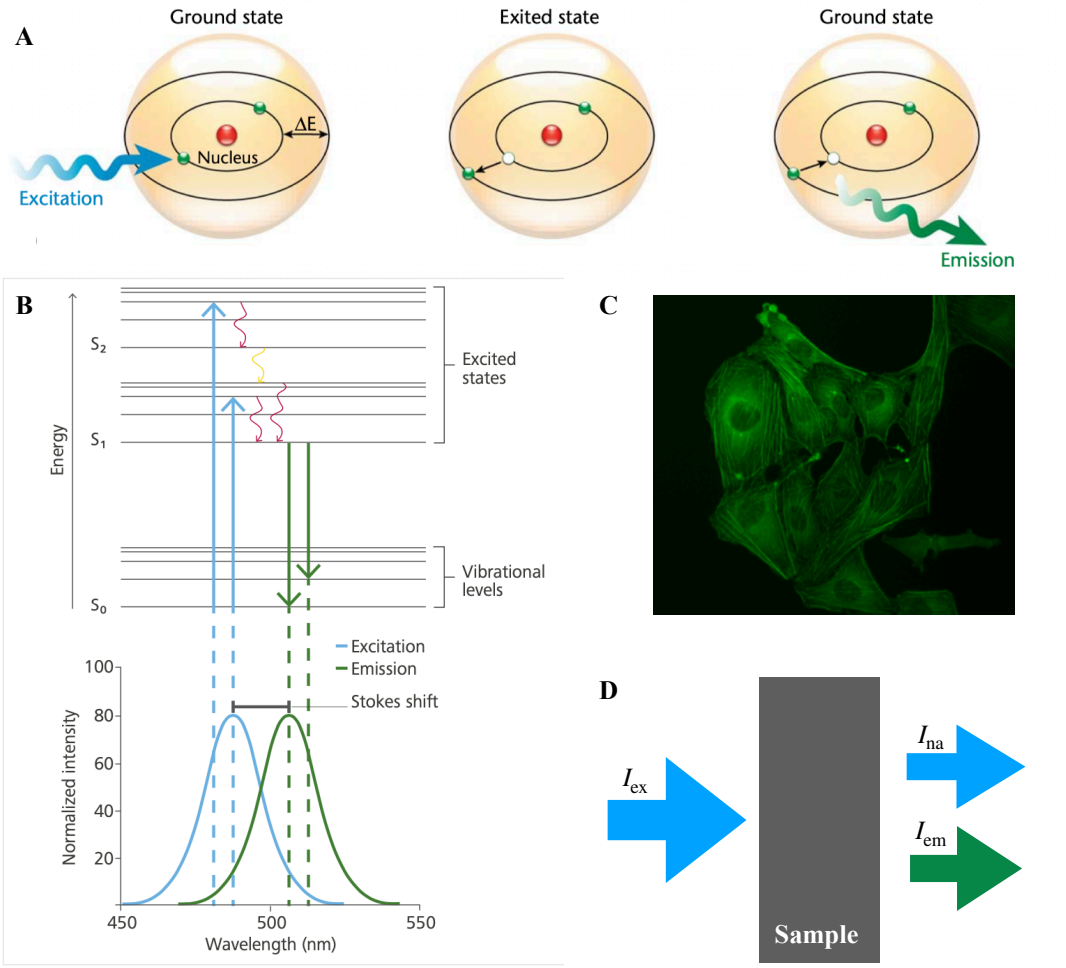

Figure 1.2.1: Principle of fluorescence. Panel A: in the classic Bohr model for an atom, electrons (green dot) are excited by incoming light (blue arrow) and make a transition to a ΔE higher energy state; as electrons relax to the ground state, they emit a photon (green arrow) causing fluorescence. Panel B: on the top it is shown the Jacobloski diagram for a GFP molecule, where different vibrational energy levels (represented by lines) are drawn for three electronic energy configurations, S_1, S_2 and S_3; after excitation at wavelength around 490 nm (in light blue), electrons first relax to lower vibrations states of the same configuration state (in red) or close configuration (in yellow) and then to the ground state; below is represented the absorption and emission spectrum, i.e. the intensity distribution as function of wavelength, highlighting the difference between emission (in light blue) and emission (in green) peaks, known as the Stoke's shift. Panel C: Fluorescence image from U2OS cells where GFP reveals actin. Panel D: Incoming light beam of intensity I_{em} which passes through the sample causing an emission of fluorescent light of intensity I_{em}; I_{na} is the light intensity which is not absorbed by the sample. Images are adapted from Ishikawa-Ankerhold et al., 2014, and Carl Zeiss Microscopy GmbH, 2019.

In the complex cellular milieu, where molecules engage in finely tuned interactions, the ability to discern and track the movements of various components has become essential for advancing biological models. To visualize these molecular dynamics, scientists label target molecules with fluorescent dyes. The principle of fluorescence is illustrated in Figure 1.2.1 (panel A). When light of a specific wavelength reaches the sample, the electrons in the fluorescent dye absorb this energy and become excited, moving to a higher and unstable energy state. As the electrons return to their ground state, a photon is emitted with a characteristic wavelength. Consequently, following the exposure to an excitation light beam of the sample, the emitted light yielded from the dyes allows for localization and quantification of the labeled molecules in the sample. For example, in figure 1.2.1 (panel C) actin cables of U2OS cells were marked with Green Fluorescent Protein (GFP), a widespread fluorescent probe which emits green light.
To accurately represent the typical absorption and emission processes of a specific dye molecule, one can utilize the Jablonski diagram, as depicted in Figure 1.2.1 (panel B) for GFP. The electronic states S_0 (ground level), S_1 and S_2 (the first two excited states) represent different configurations of electron positions. Within each electronic state, there can be several vibrational energy levels. These correspond to different ways in which the atoms of the molecule can move relative to each other, such as by stretching or bending motions, while the electrons remain in a particular electronic configuration. These intermediate states play a crucial role in the transitions of the molecule. Indeed, in the case of GFP, the typical wavelength absorbed is around 490 nm. The energy provided by the system during this process makes the energy state of the system jump at the level S_2 or S_3. However, because of fast relaxation (of the order of 10^{-12} s) of nonradiative process, i.e. process that does not emit photons, the energy absorbed is partially lost. Examples of these processes are vibrational relaxation and internal conversion, if the system transits to a very close energy level yet with a different electron configuration. Consequently, when the system returns to the ground state (with a typical lifetime of 10^{-9} s), it emits a photon of lower energy compared to the absorbed state, hence different wavelength. The difference between the emitted and absorbed wavelength is called the Stoke's shift, and it is characteristic of each dye. In this way, the absorption spectrum does not overlap the emitted spectrum (Figure 1.2.1, panel B, at the bottom). This is advantageous because the experimental apparatus can more easily distinguish between absorbed and emitted light, preventing the emitted light from being reabsorbed by the sample itself.
In order to calculate the intensity of light emitted by the fluorescence process, I_{em} one should consider I_{ex}, the exciting light, and I_{na}, the part of light that is not absorbed by the sample, as depicted in figure 1.2.1 (panel D). The emitted light I_{em} is in relation with the absorbed light $I_{\text{ex}} - I_{\text{na}}$ as

$$I_{\text{em}} = \phi(I_{\text{ex}} - I_{\text{na}}) \tag{1.4}$$

where ϕ is the quantum yield, a number between 0 and 1, typical of the sample, which takes into account the ratio between the emitted and absorbed photons.
Thanks to Beer's law, the not-absorbed light can be expressed as a function of the excited light

$$\log\left(\frac{I_{\text{ex}}}{I_{\text{na}}}\right) = \varepsilon c x \tag{1.5}$$

where ε is the extinction coefficient, c is the concentration of the sample and x is the mean path length of the light through the sample. From the last equation, it is possible to arrive at the following relation

$$I_{\text{em}} = \phi I_{\text{ex}}(1 - e^{-\varepsilon c x}) \tag{1.6}$$

Hence, for small attenuation value ($-\varepsilon c x << 1$), the emitted intensity of light due to fluorescence is proportional to the concentration value as

$$I_{\text{em}} \approx \varepsilon I_{\text{ex}} c \tag{1.7}$$

From this formula, in order to have higher emitted light, which may help for better visualization, one should increase the excitation light. However, over repeated high-light exposure, dyes lose their ability to fluoresce as a result of chemical alteration. This effect is called photobleaching, and it limits the light intensity of the experimental apparatus and the number of frames to acquire before the fluorescent signal is completely off. Figure 1.2.2) shows this fading phenomenon for BY-2 cells expressing GFP-MAP4, a protein associated with the assembly of microtubules.

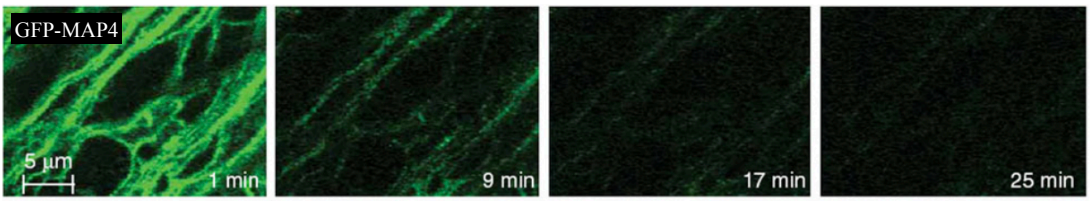

Figure 1.2.2: Photobleaching fading. In the figure, it is shown the photobleaching fading effect, i.e. fluorescent signal loss, due to the damaged fluorescent molecules by prolonged illumination. The sample is tobacco BY-2 cells expressing microtubule-associated GFP-MAP4. Figure adapted from Hoebe et al., 2007.

In conclusion, fluorescence reflects the ability of fluorescent molecules to absorb and re-emit light of a specific wavelength for a limited number of cycles. This property can be exploited to quantify the dynamics of molecules in the cell.

1.2.2 Fluorescence microscopy

In the previous section, we described the process of fluorescence, but this section instead focuses on the experimental equipment required to excite fluorescent molecules and measure the emitted light.

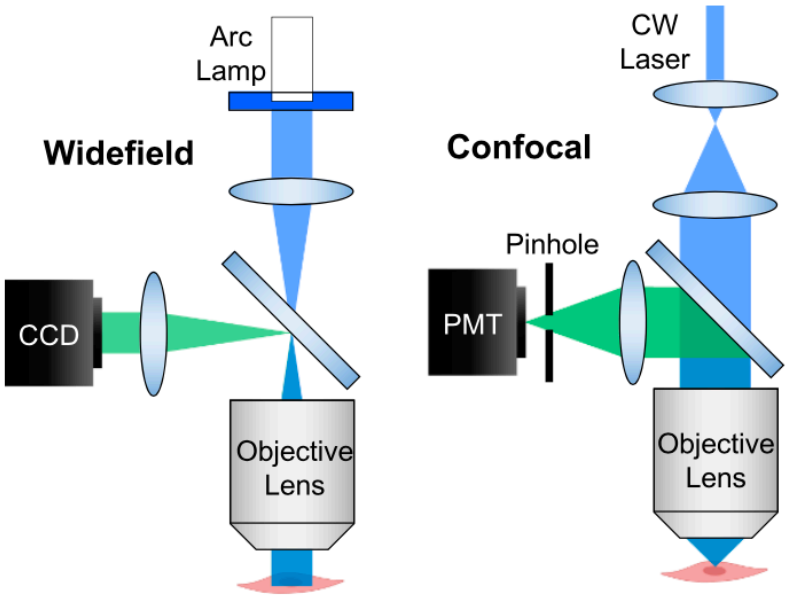

Figure 1.2.3: Widefield and Confocal microscope. Example of two common microscopes for capturing fluorescent images. On the left: widefield microscope endowed with a source of lamp (the arc lamp), filters to select proper wavelengths, dichroich mirrors to reflect light on the specimen or on the detectors according to the wavelength, objective lens and a charge couple device (CCD) as detector. On the right, confocal microscope constituted of similar elements to the widefield but with a laser beam as source of light, objective lens which focuses light only on a small point on the sample, a pinhole which helps to block out-of-focus light and photomultiplier tube (PMT) as detector. Image adapted from Mannam et al., 2020.

For this purpose, several microscopes have been developed. Here, I describe the two most common types: widefield and confocal (Merchant and Periasamy, 2008). As represented in Figure 1.2.3, the two instruments have in common the following features:

- an illumination source at require wavelength: xenon lamps or mercury to produce white light for the widefield microscope, while lasers for confocal; the light of a peculiar wavelength can be selected by inserting filters in the illumination path
- separation between emitted and excited light: for this purpose, the use of dichroic mirror which discern light of different wavelengths and addresses it to the detector or the sample.
- detection of the emitted light: this process is obtained by proper detector such as CDD (charged-coupled device) cameras or PMT (photomultipliers tubes) that capture light in an array where each pixel converts light photons into charge and then assembles this information into a digital image; CCDs are preferred for high-quality imaging with good spatial resolution, while PMTs are the choice for ultrasensitive detection of light, especially in scenarios where single-photon detection is needed.

The main difference between widefield and confocal lies in how they handle the focus plane within the sample, i.e. the depth within the sample at which the image is in sharp focus. Widefield microscopy illuminates the entire depth of the sample at once, capturing images that include both in-focus and out-of-focus areas. This often results in blurred images because of light from structures outside the focal plane. In contrast, confocal microscopy employs a point-by-point scanning mechanism, focusing specifically on one depth and one horizontal position at a time, which limits image capture to the in-focus structures, enhancing clarity and detail. However, widefield microscopy offers a faster imaging process as result of its ability to capture the entire field of view in one exposure. This speed makes it particularly suitable for live-cell imaging, time-lapse studies, and high-throughput screenings where rapid data acquisition is essential. Despite its slower speed, confocal microscopy is preferred when depth discrimination and higher resolution are required, particularly to construct detailed three-dimensional images of thick specimens.

As discussed earlier, the intensity of emitted light is proportional to the sample concentration. However, due to optical system limitations such as diffraction of light diffraction of light at the microscope's objective lens, illumination from a single point source experiences blurring. This blurring effect is described by the Point Spread Function (PSF), which is characteristic of each optical device, as shown in Figure 1.2.4. Typically, the PSF can be approximated by a Gaussian function with a specific width. Consequently, the measured signal intensity I_{exp} at any given pixel is the result of the convolution between the sample concentration and the PSF.

Furthermore, the signal is affected by a background value which is not related with the sample concentration, and technical noise, i.e. fluctuations of the signal due to the experimental apparatus.

The background can be derived from natural fluorescence of untagged molecule in the field of view, non-specific binding of fluorescent dyes, from scattering of environmental light and electronic component of the detector.

The principal sources of noise, instead, arise from two primary processes. The first is photon shot noise, which is associated with the statistical distribution of detected photons and adheres to Poissonian statistics. The second source is read-out noise, which originates from the electronic components of the detectors and follows a Gaussian distribution.

To wrap up, fluoresce signal emitted by dye molecules can be quantified by the detector of the microscope and convert it as an image. However, the experimental device introduces errors that should be accounted for in the theoretical model of the experimental data.

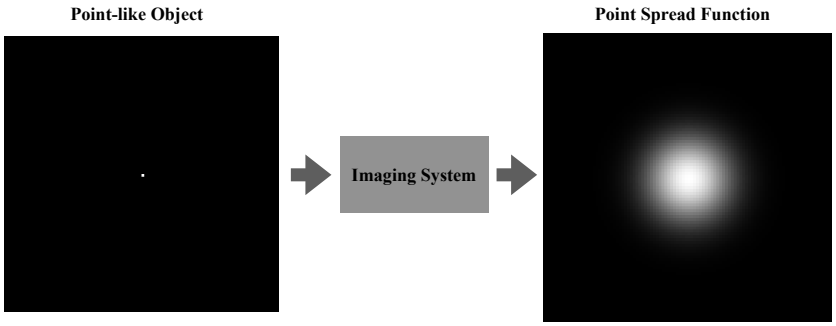

Figure 1.2.4: Point Spread Function. The figure illustrates how a point-like object is transformed into a point spread function (PSF) through an imaging system. The left panel represents the original point-like object, which is a source of light that would ideally appear as a single bright point. After passing through the imaging system, the point-like source is blurred into a PSF, as shown in the right panel. The PSF describes how an imaging system spreads the light from a point object over a region of space due to optical limitations.

1.2.3 Applications

To study the mobility properties of the molecules, it is possible to resort to fluorescence microscopy, as previously explained. In this manner, the tagged molecule is attached with a fluorescent dye and the intensity of the signal be recorded by the experimental device.
Different applications are possible, depending on the variable of interest and on the temporal and spacial scale. Singular particle tracking (SPT) is an experimental method to compute the MSD of the trajectory of single particles inside the cell. From this parameter, it is possible to discern different dynamics, such as random or oriented motion. However, tracking a single molecule can be very complex since the diffraction spots of different molecules could overlap. Another possibility is the fluorescence correlation spectroscopy (FCS) experiment, where the illumination is focused on a tiny spot, less than 1 μm^3. Since the focal volume is very small, the number of molecules going into and out of this area is limited and subject to concentration fluctuations. From the analysis of this value, it is possible to extract mobility parameters. High correlation between images at different temporal instants highlights a slow mobility, while a low correlation is related to slower mobility.
However, if one is more interested in studying the dynamics at a larger scale (more than 1 μm), one should resort to Fluorescent Recovery After Photobleaching (FRAP). The protocol, as depicted in figure 1.2.5, consists in exploiting the fluorescent property of a target protein molecule or labeling it with a fluorescent tag. Then, a small area of the sample is bleached using a high-intensity laser, causing the near-total fading of the signal in that area. Afterward, the fluorescence intensity of the damaged region of interest is monitored over time. The faster the motion, the shorter the time the signal takes to recover within the bleached region. So, from the analysis of the signal, it is possible to deduce the movement

of fluorescent molecules into and out of the bleached spot.
To extract quantitative information about protein dynamics, the signal within the initial bleached region is averaged and plotted as function of time. From the curve, it can be extracted the characteristic time of the recovery, from which the diffusion coefficient depending on the size and on the shape of the bleaching. For example, if dynamics is described by diffusion and the FRAPped area is a circle of radius r, the diffusion constant is given by

$$D = \frac{r^2}{4\tau_{1/2}} \tag{1.8}$$

where $\tau_{1/2}$ is the half-recovery time, i.e. the time at which the signal is equal to $I_B + \frac{I_\infty - I_B}{2}$, with I_B the signal after initial bleaching and I_∞ the signal once it reaches a stationary state. Beyond this quantitative approach based on the timescale of recovery, a universal method to discern dynamics of the cell, diffusion, active transport and chemical reaction is still an object of research. Moreover, the low signal-to-noise ratio, high photobleaching, restricted spatial and temporal window makes it challenging to extract kinetic parameters from data. For this reason, in chapter 4, I work on a novel inference method that can fix these issues.

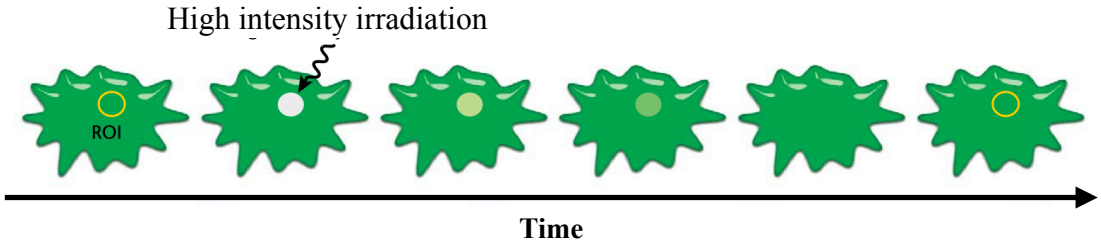

Figure 1.2.5: Cartoon of FRAP experiment. Pictorial representation of FRAP experiment, where a region of interest (ROI) is irreversibly photobleached by a high intensity laser. Due to surrounding molecules movements, the fluorescent signal (in green) in the bleached region recovers over time. Figure adapted from Ishikawa-Ankerhold et al., 2014.

In conclusion, fluorescence microscopy enables monitoring of the spatiotemporal evolution of a molecule's concentration by exploiting the property of molecules to absorb and emit light. Among the various applications of this technique, FRAP is particularly effective in quantifying the system's kinetic parameters. However, data interpretation is challenging due to contamination by experimental artifacts such as photobleaching during imaging, limited resolution, and high noise levels.

In this chapter, I have shown how molecular motion within the cell can vary and be influenced by external factors, and I described how this behavior can be studied experimentally. In the next chapters, I focus on a specific protein, Wsc1, whose motion has been recently proved to be sensitive to mechanical signals.

CHAPTER

TWO

WSC1 PROTEIN AS FISSION YEAST MECHANOSENSOR

This chapter reviews literature to introduce the study of a protein in fission yeast, Wsc1, a receptor capable of perceiving mechanical variations in the cell wall and activating a response to preserve cell integrity. After discussing the ubiquitous nature of mechanical stimuli in biology, I explain the concept of mechanosensing, the ability of living systems to detect mechanical signals. Afterwards, I describe models that illustrate how mechanical forces may be sensed by subcellular receptors, such as membrane channels, whose opening is sensitive to membrane tension. Next, I present mechanosensing in the cell wall of fission yeast. In particular, I focus on the Wsc1 protein, which has been observed in recent experiments to form clusters in the compressed region of the cell wall. Moreover, performing FRAP experiments, researchers measured a lower protein mobility in the cluster region. These pieces of evidence will drive my work in developing a model for protein dynamics exhibiting a clustering behavior.

2.1 Introduction to mechanosensing

2.1.1 Mechanical forces in biology

Living systems experience a myriad of mechanical stimuli, including compressive, shear, and tensile stresses (Mishra et al., 2022). These processes involve forces that push or pull directly on a surface or that act parallel to the surface, causing deformations and friction, as seen when cells navigate narrow channels like red blood cells in capillaries (Secomb et al., 2001; Skalak and Brånemark, 1969). The stresses can occur when a surface is stretched or pulled, such as in biological membranes under tension (Sitarska and Diz-Muñoz, 2020). These forces can derive not only from the external environment, e.g. the contact with a subtract or the fluid they are surrounded by, but also from inside the organism, for instance an internal pre-stressed pattern due to the shape and the geometry (Hamant and Haswell, 2017).
From the macromolecule scale up to molecular organism level, forces in biology can span different range of magnitudes (Prabhune et al., 2017). A molecular motor, such as myosin II, can exert a force of the order of the pN by 'walking'

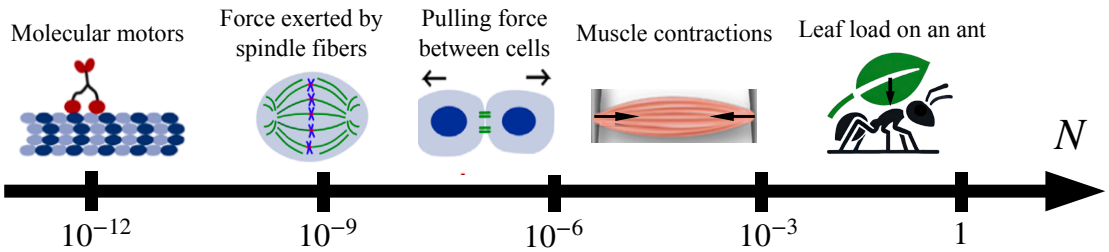

Figure 2.1.1: Different range of mechanical forces in biology. The arrow spans different force scales (expressed in Newton [N]) varying from pico N up to 1N. From left to right, the systems considered are: a molecular motor (at the top) acting on microtubules (at the bottom), the action of multiple molecular motors on spindle fibers (green) to separate the chromosomes (purple), cell junction (green) to separate two cells, contracting muscle and the load of a leaf on an ant. The arrow highlights the direction of the forces. This figure was adapted from (Prabhune et al., 2017)

on cylindrical structure made of proteins, the microtubules. During cell division, the action of multiple molecular motors on organised microtubules, the spindle fibers, can generate a force able to segregate the chromosomes of two cells. Differently, cells within tissue can form junctions made of proteins such as E-cadherins that are able to transmit forces of the order of 100 pN. If we look broader, the muscle contractions can free a contractile force between micro and milli Newton (Vesga-Castro et al., 2022). To compare these values with something more close to everyday experience scale, leaf-cutter ants, *Atta cephalotes*, can load a weight 10^{-1}/1 N which is approximately 9 times their body weight (Segre and Taylor, 2019).
Overall, mechanical forces play an important role in many biological activities, for instance cell migration, proliferation, morphogenesis, cell polarization, cell adhesion and so on. As an illustration in 'On growth and Shape' (Thompson., 1917) it is shown how the shape of the cell can be set by diagram forces with many analogies with the physics of bubbles. However, particular hostile physical properties of the microenviroment can lead to many diseases (Verbruggen, 2018).
For this reason, the study of how physical forces can regulate complex living systems is a growing field.

2.1.2 Definition and examples

Mechanical forces are non-uniform and dynamic as they change in space and in time, constituting a potential source of damage. In fungal cells, the internal turgor pressure is born by a rigid layer around the membrane, the cell wall. During growth, the balance between the cell wall tension and this internal stress sets the shape of the organism. However, since the pressure is very high, local defects in the cell wall composition may not withstand this force. So at certain points, excessive stress on the cell wall can lead to cell bursting (Davì et al., 2018, 2019). For this reason, an active response of the system to mechanical stimuli is required. This characteristic is shared with all living systems. In *P. aeruginosa*, a type of bacteria, detection of stiffer substrate rigidity promotes the transition from living as free-floating, individual cells (called planktonic) to growing together in a

Figure 2.1.2: Example of mechanosensor models. On the left it is shown the operating principle of a mechanosensitive channel, representing in red arrows the tension which causes the opening of the channel. On the right, instead, the two-spring model where the molecular motor is colored in red. The latter applies on average a force dependent on the equivalent elastic constant of the whole system $k_{eq} = (\frac{1}{K_{ECM}} + \frac{1}{CYT})^{-1}$, with k_{ECM}/k_{CYT} the elastic constant of the ECM/cytoskeleton. Instead, the biomolecular bond, responsible for the downstream signal, opens with rate r, dependent on $< F >$.

dense, sticky group attached to a surface (called a biofilm) (Straub et al., 2019). In *Arabidopsis*, a small flowering plant, experimental evidence demonstrates that root network growth alters its direction in response to the detection of a physical barrier (Monshausen and Gilroy, 2009). In animal stem cells, mechanical cues are important to influence the cell identity and gene expression (Ferrai and Schulte, 2024).
From this perspective, mechanosensing refers to the ability of cells—or smaller scale components—to detect mechanical cues in their microenvironment, such as stress, strain (deformation), or other mechanical properties like substrate adhesion (Y. e. a. Chen, 2017). These mechanical signals are then transduced into biological pathways (mechanotransduction), i.e. a series of actions among molecules in a cell that leads to a specific product or change within the cell, i.e. a series of interconnected molecular events within a cell that lead to a specific outcome, such as a sequence of chemical reactions or an electrical signal.
Numerous mechanosensing mechanisms have been investigated in recent studies (Orr et al., 2006; Rodicio and Heinisch, 2010). The prevailing idea is the identification of putative mechanosensors at the microscopic scale, typically receptors that are sensitive to mechanical signals. For example, mechanical forces can alter the energy landscape of a protein, leading to a conformational change. The mechanosensor then transduces the mechanical signal into a downstream chemical signal. Ultimately, the integration of signals from multiple sensors, whether at the subcellular level or on a more global scale (tissues, organs), orchestrates the system response (Fruleux et al., 2019).

2.1.3 Review of mechanosensing models

In this section, I will explore key examples of biological mechanosensing systems studied so far and discuss how the dynamics of mechanosensors can be modeled.
One of the most studied systems sensitive to mechanical signals are the mechanosensitive channels (MSC), which are present along the membrane of the cell in different

domains of life, such as bacteria, fungal cells and plants (Municio-Diaz et al., 2022). When the membrane is stretched, the resulting tension is directly transmitted to the channel (Martinac, 2004), facilitating its opening and thereby promoting the flux of ions, as shown in figure 2.1.2. MSCs are crucial for managing sudden hypoosmotic shocks. If a large influx of water enters the cell, the resulting swelling can rupture the cell wall (the bacterial envelope). Activating these channels helps the organism stabilize osmotic pressure and prevent cell damage.
Different models are proposed to describe this phenomenon, depending on the scale of interest. By examining a single mechanosensitive channel, its energy landscape can be modelled based on its interaction with the cell membrane (Wiggins and Phillips, 2004, 2005). When mechanical force is applied, the equilibrium conformation—determined by the minimum of free energy—shifts from the closed state to the open state. To study cooperative effects and the emergence of collective behavior of the channels -important to temperate the answer of the system- a lattice gas-like model can be analysed (Fernandes et al., 2017). A basic model can be introduced by representing the membrane as a two-dimensional lattice. In this framework, each position on the lattice can be occupied by a channel that exists in one of two states: open or closed. The interaction between the channels depends on their state. In this manner, the statistical-mechanics approach can be exploited to understand under which condition the formation of clusters of channels is possible, as observed in experiments. To achieve more realistic models, it is beneficial to consider a coarse-grained approach at the molecular scale (Paraschiv et al., 2020), where a single channel is divided into various sub-units with distinct chemical properties, resulting in different interaction behaviors. Although analytical studies become impractical in this scenario, simulations can be employed to obtain results.
To describe only the downshock water and solute transport across the membrane, a continuum model (Buda et al., 2016) can be set. In this model, the dynamics, set in partial differential equations, is driven by the chemical potential difference inside-outside of the cell considering the stress stiffening properties of the cell wall. Channels are open only if volume exceeds a threshold, whose value, however, is not easy to determine for each channel because it must consider the effect of the interactions between them.
Another interesting mechanosensing model of study is focal adhesion, i.e. large macromolecular assemblies that form mechanical links between the cytoskeleton and the extracellular matrix (ECM) and drive cell locomotion. This complex can grow anisotropically in the direction of the stress (Nicolas et al., 2004) and it is also susceptible to the mechanical properties of the surrounding. The two-spring model proposed by Schwarz et al. (Schwarz et al., 2006) explains how these mechanonsensors can be sensitive to the stiffness of the environment. Indeed, if the theory of elasticity is applied, ECM and cytoskeloton are modelled as two springs in series, as in figure 2.1.2. The internal state of the focal adhesion is represented by a biomolecular bond whose open probability is described by stochastic equations, whose rates depend on the force. When a molecular motor, myosin II, exerts a force, it feels the equivalent spring constant of the whole system, and it would exert a lower to higher mean force during its application on a softer stiffer spring. Then, since bond's breaking rate, responsible for the downstream signal, depends on the force, the information about the stiffness of the environment can be di-

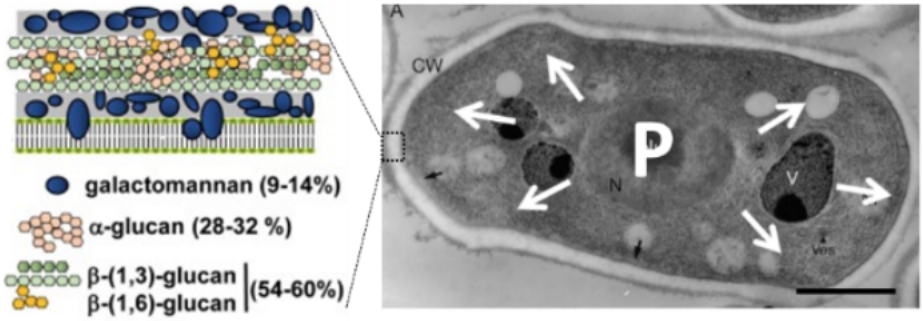

Figure 2.2.1: . Schematic and electron microscopy image of the fission yeast cell wall structure. The left panel illustrates the cell wall composition, highlighting the major polysaccharide components: galactomannan (9-14%), α-glucan (28-32%), β-(1,3)-glucan, and β-(1,6)-glucan (54-60%) (Pérez et al., 2018). The right panel shows a transmission electron microscopy image of a fission yeast cell, with internal pressure P (turgor) which exerts force on the cell wall (indicated by the arrows)

rectly perceived by the cell. Afterwards, focal adhesions are reinforced where the ECM is stiffer and consequently guide the movement of the cell, as experimentally observed.
In the latter example, chemical reactions are described by a probabilistic agent-based model. However, for large system the deterministic treatment and continuum models are a good approximation. Ali et al. (Ali et al., 2011) propose a method to couple mechanics with chemistry by focusing on the clustering behavior of integrin, an allosteric transmembrane protein involved in cell adhesion. Their main assumption is that once the protein becomes active and binds to the extracellular matrix, the molecule loses its ability to diffuse along the cell membrane. To capture this behavior, they develop reaction-diffusion equations with rates dependent on the activator field, in this case the strain. This framework enables mechanical signals to regulate integrin binding to the ECM, leading to increased protein density in regions where force is applied.

2.2 Mechanosensing in fission yeast

2.2.1 Fission yeast as model organism

After having highlighted the importance of studying mechanosensing in living system and having shown some examples, in this section I explain the choice of investing these phenomena in our model organism *S. Pombe*, also called fission yeast. As I explain in section 2.1.2, these mechanisms are vital during morphogenesis to ensure the homeostasis of the organism during its expansion (Davì et al., 2018), i.e. a self-regulating process to maintain the mechanical integrity of the cell wall (CW). Fission yeast is a unicellular fungus with a rod-like shape. It is endowed with a stereotypical tip growth, and it elongates from 7 to 14 μm with a constant diameter of about 4 μm (Davì and Minc, 2015). Experimentalists chose this model organism for mechanosensing studies for different reasons.

Firstly, differently from animal cells, the source of forces is limited and restricted to turgor pressure and external constrains, hence reducing the possible source of stress (Hamant and Haswell, 2017). Then, genetically it is easy to manipulate; hence one can produce mutants with defective functions that we are interested in to analyze. Furthermore, only two mechanosensors have been found so far, hence with a low-number of particle species in possible models. Yet above all, it allows for sub-resolution imaging techniques which are able to study the dynamics of the cell-wall thickness (Davì et al., 2019).

2.2.2 Cell wall

Fission yeast, as a fungal cell, is endowed with a stiff polymeric rigid layer encasing the membrane, the cell wall. The CW is made of reticulated polysaccharides, e.g. glucan, chitin and mannans, and proteins (in figure 2.2.1 it is shown the composition for the fission yeast). It plays a structural role similar to the actin cortex in animal cells, but it withstands significantly higher internal pressure, called turgor pressure. The balance with this force determines the shape of the fission yeast cell (Davì et al., 2018). CW has a high Young's modulus (of about 10 MPa) since it must cope with the elevated turgor pressure, which reaches values of about 10^6 Pa. The CW thickness, which is about 100 nm, varies during its growth, due to the strain caused by its own expansion. This thinning is perceived by the cell and then properly compensated with a glucan production increase to reinforce the cell wall itself. Thanks to this positive feedback, it is possible to observe fluctuations of cell wall thickness overtime without reaching too low values which would lead to cell lysis, i.e. the cell wall rupture. This ensures the mechanical homeostasis of the cell wall. Mutants which are defective in performing this response, have lower probability to survive.
Cell wall is usually described by continuum mechanics-based mathematical models (Julien, 2015). The most accepted description is given by the Lockhart's model, in which CW acts as a viscoelastoplastic material (Fruleux et al., 2019). Above a certain threshold of stress, it can irreversabily deform, yet below that value it behaves like an elastic material.

2.2.3 Mechanosensors in fission yeast cell wall

Mechanosensing in fission yeast is crucial for maintaining cell integrity, especially during growth, when the cell wall risks excessive thinning during its expansion. To avoid damages, it is fundamental for the cell to be endowed with mechanosensors along the cell wall capable of activating the cell wall synthesis to reinforce this layer (figure 2.2.2, left panel). Research by Cruz et al. (Cruz et al., 2013) identified two putative mechanosensors in fission yeast involved in this process: Wsc1 and Mtl2. Using genetic techniques to cultivate yeast cells lacking Wsc1 or Mtl2, the study analyzed how these modified cells responded to environmental stresses, such as osmotic shock or antifungal drugs affecting the integrity of the cell wall. Without Wsc1 or Mtl2, cells exhibited lower glucan synthesis production and decreased viability under cell wall stress conditions compared to wild type. The higher sensitivity to environmental changes underscores the role of Wsc1 and

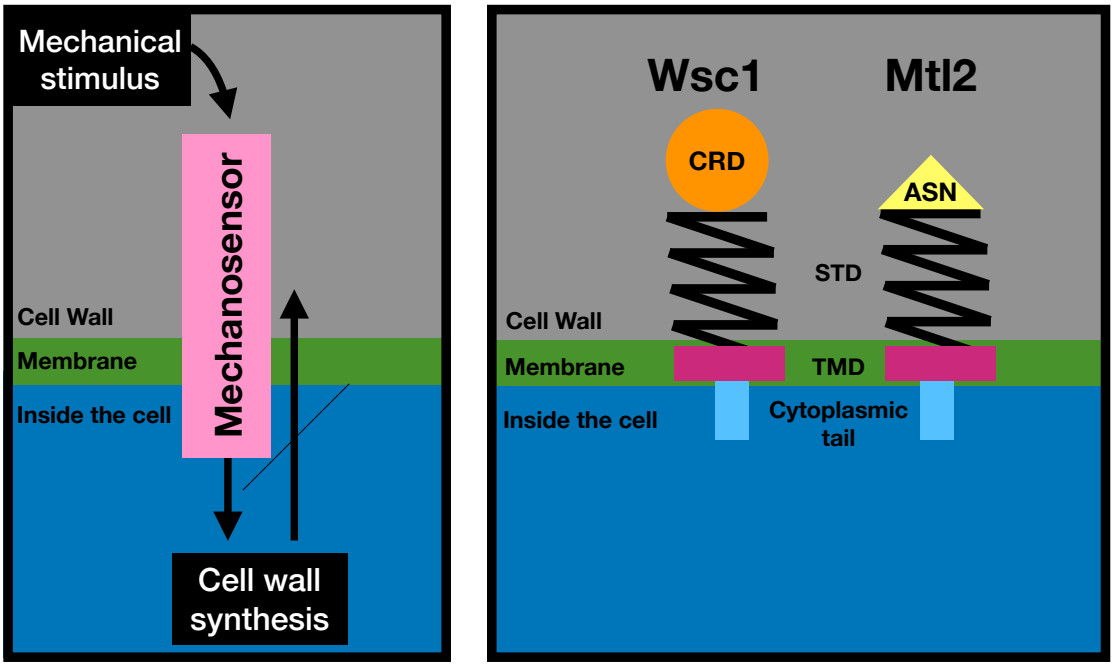

Figure 2.2.2: Wsc1 and Mtl2 protein as mechanosensors. The left panel shows a mechanosensor in the cell wall (in pink), such as Wsc1 or Mtl2 protein, that after a mechanical stimulus (stress or strain), stimulates the glucan synthesis to reinforce the cell wall. On the right panel instead, it is exposed the structure of the Wsc1 and Mtl2 protein. Wsc1 is composed by the head (in orange) which is a cystein-riched domain (CRD), also called Wsc domain, then the serine-threonine riched (STR) domain which behaves like a nanospring, the transmembrane domain (TMD) and the cytoplasmic tail. Mtl2 protein shares the same structure but with an N -glycosylated asparagine as head group (in yellow).

Mtl2 in detecting and responding to potentially dangerous mechanical stimuli on the cell wall.

Wsc1 and Mtl2 belong to two major families of single-pass transmembrane proteins, respectively, the Wsc (Wall Stress Component) and MID-type (Mating-Induced Death) families, which are conserved among yeasts. Experiments have confirmed that these proteins activate the Cell Wall Integrity (CWI) pathway. This pathway is triggered by a signaling cascade initiated by surface receptors and promotes the expression of genes for cell wall synthesis and repair, strengthening the cell wall and enhancing resistance to environmental stress (Municio-Diaz et al., 2022).

The WSC and MID sensors share a similar structure (figure 2.2.2, right panel): a cytoplasmic C-terminal tail for downstream signaling, a single transmembrane domain (TMD), an *O*-mannosylated serine/threonine-rich (STR) region and a head group. Within the WSC family, the head group includes a conserved WSC cysteine-rich domain, while in the MID family, an *N*-glycosylated asparagine head group is present. These WSC cysteine-rich domains are part of the C-type lectin family, allowing them to bind carbohydrates via multiple weak interactions (Kock et al., 2015; Oide et al., 2019; Wawra et al., 2019). Atomic force microscopy studies derived from *S. cerevisiae* Wsc1 and Mid2 STR regions have shown that these domains behave like nanosprings, expanding linearly in response to applied

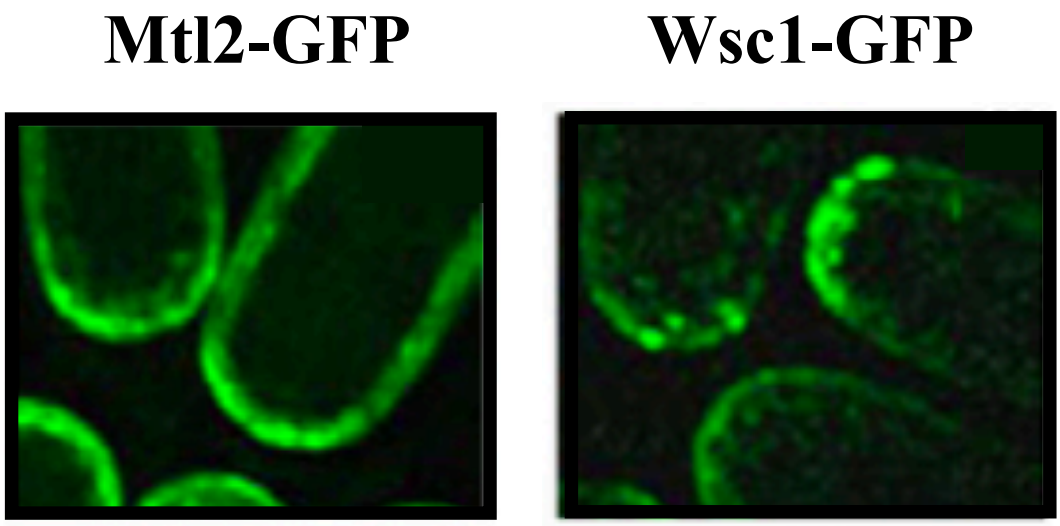

Figure 2.2.3: Wsc1 and Mtl2 protein distribution in fission yeast. Fluorescence microscopy images showing the localization of Mtl2-GFP and Wsc1-GFP in fission yeast cells. While Mtl2 concentration is homogeneous around the cell, Wsc1 concentration is more peaked at the cell tip. Figure adapted from Cruz et al., 2013.

force (Dupres et al., 2009). Studies on mutants with defects in this domain suggest that the STR region is essential for the effective transmission of mechanical signals downstream.
In fission yeast, Wsc1 and Mtl2 show distinct localization patterns within the cell (Cruz et al., 2013), as shown in fluorescent microscopy images in figure 2.2.3. Wsc1 is concentrated at the cell tips, whereas Mtl2 is distributed more homogeneously throughout the cell wall. This differential localization suggests specialized roles for each sensor. Wsc1's concentration at the cell tips enables it to detect and respond to intense, localized stress associated with cell growth, making it ideal for reinforcing cell wall biosynthesis under extreme conditions. Mtl2's broader distribution, on the other hand, allows it to sense and respond to a range of environmental stresses, providing a generalized protective mechanism across the cell (Cruz et al., 2013).

2.3 Wsc1 clustering behavior

Besides its capability to activate the glucan synthesis and reinforce the cell wall under stress condition, recent experiments in Wsc1 show that the protein is able to form clusters in the compressed region of the cell wall (Kock et al., 2015; Neeli-Venkata et al., 2021). This behavior, which is also common to other surface receptors, such as integrin in focal adhesion (see section 2.1.3), could be useful for the cell to enhance the capacity of large-force-detection and reduce noise sensitivity to single-molecules fluctuations (Municio-Diaz et al., 2022; Neeli-Venkata et al., 2021).
In this work, I want to understand what drives this phenomenon.
In particular, my study considers the experimental outcomes from the Minc's lab,

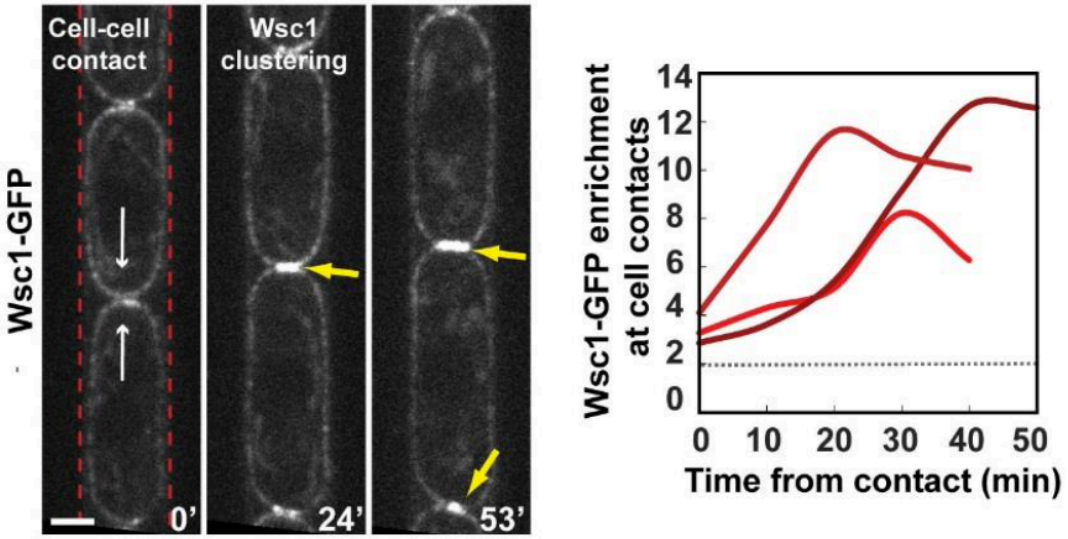

Figure 2.3.1: Wsc1-GFP Enrichment at Cell-Cell Contacts in Microchannels. Yeast cells expressing Wsc1-GFP were observed growing aligned within microchannels. The left panel presents time-lapse fluorescence images showing the initial formation of cell contact (0') followed by clustering of Wsc1-GFP signal at the contact site at later time points (24' and 53'), indicated by yellow arrows. The right panel illustrates the Wsc1-GFP signal enrichment (ratio between the Wsc1 signal in A.U. and a reference signal value at the cell side) over time (in minutes) at the contact site for three different cells (marked by three different colors for the curve). Image taken from Neeli-Venkata et al., 2021.

which are exposed in the article by Neeli-Venkata et al. (Neeli-Venkata et al., 2021). In this work, experimentalists were able to cultivate cells in microchannels, as seen in figure 2.3.1 (left panel). As cells grow and are in contact, the internal pressure that causes the cell to expand exerts a compressive force on the neighbor cell. Following this mechanical stimulus on the cell wall, a clear cluster of the protein appears, as proved by the fluorescent signal enrichment (figure 2.3.1, right panel). Moreover, when the neighbor cell pressure is reduced by laser ablation, the cluster disappears with the same timescale. Hence, not only can the Wsc1 cluster form, but they are also reversible once stress is released. The same result of cluster formation and disassembly is observed with tip-to-tip contact in mating cells, i.e. cells that are preparing to fuse.

By labeling two transmembrane proteins in contacting cells with fluorescent markers (Wsc1-GFP and Psy-mcherry) at their cytoplasmic tails and measuring the distance between their signals (figure 2.3.2, top-left and top-right panel), researchers could track both the signal intensity of Wsc1 and the thickness of the cell wall during compression (figure 2.3.2 bottom panel). This plot reveals a clear trend between these two quantities. Indeed, the higher the compression of the cell wall, the higher the signal from Wsc1 is.

Further investigations by Neeli-Venkata et al. were conducted on various mutants, defective in structural components of the protein or on other possible auxiliary molecules in this process. From this study, it emerges that Mtl2 protein does

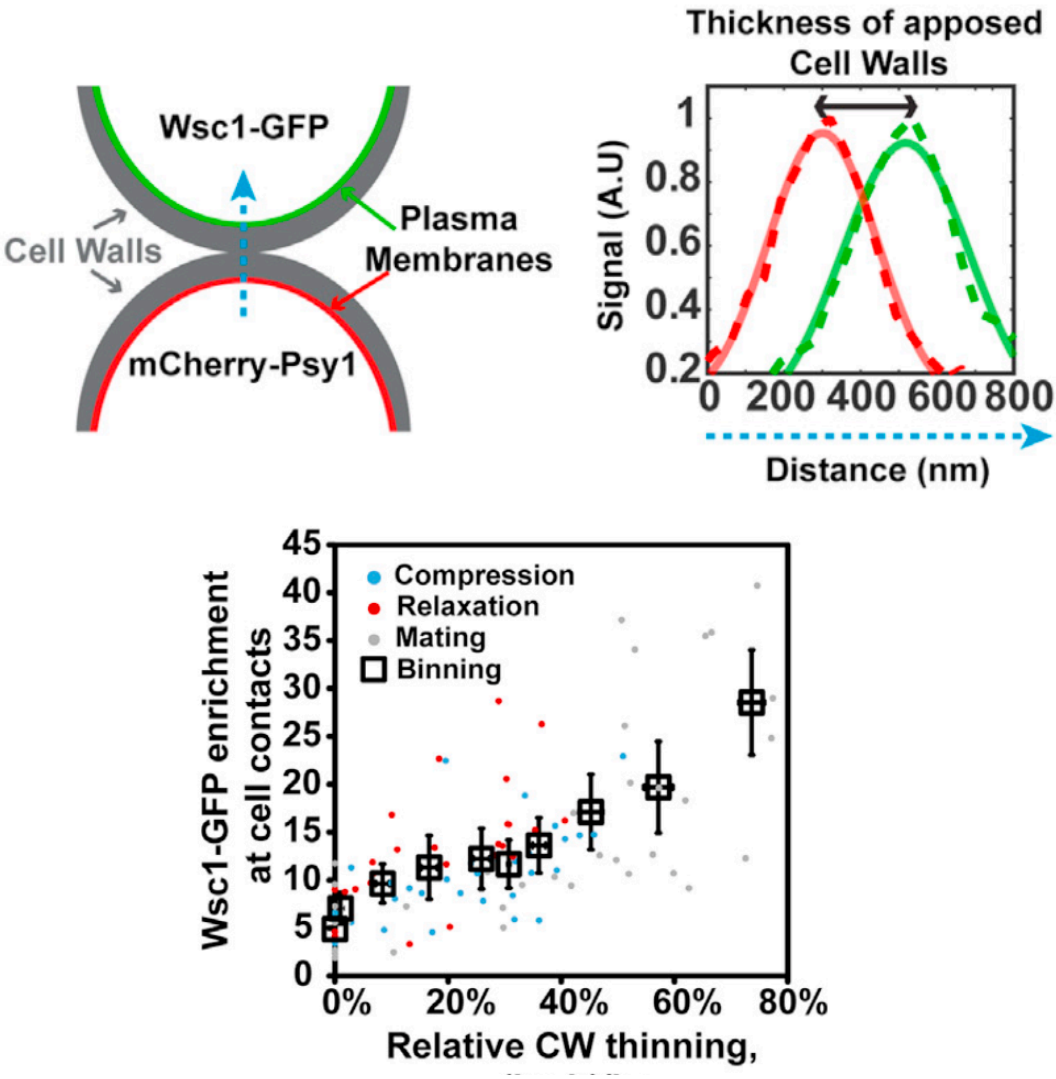

Figure 2.3.2: Wsc1-GFP signal and cell wall thickness. On the top-left and top-right panel, it is shown the experimental technique to measure the cell wall thickness. By labeling two transmembrane proteins -Wsc1 with GFP and Psy1 with mCherry fluorescent molecules-in two cells in contact, it was possible to measure the distance between the two apposed cell wall. On the right panel, it is plotted the Wsc1-GFP signal as a function of the cell wall thinning relative to the thickness at rest (150 nm) supposing the thickness to be half of the distance of two apposed cell walls. The different colors represent three different phase acquisitions: during growth (compression), after laser ablation (relaxation) and during mating. The squares are bins of 10 individual measurements, with error bars representing standard deviations. Figures adapted from Neeli-Venkata et al., 2021

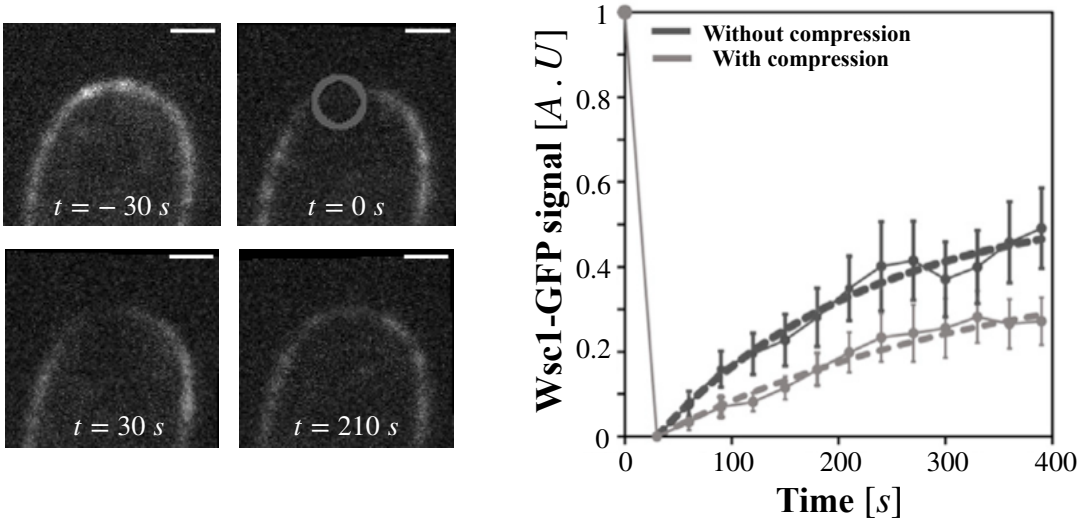

Figure 2.3.3: Wsc1 protein FRAP experiment. On the left panel, it is shown different images for FRAP experiment with Wsc1-GFP protein on free cells tips at different time $t = -30\ s$, $t = 0\ s$, $t = 30\ s$, $t = 210\ s$, with laser photobleaching, at $t = 0\ s$. On the right, the average signal inside the bleached region is plotted as function of time. The error bar represents the mean and standard deviation (SD) for 28 free cells tip (in dark gray) and 27 compressed cells tips (light gray). The two dotted curves correspond respectively to a single exponential fit of experimental data, yielding an average half-recovery time of $\tau_{1/2} = 188.7 \pm 117\ s$(mean $\pm$ SD) for free cell tip and $\tau_{1/2} = 457.3 \pm 479$ (mean $\pm$ SD) for compressed cell tip. The scale bar represents 2 μm. The figure is adapted from Neeli-Venkata et al., 2021.

not play a substantial role in the clustering mechanism since defective mutants on this protein conserve the cluster formation capability. In mutants with defects in the cytoplasmic tail, the clustering capability was preserved, even if there is no downstream chemical signals for the cell wall synthesis. This suggests that clustering is independent of this signaling process. Furthermore, by significantly inhibiting the exchange with the cytoplasm mechanism, the protein distribution becomes more homogeneous around the cell, but it retains the clustering capability. This result may suggest that the clustering behavior is independent on the polarity mechanism, which maintains the Wsc1 concentration peaked at the cell tip. Remarkably, from these experiments, it appears that the most interactive region responsible for clustering is the Cysteine-Rich Domain (CRD), since defective mutants of this protein component do not exhibit the clustering behavior. Following author's consideration, CRD may bind to polysaccharides in the cell wall at a rate dependent on mechanical stress or strain. This increasing interaction may trap the molecules and reduce its diffusivity, causing the formation of a cluster.
To test this reduced-mobility hypothesis, researchers performed FRAP experiments (Figure 2.3.3, panel A). As a result, regions under compression exhibited slower diffusion, as indicated by a longer recovery time for this protein. This is proved by Figure 2.3.3 (panel B), where the recovery curve in the compressed region shows an extended half-recovery time.

In conclusion, sensing mechanical cues from its microenvironment is vital for the cell. For this reason, living organisms are endowed with receptors at the subcellular scale, called mechanosensors, which are able to perceive mechanical cues and activate a system response. One such mechanosensor in the fission yeast cell wall is Wsc1. In particular, this protein exhibits mechanosensitive clustering behavior, i.e., it increases its concentration in the compressed region of the cell wall. Interestingly, the head the protein embedded in the cell wall is essential to conserve this clustering behavior and from chemical considerations, this component of the protein may interact with the cell wall molecules. Moreover, FRAP experiments highlighted a slower dynamics of this protein in the compressed region.

2.4 Questions and challenges in this thesis

The focus of my work is to develop and test mathematical models with experimental data in order to understand the causes of the Wsc1 clustering behavior which is sensitive to mechanical cues.
In particular, I would like to investigate the possible interaction between the protein and the cell wall. Indeed, if compression may increase the polysaccharides' concentration around the protein and consequently enhance the protein-cell-wall binding, I wonder if this increased interaction is able to trigger the clustering behavior observed in the experiments.
Several challenges arise in this endeavor, primarily due to the complexity of the cellular environment. Cells are crowded, dynamic systems where numerous interacting factors can influence molecular motion, making it difficult to pinpoint which actors are essential to the process and which may be unnecessary. For example, Wsc1 may be transported from the cytoplasm to the cell wall, diffuse

along this layer and activate mechanosensing signal pathways. As seen from experiments, not all these processes are fundamental for clustering. For this reason, it is essential to disentangle the different molecular mechanisms and quantify each contribution. In this study, I would like to keep a parsimonious approach building a minimal-ingredient model which is consistent with the experimental results on Wsc1 exposed in section 2.3.
However, data used to test the models are often imperfect, subject to measurement errors, experimental bias and other limitations. Time-lapse videos from FRAP experiment on Wsc1 are particularly noisy, with a low spatial resolution compared to the cell size and with a significant photobleaching during imaging. Therefore, classical analysis based on the mere information about the characteristic time of recovery are not sufficient to discern the different dynamics inside the cell. Hence, besides modeling in this project I develop a flexible inference method which could potentially well-fit the experimental conditions for Wsc1 and gain more information about its dynamics.
In the next two chapters, I first present a model able to reproduce the clustering behavior and justify a slower dynamics timescale in the compressed region of the cell wall. Afterwards, I present an inference method for FRAP experiment able to estimate all the parameters of the model.

CHAPTER

THREE

MODELLING WSC1 MECHANOSENSITIVE CLUSTERING

In this chapter, I present a mathematical model for the clustering behavior of mechanosensitive proteins, specifically for Wsc1 but adaptable to other systems as well. To achieve this, I will translate experimental observations into a set of partial differential equations (PDEs) that describe the evolution of protein concentrations. In particular, I would like to test the hypothesis suggested in the Neeli-Venkata's article (Neeli-Venkata et al., 2021) for which the interaction between the protein and the cell wall is enhanced by compression and leads to clustering. Initially, I will outline the problem's geometry, the various particle species involved, the relevant chemical reaction rates and the different mechanisms of protein recruitment. Subsequently, I will analyze the resulting reaction-diffusion equations and compare the predictions with experimental data. In particular, I focus on the relation between the different parameters, e.g. concentration, diffusion, and cell wall thickness.

3.1 Building the model

3.1.1 Geometry of the system

Firstly, it is essential to address the spatial domain of the system. Specifically, the protein Wsc1 is a cylindrical transmembrane protein with part of its domain embedded in the cell wall. Therefore, I can use the cell wall as a reference for the protein position and I can describe the protein concentration evolution with respect to this layer. In particular, we focus on the cell tip, which is the region where most of the Wsc1 experiments occur. Within this area, the cell wall layer can be approximated as a 2-dimensional curved surface (Abenza et al., 2015), assuming that the dynamics in the direction orthogonal to the cell wall is negligible. This approximation is reasonable given that the cell wall is sufficiently thin (~ 100 nm) relative to the cell tip radius ($\sim \mu m$).
However, to maintain computation simpler and analytically tractable, I develop the model in a 1D flat geometry. This approximation can be fit with experiments where the cell tip is flattened by contact forces and the concentrations vary mostly

along one direction. Nevertheless, beyond these scenarios, too simple geometry approximation can lead to an overestimation or underestimation of dynamical parameters. For instance, diffusion on a 2D curved surface tends to be underestimated when modeled as a 2D flat surface. Nevertheless, it is fair to assume that such scaling factors are not critical for understanding the clustering behavior.
Consequently, the investigation of more complex and realistic geometries will be reserved for future works.
For notation, I indicate the x-axes direction tangential to the cell wall and I suppose that the spatial domain is sufficiently big to consider the infinite space approximation, where dynamics does not feel the effect of the boundaries.

3.1.2 Assumptions on protein dynamics

In this section, I describe the assumptions on Wsc1 dynamics.
Following the experimental consideration that the head of Wsc domain can interact with the polysaccharides of the CW, I suppose that the proteins can be found in two possible states: bound or unbound to the CW. Denoting with $c_{\mathrm{u/b}}$ the concentration of bound/unbound proteins, the total density of Wsc1 proteins is given by $c_{\mathrm{tot}}(x) = c_{\mathrm{u}}(x) + c_{\mathrm{b}}(x)$. The exchange of particles between the two states is defined by the following chemical reaction

$$\mathrm{U} \underset{\mathrm{k_{off}}}{\overset{\mathrm{k_{on}}}{\rightleftharpoons}} \mathrm{B} \tag{3.1}$$

In this case, k_{on} is the binding rate, by which unbound particles get bound to the cell wall, while k_{off} is the constant which regulates the inverse process.
Moreover, since the link with cell wall components is supposed to be weaker, unbound proteins are free to move laterally along the cell wall with a lateral diffusion constant D, while bound proteins are trapped by the polysaccharides network and do not diffuse. Coherently with the previous section, I neglect all other degrees of freedom, e.g. rotational diffusion.
Furthermore, I account for an homogeneous influx of proteins from the cytoplasm with an intensity α (representing exocytosis). This corresponds to the assumption that cytoplasmic concentration is constant near the cell surface. Conversely, I assume that unbound proteins are recycled via endocytosis at a rate of β per protein.
The combined effects of these factors are illustrated in the model shown in Figure 3.1.1, where the unbound proteins (in pink) can laterally diffuse along the CW and be exchanged with the cytoplasm, while bound proteins (brown) are fixed.

3.1.3 Mechanosensitive binding

Although the dynamics of Wsc1 are not described in the direction orthogonal to the cell wall, the information about the thickness of the cell wall can be incorporated into a spatial field, defined as the compression profile. In this model, the compression profile is represented by the function $h(x) : \mathbb{R} \to [0, H]$, which quantifies the variation of cell wall thickness at each point $x \in \mathbb{R}$ in space, relative to a CW thickness at rest H. At the same time, I can define the relative thinning of the CW as $h_{\mathrm{r}}(x) = \frac{h(x)}{H}$.

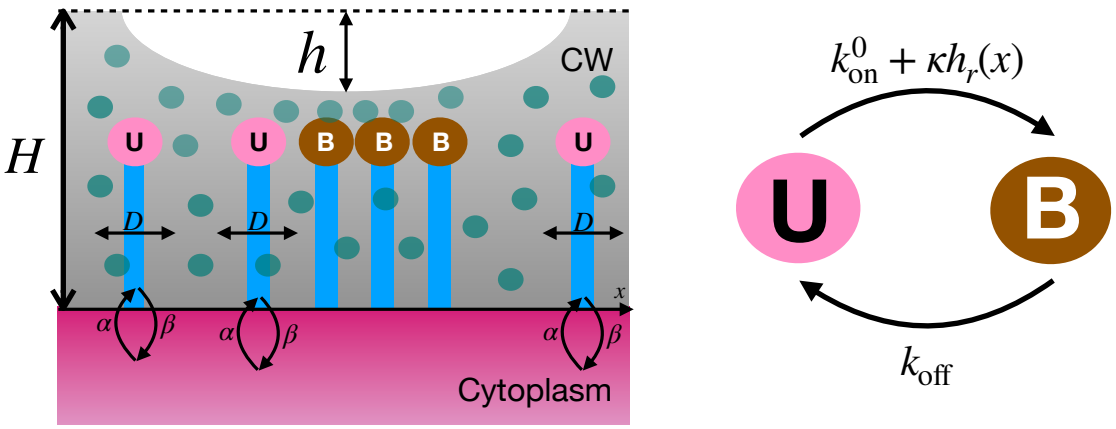

Figure 3.1.1: Protein model. Schematic representation of the 1D Wsc1 model. Different colors of protein heads (i.e. the Wsc domain) represent the two different states, bound and unbound to the cell wall, brown and pink respectively. The unbound proteins can diffuse along the cell wall (x-axis) and being exchanged with the cytoplasm with the cytoplasm with an incoming flux α and dissociation rate β. H represents the cell wall thickness at rest, and $h(x)$ is the compression profile at each point of the cell wall. In the compressed region, the polysaccharides molecules (in green) get more packed around the protein head. The transition rate between the two states is regulated by the binding constant $k_{\text{on}} = k^0_{\text{on}} + \kappa h_r(x)$ and unbinding constant k_{off}, where $h_{\text{r}} = \frac{h}{H}$ is the relative thinning, k^0_{on} is the binding rate when there is no compression and κ the increase due to compression.

I assume that $h_{\text{r}}(x)$ is prescribed, and it does not vary with time. This corresponds to the static situation where external or internal forces impose a constant thickness of the cell wall.
After having defined the compression profile, I need to model how this mechanical parameter can alter the protein dynamics. Qualitatively, as compression occurs, polysaccharides in the cell wall get more packed around the protein's head as depicted in figure 3.1.1, thereby increasing their interactions. Conversely, the reverse reaction rate, from the bound to the unbound state, does not depend on the polysaccharides' concentration, if we model it as a ligand-receptor like reaction (Long et al., 2006). Therefore, in my framework I suppose that k_{on} is a functional $k_{\text{on}}[h_{\text{r}}(x)] : h_{\text{r}}(x) \to \mathbb{R}^+$, which depends on the compression profile. It is worthy to remark that in the latter definition, I implicitly assume that local variation of CW relative thinning $h_{\text{r}}(x)$, implies a local variation of the binding rate $k_{\text{on}}(x)$. Furthermore, once I fix the compression, k_{on} is a function of space. So if the compression profile is uniform, k_{on} is a constant parameter which depends only on the level of compression. On the contrary, k_{off} does not depend on thickness of the cell wall.
Most of the following calculations require only that k_{on} is a parameter independent on the variable c_{u}, the unbound protein concentration, and c_{b}, the bound proteins concentration, in order to have linear PDE (partial differential equations). However, to directly show the compression profile $h_{\text{r}}(x)$ effect on protein dynamics, I consider an explicit relation between k_{on} and $h(x)$. To be as simple as possible, I

set a linear relation as follows

$$k_{\text{on}}[h(x)] = k_{\text{on}}^0 + \kappa h_{\text{r}}(x) \tag{3.2}$$

In this equation, k_{on}^0 is the binding rate when no compression is applied and $\kappa > 0$ quantifies the increase rate when I compress completely the cell wall. The latter parameter must be positive, since I assume that the interaction with the cell wall increases with compression. The relationship between the binding rate and the compression profile may be more complex, potentially involving nonlinear saturation effects. Alternative models can be explored in future works.

3.1.4 Constitutive equations

Finally, the PDE must describe lateral diffusion along the CW in one dimension of the unbound proteins, with the additional contribution of the chemical reaction which regulates the exchange of particles between the unbound state and the bound state, which do not diffuse; the binding rate of the chemical reaction is determined by the compression profile. Moreover, the cytoplasm acts as a reservoir from which proteins can be exchanged.
So, with the assumptions previously mentioned, I get the following reaction-diffusion equations to describe the dynamics

$$\begin{cases} \frac{\partial c_{\text{u}}}{\partial t} = D\frac{\partial^2}{\partial x^2}c_{\text{u}} - (k_{\text{on}}^0 + \kappa h_{\text{r}}(x))c_{\text{u}} + k_{\text{off}}c_{\text{b}} + \alpha - \beta c_{\text{u}} \\ \frac{\partial c_{\text{b}}}{\partial t} = (k_{\text{on}}^0 + \kappa h_{\text{r}}(x))c_{\text{u}} - k_{\text{off}}c_{\text{b}} \end{cases} \tag{3.3}$$

where D is the lateral diffusion constant of the unbound proteins, $k_{\text{on}} = k_{\text{on}}^0 + \kappa h_{\text{r}}$ and k_{off} the binding and unbinding rate from the cell wall, α the incoming flux from the cytoplasm by exocytosis and β the protein loss rate by endocytosis. Equations 3.3 are linear PDE, since D, k_{on}, k_{off}, α and β do not depend on c_{u} and c_{b} . The dependence on $h_{\text{r}}(x)$, which is a given compression profile, is included in $k_{\text{on}}(x)$.
On the right-hand side of the first equation, it is clear to distinguish the three contributions to the unbound protein dynamics: the effect of diffusion (first term), chemical reaction (second and third term) and exchange with the cytoplasm (forth and fifth term). While for the second equation for the bound proteins, only the chemical reaction term is present.
Summing the two equations, it is possible to observe the global behavior of the total protein concentration $c_{\text{tot}} = c_{\text{u}} + c_{\text{b}}$, I obtain

$$\frac{\partial c_{\text{tot}}}{\partial t} = D\frac{\partial^2}{\partial x^2}c_{\text{u}} + \alpha - \beta c_{\text{u}} \tag{3.4}$$

So the evolution of c_{tot} depends on the unbound protein concentration c_{u}. If in the extreme case $c_{\text{u}} = 0$ and $\alpha = 0$, i.e. there is no unbound concentration no source rate, then the total protein concentration remains constant in space and time.
To recapitulate, all parameters of the model are reported in table 3.1.1.

3.1.5 Remarks on the validity of the model

Before going on, it is important to highlight the assumptions of the previously presented model, and the experimental consideration for this choices. Indeed, the following processes have not been taken into account :

Symbol	Description
H	Cell wall thickness at rest
h	Cell wall compression profile
h_{r}	Cell wall relative thinning
k_{on}	Cell-wall-Wsc1 binding rate
k_{off}	Cell-wall-Wsc1 unbinding rate
k_{on}^0	Cell-wall-Wsc1 binding rate with no compression
κ	Increasing binding factor related to cell wall compression
κ_{r}	Relative increasing binding factor related to cell wall compression
D	Wsc1 unbound protein lateral diffusion coefficient
α	Source rate income from the cytoplasm
β	Dissociation rate from the cell wall to the cytoplasm
$c_{\mathrm{u}}, c_{\mathrm{b}}, c_{\mathrm{tot}}$	Unbound, bound, and total protein concentration

Table 3.1.1: Parameters of the model

- The downstream signal in principle could activate the glucan synthesis. This mechanism is not essential for the formation of clusters, as proved experimentally with defective mutants in the cytoplasm tail of fission yeast (Neeli-Venkata et al., 2021) which were able to cluster even without triggering the downstream pathway. However, the cell wall thickness due to this feedback mechanism could vary of about 10% for a scale time of $\sim$ 10 *min* (Davì et al., 2018) which is comparable with the clustering behavior. This is in contrast with the assumption of a static compression profile. For this reason, for a more realistic model and more accurate predictions, these possible fluctuations of the cell wall thickness due to the cell wall synthesis can be important and should be considered.

- Yeast morphogenesis, i.e., cell growth. Indeed, due to cell expansion, the CW surface is stretched in the tangential direction with a strain rate $\sim 10^{-3}\,\mathrm{s}^{-1}$ (Davì et al., 2018; Odermatt et al., 2021). This lateral strain factor could be absorbed in the loss term β, as it corresponds to a dilution of protein concentration. Therefore, when analyzing experiments during interphase, it should be considered that $\beta = \beta_{\mathrm{cyt}} + \beta_{\mathrm{growth}}$, where $\beta_{\mathrm{growth}} \sim 0.001\,\mathrm{s}^{-1}$ is due to growth only, and β_{cyt} is due to exchange with the cytoplasm only. However, from FRAP experiments (Neeli-Venkata et al., 2021), the characteristic time of the dynamics is of the order of 10^2 s, which is slightly greater than $\frac{1}{\beta_{\mathrm{growth}}}$. Therefore, this dilution effect due to growth is not so significant.

- Protein-protein interactions. Despite the possibility for Wsc1 to form disfulde bridges, a type of covalent bond, as claimed by Kock et al. (Kock et al., 2015), this interaction does not seem to play an important role in clustering. A simple argumentation given in the article (Neeli-Venkata et al., 2021), is that as long as stress is released, clusters disappear within few minutes. This is not compatible with the idea that the aggregations were formed due to covalent interaction, since it is expected to be stronger and more stable. However, it is not to be excluded that other types of interactions between proteins that are weaker exist or the presence of an enzyme that breaks

disulfide bonds in the absence of mechanical stress. Since there is no evidence and chemical motivation for this scenario, the case of protein-protein interaction is explored only in the appendix C. Currently, it is not known if this effect is important and future research can address this question.

- The experimental density distribution of Wsc1 is polarized, as it is more concentrated at the cell tips, even in the absence of applied forces. For now, I will disregard this effect to simplify the derivation. A more detailed model, which assumes a heterogeneous influx from the cytoplasm to the cell wall and explains this polarization pattern, is examined in Appendix A. However, although this aspect may be important for accurate predictions, it is not essential for clustering behavior, as confirmed from experiments with mutant yeast, where Wsc1 could cluster even in the absence of the polarizing machinery (Neeli-Venkata et al., 2021).

After these considerations, since I want to build the most parsimonious model able to explain the clustering behavior of Wsc1, I neglect all these processes. More realistic and sophisticated descriptions will be possible in the future.
For now, I also assume the system to be strain-sensitive, meaning it senses the compression of the cell wall, and not the stress. Although stress and strain can be related by a proportionality constant when considering the elastic regime of the cell wall (Weber et al., 2015), this proportionality can be inhomogeneous along the cell wall, making stress solicitation different from compression. Since I have data relating particle concentration to relative thinning, the strain-sensitive assumption is more convenient. However, future data mapping the concentration of Wsc1, the cell wall thickness and stress around the cell could verify if this hypothesis is correct.

3.2 Model Predictions

3.2.1 Stationary solution

In this section, I study the stationary concentration of the protein, i.e. the concentration profile value at which the system relaxes after an initial compression profile. By comparing this profile with the stationary distribution obtained without compression, I can understand if protein density increases or not after mechanical strain. If the model correctly predicts clustering, I expect the in compressed region of the cell wall, the stationary concentration is higher.
In the stationary regime, 3.3 takes the form

$$\begin{cases} D\frac{\partial^2}{\partial x^2}c_{\mathrm{u}}^* - (k_{\mathrm{on}}^0 + \kappa h_{\mathrm{r}}(x))c_{\mathrm{u}}^* + k_{\mathrm{off}}c_{\mathrm{b}} + \alpha - \beta c_{\mathrm{u}}^* = 0 \\ (k_{\mathrm{on}}^0 + \kappa h_{\mathrm{r}}(x))c_{\mathrm{u}}^* - k_{\mathrm{off}}c_{\mathrm{b}}^* = 0 \end{cases} \tag{3.5}$$

where c_{u}^*, c_{b}^* and $c_{\mathrm{tot}}^* = c_{\mathrm{u}}^* + c_{\mathrm{b}}^*$, are the stationary solution which satisfies this problem. The final results of equations 3.5 yields the following relation:

$$\begin{cases} c_{\mathrm{u}}^* = \frac{\alpha}{\beta} \\ c_{\mathrm{b}}^*(x) = \frac{\alpha}{\beta}\frac{k_{\mathrm{on}}^0 + \kappa h_{\mathrm{r}}(x)}{k_{off}} \end{cases} \tag{3.6}$$

As it is remarked by the notation, while c_{u}^* is homogeneous, $c_{\mathrm{b}}^*(x)$ instead is heterogeneous since it depends on the compression profile. Indeed, in the region where the relative thinning of the CW is higher, the binding rate increases and therefore a higher concentration of bound proteins is expected. Conversely, c_{u}^* is kept constant along the cell wall thanks to diffusion and exchange with the cytoplasm by which proteins are recruited.
If I sum the two contributions given by the two species, I obtain

$$c_{\mathrm{tot}}^*(x) = \frac{\alpha}{\beta}\left(1 + \frac{k_{\mathrm{on}}^0 + \kappa h_{\mathrm{r}}(x)}{k_{\mathrm{off}}}\right) \tag{3.7}$$

Comparing this concentration with a reference value c_0, defined as the stationary concentration obtained when no compression is applied, it yields

$$\frac{c_{\mathrm{tot}}^*(x)}{c_0} = 1 + \kappa_{\mathrm{r}} h_{\mathrm{r}}(x) \tag{3.8}$$

where $\kappa_{\mathrm{r}} = \frac{\kappa}{k_{\mathrm{on}}^0 + k_{\mathrm{off}}}$ is the relative increasing binding rate compared to the total reaction rate with no strain.

Since compressed region have higher affinity with the cell wall and consequently $k_{\mathrm{on}}^0 + \kappa h_{\mathrm{r}}(x)$ increases, the total concentration is higher. Therefore, the model correctly predicts the formation of clusters in correspondence to the compressed area of the cell wall.
It is important to note that this stationary concentration is achieved regardless of the initial conditions. Therefore, if the compression is first applied and then released, the cluster disappears, as experimentally observed, as the stationary concentration value returns to c_0.
If I choose as compression profile a Gaussian curve centered on zero, variance equal to σ, and integral in space equal to $\sqrt{2\pi\sigma^2}$, I obtain the following concentration profile

$$\frac{\bar{c}_{\mathrm{tot}}}{\bar{c}_0} = 1 + \kappa_{\mathrm{r}} e^{-\frac{-x^2}{2\sigma^2}} \tag{3.9}$$

As shown in figure 3.2.1, the stationary density follows the profile of the compression as expected from relation 3.8, remarking the fact that the compressed region and the cluster region have the same characteristic size.
It is important to emphasize that the clustering behavior remains valid if either diffusion or exchange with the cytoplasm is neglected. So the two protein recruitment mechanisms are redundant. So, from the simple analysis of stationary concentration is not possible to discern the two mechanisms of protein recruitments.

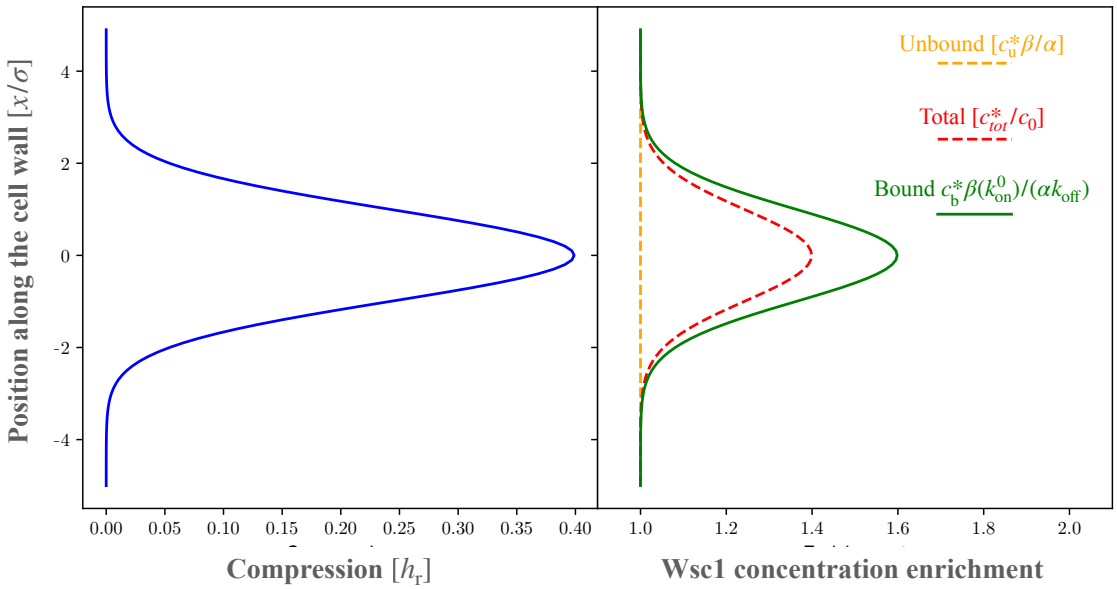

Figure 3.2.1: Predicted clustering. On the right, it is shown the Wsc1 protein density profile at stationary state after the application of a Gaussian compression profile $h_r = e^{-\frac{x^2}{2\sigma^2}}$, plotted on the left. The relation is given in the linear case by relation 3.9. The different colors represent the different population concentration, unbound (normalized with respect to the strain-free stationary state $\frac{\alpha}{\beta}$, bound (normalised with respect to $\frac{\alpha k_{on}^0}{\beta k_{off}}$) and the total concentration (normalised with respect to c_0)

3.2.2 Relative increasing rate quantification

This section deals with quantification of κ_r, which expresses the binding rate increase as the cell wall is compressed. For this purpose, we examine data from Neeli-Venkata's article (Neeli-Venkata et al., 2021), where the Wsc1-GFP fluorescence signal I at the cell tip is yielded after background subtraction and normalization with a reference signal value at the cell side. In the Neeli Venkata's article (Neeli-Venkata et al., 2021), I is reported as function of the CW relative thinning h_r. Supposing the signal proportional to the concentration value, equation 3.8 can be rewritten in terms of these experimental measurements as

$$I(h_r) = A + Bh_r \tag{3.10}$$

where A and B are respectively the intercept and the slope of the line, and they must satisfy the relation $\kappa_r = \frac{B}{A}$. To vary the thickness of the cell wall, three different processes are exploited:

- compression, when CW and enrichment is monitored as fission yeast is growing during its interphase pushes against the upper or lower cell, causing compression of the cell wall
- relaxation (or decompression), obtained by laser ablation of the neighbor cell, which consequently relaxes back and does not exert any forces on the close cell anymore.
- mating, i.e. when CW becomes thinner due to cell-cell contact before fusion

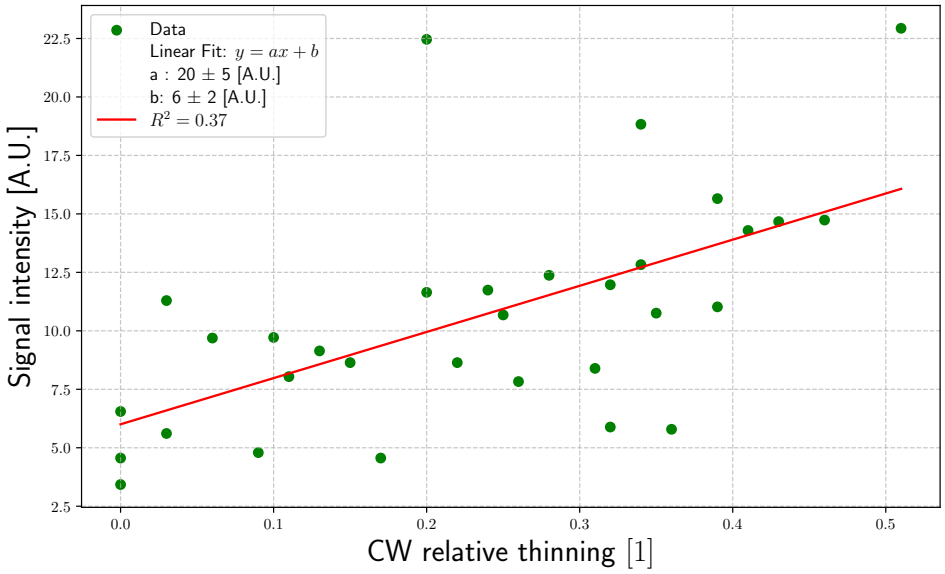

Figure 3.2.2: Linear relation between the fluorescent signal and the cell wall compression. In the panel, it is shown the scatter plot of the experimental data of fluorescent signal tagging Wsc1 protein as function of the relative cell wall compression. The results of the linear fit are reported in the legend. Error bars are neglected, since the technical noise is supposed to be smaller than biological dispersion.

However, in my analysis, I concentrated solely on compression processes, discarding mating and decompression. Indeed, mating involves chemical digestion of the cell wall, which could alter hugely the composition of this layer. Therefore, this is not an elastic deformation, and it is not clear whether cell wall density changes. Instead, decompression is obtained after a strong perturbation, like laser ablation, which requires a rapid CW mechanical equilibrium rearrangement. Consequently, data obtained during compression are closer to the stationary state than during mating and decompression processes.
After fitting data with a straight line, I obtain a relative increase binding rate of about $\kappa_r \approx 3.3$. This means that for a half-compression of the cell wall, I obtain a concentration enrichment factor of $\frac{c^*_{tot}}{c_0} \approx 2.7$.
This result, obtained purely by fitting the data, assumes only a linear relationship between Wsc1 concentration and cell wall compression and does not require the whole model presented in this chapter to be valid. However, the binding/unbinding dynamics provides an interpretation of this value as the result of the underlying interactions between molecules. In fact, the proportionality factor between the relative increase in protein density with compression is the relationship between the increasing binding rate constant κ and the total binding rate in the absence of compression $k^0_{\text{on}} + k_{\text{off}}$.
I finally remark that in order to test whether a linear relationship is sufficient to explain data even up to 0.5 of relative compression, further studies that open the possibility of non-linear effects in the Wsc1-cell wall interaction are needed.

3.2.3 Quasi-steady-approximation

Despite the simplifying assumptions regarding Wsc1 dynamics, the partial differential equations 3.3 encompass numerous dynamical parameters, including k_{on}, k_{off}, D, α, and β. This complexity poses significant problems for obtaining analytical solutions for studying the system's behavior following an initial perturbation. To address this challenge, I explore potential approximations to reduce the number of parameters. Afterwards, I assess whether the predictions made under these assumptions align with experimental observations.
First of all, to each contribution in equation 3.3, we can associate a typical relaxation time, which is the scale time necessary to reach equilibrium for the single process. For the chemical reaction, the typical timescale to get to the equilibrium is of the order of $t_{\text{on/off}} \sim \frac{1}{k_{\text{off}}}$, for diffusion $t_D \sim \frac{L^2}{D}$, where L is the typical size of the system and for the exchange with the cytoplasm is $t_{\alpha/\beta} \sim \frac{1}{\beta}$. If these time scales differ by order of magnitudes, we can apply the so called quasi-steady approximation (Goussis, 2012). This method consists in considering the fastest dynamics at the stationary state, while the system evolves according to the remaining slower processes. In the Fourier space solution, as in appendix B, this is equivalent to considering the faster mode to be released. This approximation allows writing explicit relation between variables and makes calculations simpler.

3.2.3.1 Chemical-Reaction-limited region

In this section, I study the quasi-steady-approximation by which the chemical reaction process is slower than diffusion and exchange-rate. Notice that if diffusion gets to the stationary state with concentration of unbound protein $c_{\text{u}}^* = \frac{\alpha}{\beta}$ homogeneous, also the exchange rate is at the equilibrium or the contrary. So this limit is verified whether $t_D << t_{\text{on/off}}$ or $t_{\alpha/\beta} << t_{\text{on/off}}$. In this case, PDE 3.3 can be written as

$$\begin{cases} c_{\text{u}} = \frac{\alpha}{\beta} \\ \frac{\partial c_{\text{b}}}{\partial t} = (k_{on}^0 + \kappa h(x))c_{\text{u}} - c_{\text{b}} k_{\text{off}} \end{cases} \tag{3.11}$$

It is straightforward to verify that the total concentration dynamics evolves according to

$$\frac{\partial c_{\text{tot}}}{\partial t} = \frac{\alpha}{\beta}(k_{\text{off}} + k_{\text{on}}^0 + \kappa h(x)) - k_{off} c_{tot} \tag{3.12}$$

Henceforth, the total concentration relaxation time is $\frac{1}{k_{\text{off}}}$ and it does not depend on the mechanics. This is not coherent with FRAP experiment, where it was measured a slower recovery time in the compression region of the cell wall.

3.2.3.2 Diffusion-Exchange-limited regime

In this section, I study the quasi-steady-approximation when the chemical reaction is faster than diffusion/exchange, i.e. $t_D >> t_{\text{on/off}}$ and $t_{\alpha/\beta} >> t_{\text{on/off}}$. By this assumption, chemical reaction can be considered at the stationary state, transforming equations 3.3 into

$$\begin{cases} \frac{\partial c_{\text{u}}}{\partial t} = D\frac{\partial^2}{\partial x^2} c_{\text{u}} + \alpha - \beta c_{\text{u}} \\ 0 = (k_{\text{on}}^0 + \kappa h_{\text{r}}(x))c_{\text{u}} - k_{\text{off}} c_{\text{b}} \end{cases} \tag{3.13}$$

If I consider the global dynamics of c_{tot}, I obtain an exchange-diffusion-advection equation as follows

$$\frac{\partial c_{\text{tot}}}{\partial t} = \frac{\partial}{\partial x}\left[D_{\text{eff}}[h(x)]\frac{\partial c_{\text{tot}}}{\partial x}\right] - \frac{\partial}{\partial x}\left[c_{\text{tot}} v_{\text{eff}}[h(x)]\right] + \alpha - \beta_{\text{eff}}[h(x)]c_{tot} \tag{3.14}$$

where

$$\begin{cases} D_{\text{eff}}[h(x)] = \frac{k_{off}}{k^0_{\text{on}}+\kappa h_{\text{r}}+k_{off}} D \\ v_{\text{eff}}[h(x)] = -\frac{\partial}{\partial x}\left(\frac{k_{off}}{k^0_{\text{on}}+\kappa h_{\text{r}}+k_{off}}\right) D \\ \beta_{\text{eff}}[h(x)] = \frac{k_{off}}{k^0_{on}+\kappa h(x)+k_{off}} D \end{cases} \tag{3.15}$$

can be defined respectively as the effective diffusion coefficient, velocity field and dissociation rate. It is worthy to notice that in the region that are compressed, the apparent diffusion coefficient and dissociation rate is slower since $D_{\text{eff}} \sim \frac{1}{k^0_{\text{on}}+\kappa h_{\text{r}}}$ and $\beta_{\text{eff}} \sim \frac{1}{k^0_{on}+\kappa h_{\text{r}}}$. This is due to the fact the mobile particles' fraction, i.e. $\frac{c_{\text{u}}}{c_{\text{tot}}}$ is lower since more proteins are pushed towards the bound state, and therefore it yields a slower global mobility. Differently, the velocity field is present in the zone where there is a variation of the CW thickness, since $v_{\text{eff}} \sim \partial_x \kappa h_{\text{r}}$. If I suppose a compressed region at the center, by considering the sign of v_{eff}, it is clear that the advective fluxes pull proteins from the sides to the center, favoring clustering. If the compression profile is homogeneous, instead, there is no velocity field. In this special case, denoting with h_{r} the relative thinning, I obtain a simpler equation

$$\frac{\partial c_{\text{tot}}}{\partial t} = D_{\text{eff}}\frac{\partial^2}{\partial x^2} c_{\text{tot}} + \alpha - \beta_{\text{eff}} c_{\text{tot}} \tag{3.16}$$

with

$$\begin{cases} D_{\text{eff}} = \frac{k_{\text{off}}}{k^0_{\text{on}}+\kappa h_{\text{r}}+k_{\text{off}}} D \\ \beta_{\text{eff}} = \frac{k_{\text{off}}}{k^0_{\text{on}}+\kappa h_{\text{r}}+k_{\text{off}}} \beta \end{cases} \tag{3.17}$$

If now I confront these parameters with their values at $\bar{h}_{\text{r}} = 0$, D_0 and β_0, I obtain the following relation

$$\begin{cases} \frac{D_{\text{eff}}}{D_0} = \frac{1}{1+\kappa_{\text{r}} h_{\text{r}}} \\ \frac{\beta_{\text{eff}}}{\beta_0} = \frac{1}{1+\kappa_r h_{\text{r}}} \end{cases} \tag{3.18}$$

with κ_{r} which is the same computed value of section 3.2.2. This specific relation with $h_{\text{r}}(x)$ is possible only because I suppose a linear relation with $k_{\text{on}} = k^0_{\text{on}} + \kappa h_{\text{r}}$. A summary of the model qualitative prediction after cell wall compression is shown in table 3.2.1.

However, even if $k_{\text{on}}[h(x)]$ is not known, as long as it does not depend on the protein concentration (so PDEs 3.3 are linear) in the diffusion-exchange limited regime it must be verified the following relation

$$\begin{cases} \frac{D_{\text{eff}}}{D_0} = \frac{c_0}{c^*_{\text{tot}}} \\ \frac{\beta_{\text{eff}}}{\beta_0} = \frac{c_0}{c^*_{\text{tot}}} \end{cases} \tag{3.19}$$

This condition shows that the mobility, which is related to the parameters D_{eff} and β_{eff}, is reduced where there is clustering, i.e. when the density c^*_{tot} is higher at the stationary state. This could explain a lower mobility in the region where there is compression. This is confirmed in FRAP experiments (Neeli-Venkata et

al., 2021). Moreover, in section 3.2.2, I obtain that for a relative compression of $h_r = 0.5$, the relative concentration increase is $\frac{c^*_{tot}}{c_0} = 3$. This means that for the same CW thickness value the effective mobility, D_{eff} and γ_{eff}, are decreased by a factor 3 compared the rest state according to relation 3.19. This is consistent with the experimental results for the diffusion value (Neeli-Venkata et al., 2021). However, in their analysis, the researchers neglect the exchange process with the cytoplasm. Therefore, a new analysis that can differentiate between the two recruitment mechanisms should be conducted.

Symbol	Description	Prediction
c^*_u	Unbound concentration at stationary state	No change
c^*_b	Bound concentration at stationary state	Increase
c^*_{tot}	Total concentration at stationary state	Increase
D_{eff}	Effective diffusion constant	Decrease
β_{eff}	Effective exchange rate	Decrease

Table 3.2.1: Model predictions after cell wall compression

3.3 Comparison with the literature

This section provides a comparative analysis of my work against other clustering mechanisms discussed in the literature. Since my mathematical framework is for general particle dynamics, I do not restrict this analysis to the mechanosensing context, such as focal adhesion integrin protein (see chapter 2), but I also consider other clustering behaviors, e.g. for chemotaxis membrane receptors in *E. Coli* (Recouvreux and Lenne, 2016) and other non-biological systems.
The main result of my work is that clustering is obtained considering a combination of heterogeneous protein binding with the substrate, in my case the Wsc1 with the CW, with a protein recruitment process, lateral diffusion and/or exchange with a reservoir. This output is coherent with kinetic trapping models (Sánchez and Wio, 1997; Viljoen and Uebing, 1997), i.e. system of freely diffusing particles that can be trapped in specific absorbing sites of the domain.
It is important to remark that in my model the clustering is triggered by the activator field, in my case the compression profile, which makes the binding rate non-homogeneous and the consequent concentration increase follows the spatial field. This is in contrast with other clustering proteins, where cluster can arise only at a certain distance between each other (Greenfield et al., 2009) and only for a given critical size (Ali et al., 2011; Das et al., 2018; F. Zhang et al., 2024). This difference can be attributed to the omission of protein-protein attractive and self-repulsive interactions, which may promote the fusion of adjacent clusters but also disfavor the formation of excessively large clusters.
Moreover, compared to mechanosensitive integrin clustering models (Besser and Safran, 2006), an initial nucleation is not required. Hence, stochastic fluctuations do not seem to play a role. Another characteristic of my model is that it does not require feedback loop neither from inside the cell, for example building a preferential microtubules pathway which affects the incoming source rate (Muller et al., 2016), neither from cascade reactions in the membrane (Welf et al., 2012).

Moreover, the fact that only one protein species in two possible states is involved, avoid reproducing more complex behavior, where region of depletion can form within the region of the cluster (Ali et al., 2011).
Another striking regard concerns the mobility of the protein in the clusters. Indeed, where the protein forms clusters, the mobility is reduced. It was also already proved that there is a reduced diffusion in the region of the trapping binding sites (Ali et al., 2011; Sánchez and Wio, 1997; Viljoen and Uebing, 1997). My work confirms this behavior and extends this concept to any possible mechanism of mobility, e.g. the exchange with the cytoplasm. In general, if we had considered other protein mobility mechanisms that are present only for the free-state population, e.g. advection fluxes, the collective mobility would be affected as the fraction between the bound-unbound concentration is altered.

3.4 Conclusion

In this work, I propose a simple model to reproduce a protein clustering behavior triggered by CW compression. The model takes into account two states of the protein, unbound or bound to the CW. Only for the former, I consider lateral diffusion along the cell wall and exchange of proteins with the cytoplasm. Furthermore, I assume that the binding rate is enhanced by compression. With these assumptions, the model reproduces the concentration enrichment of the protein in the compressed regions of the CW, as observed in experiments.
Moreover, assuming that chemical reactions reach equilibrium quickly, the model predicts for the global behavior of the protein an effective diffusion coefficient and exchange rate that is reduced by compression. This decrease is inversely proportional to the cell wall thinning. Data analysis from FRAP experiments confirms that in the cluster regions, the dynamics occur on a longer timescale, consistent with the predictions of my model.
However, from the FRAP characteristic recovery time value only, it is not possible to determine whether the protein recruitment is due to diffusion, exchange with the cytoplasm or both. For this reason, I work in the next chapter on developing a new inference method for FRAP capable of discerning different types of dynamics.

CHAPTER

FOUR

A NOVEL INFERENCE METHOD FOR FRAP

This chapter aims to provide a novel inference method for the FRAP experiment that is able to estimate diffusion, reaction, and exchange parameters from imperfect data where the signal-to-noise ratio is low, the spatial observational window is restricted, and photobleaching during imaging is not negligible. These conditions are typical for Wsc1 FRAP experiments. For this purpose, I attach the draft of a future paper, written in collaboration with my supervisors, A. Boudaoud[1] and A. Fruleux[2], and experimentalists, C. Municio-Diaz[3,4] and N. Minc[3,4]. The experiments were conducted by C. Municio-Diaz, while the data analysis and theoretical work were performed by me under the supervision of A. Boudaoud and A. Fruleux. A summary of the content is given of the content is given in section 4.2, motivations for this work in section 4.3, results of the inference method in section 4.4 and the conclusion in section 4.5. The theory and experimental protocols are found in Section 4.6, while supplementary figures are found in Appendix D. Before submitting the paper, an implementation of the inference method is expected to be finished as a Fiji plugin, HiFRAP. At this time, this macro is not finalized. So the results of the analysis here are obtained by python scripts, except for subsection 4.4.7, where a demo version of HiFRAP was used. Before delving into the article, I first introduce the inverse problem: the challenge of estimating kinetic parameters from sampling data. This discussion provides some context useful for understanding the novel problem addressed in this chapter.

4.1 Introduction to the inverse problem

4.1.1 Problem formulation

In chapter 3, I developed a mathematical model able to predict protein dynamics. This means that, knowing the initial condition, I am able to reproduce the spatial-temporal concentration evolution of the proteins. However, the result is dependent on the choice of the parameters, such as the diffusion coefficient value and exchange rate with the cytoplasm. In the absence of a molecular model for

[1]LadhyX, CNRS, École Polytechnique
[2]LPTMS, CNRS, Univeristé Paris Saclay
[3]Université Paris-Cité, CNRS, Institut Jacques Monod
[4]Equipe Labellisée LIGUE Contre le Cancer, 75013 Paris, France

Wsc1 protein, able to predict the exact interactions in the cellular environment, these parameters are not known *a priori*.
For this reason, in this chapter I focus on a data-driven approach: from sampling the spatial temporal concentration, I want to infer the parameters of the model. This scenario is known as the inverse problem or parameter identification (G. Zhang et al., 2023), i.e. estimating the underlying model parameters from observed data. Solution of this problem are applied in different contexts: geophysical and medical imaging, computational photography and computational microscopy (Ongie et al., 2020). In this setting the concentration $c(x,t)$ is not directly measured, but indirectly with the fluorescent signal $I(x,t)$, by means of the experimental device. Henceforth, the model prediction should be affected by the parameters describing the experimental signal acquisition. This issue is dealt in section 4.6.3. I define $\mathcal{M}$ as the operator that maps the model parameters θ to the data vector $\vec{Y}^{DATA}$. The goal is to construct the inverse function, $\mathcal{M}^{-1}$, such that from the observed data, it is possible to infer with an estimation θ_{est} the true parameter of the system θ_{true}. However, the inverse operator, contrary to the direct operator, is not always well-defined since it is not guaranteed that a solution exists, and it is unique.

4.1.2 Experimental data are noisy

As it is explained in section 1.2, data collected by the experimental device includes a certain degree of uncertainty due to stochastic noise. For this reason, the inverse function $\mathcal{M}^{-1}(\vec{Y}^{DATA})$ is inherently stochastic. This means that the output of this operation, θ_{est} is not deterministic but rather follows a probability distribution. However, to impose a useful inference method, i.e. a method from which it is possible extract information on θ_{true}, the following criteria are required (Ronceray, 2024)

- consistency: in the limit of infinite sampling, i.e. with an infinite number of points, the estimated value should coincide with the true value (unbiased estimation)
- control: the error on the estimated parameter can be estimated from data
- efficiency: the error should converge fast to the true value
- robustness: the error should remain small even with imperfect data, such as outliers.

These criteria henceforth will be leading the choice of the inference method.

4.1.3 Variational method

To address the stochasticity of the experimental data with the previous criteria, it is common to resort to variational methods (Vogel, 2002). Specifically, solving the inverse problem can be approached by reducing it to a minimization problem. This method involves finding the parameters that minimize a distance measure d between the observed data $\vec{Y}^{DATA}$ and the noiseless model predictions $\vec{Y}^{TH}$. The

objective function for this minimization problem is a distance d between data and the observed value and θ_{est} is obtained as solution to

$$\min_{\theta} d(\vec{Y}^{DATA}, \vec{Y}^{TH}(\theta)) \tag{4.1}$$

An example possible choice for the function d is the sum of the square of residuals $||\vec{Y}^{DATA} - \vec{Y}^{TH}||^2$ (Johnson and Faunt, 1992), where the notation $||\cdot||$ refers to the sum of the squares of the elements of the vector. This formulation is known as the least squares method.

However, for complex models where the number of parameters is equal to or exceeds the number of data points, the problem is typically ill-posed. In such cases, the least squares solution may not be unique, leading to multiple potential parameter sets that fit the data equally well. To address this issue, additional constraints or regularization terms are introduced to stabilize the solution and ensure that it is well-posed. One common approach is to add a penalty term to the objective function. This penalty term can take the form of regularization that constrains the solution space, often by incorporating prior knowledge or preferences about the parameters. A regularized minimization problem is generally formulated as:

$$\min_{p} d(\vec{Y}^{DATA}, \vec{Y}^{TH}) + p(\theta) \tag{4.2}$$

where $p(\theta)$ is the regularization function, such as, L1 Regularization (Lasso), which promotes sparsity in the parameter estimates or L2 Regularization (or Tikhonov), which smoothly suppresses the less relevant parameters (Aggarwal et al., 2020). By incorporating such regularization terms, the inverse problem can be made more tractable, possibly ensuring that the solution is unique and stable even when the model complexity is high or the data is limited.

In the following section, I will illustrate how inference method techniques can be applied to experimental data from FRAP in order to infer dynamical parameters for a reaction-diffusion model in the case of imperfect experimental condition, with noisy data, restricted spatial window and low number of frames.

4.2 Abstract of the article

Fluorescence recovery after photobleaching (FRAP) is broadly used to investigate the dynamics of molecules in cells and tissues, notably to quantify diffusion coefficients. FRAP is based on spatiotemporal imaging of fluorescent molecules of following initial bleaching of fluorescence in a region of the sample. Although a large number of methods have been developed to infer kinetic parameters from experiments, it is still a challenge to fully characterize molecular dynamics from noisy experiments in which diffusion is coupled to other molecular processes or the initial bleaching profile is not perfectly prescribed. To address this challenge, we have developed HiFRAP to quantify reaction (or exchange)-diffusion kinetic parameters from FRAP with imperfect experimental conditions. HiFRAP is based on the variable projection method and is implemented as a Fiji plugin. To the

best of our knowledge, HiFRAP offers features that have not been combined together: making no assumption on the initial bleaching profile, which does not need to be known; accounting for bleaching during imaging and for limitation of the optical setup by diffraction; inferring several kinetic parameters from a single experiment, providing errors on parameter estimation, and testing model goodness. Our approach is applicable to other dynamical processes described by linear partial differential equations, which could be useful beyond FRAP, in experiments where the concentrations fields are monitored over space and time.

4.3 Review on FRAP inference methods

Cells and tissues are the place of permanent transport and transformation of matter. At cellular level, trafficking, binding and unbinding, or diffusion, are essential in the self-organisation of the cell, for instance. At multicellular level, diffusion, directed transport, and consumption of morphogens are key to set morphogen distributions and provide positional information during organism development. Several methods have been developed to assess such molecular dynamics, including fluorescence recovery after photobleaching (FRAP), fluorescence spectroscopy, or single-particle tracking (Y. Chen et al., 2006). Among these, FRAP appears as the most widely used method (Y. Chen et al., 2006; Ishikawa-Ankerhold et al., 2014; Jacobson et al., 1987; Lorén et al., 2015; Reits and Neefjes, 2001), likely because the microscopy setup is technically less demanding.

FRAP is designed to study the dynamics of fluorescent molecules, by monitoring the response to an initial perturbation. Molecules are first photobleached by strong and short light pulses in a region of the sample, often circle- or square-shaped. Fluorescence is then followed over space and time, by time-lapse imaging with a microscope. Typically, fluorescence (partially) recovers its initial level, and the pattern of recovery is informative on the underlying dynamics. When molecules only undergo diffusion, the timescale of fluorescence recovery is a function of the diffusion coefficient and of the size and shape of the initially bleached (or FRAPped) region (Ishikawa-Ankerhold et al., 2014; Lorén et al., 2015; Reits and Neefjes, 2001). Accordingly, FRAP is routinely used to determine diffusion coefficients. When molecules only undergo binding and unbinding to immobile cellular substrates, then the timescale of fluorescence recovery is the inverse of the binding rate (Ishikawa-Ankerhold et al., 2014; Lorén et al., 2015; Reits and Neefjes, 2001). Here, we consider more complex situations where several molecular processes are coupled.

At cellular level, FRAP has also been used to investigate protein synthesis (Kourtis and Tavernarakis, 2017), dynamics of molecular condensates (Taylor et al., 2019), mechanosensing (Neeli-Venkata et al., 2021), transport of mRNA (Ciocanel et al., 2017), or cell adhesion (Erami et al., 2016; Hardin, 2011). At tissue level, FRAP has been used to assess diffusion of morphogens (Recouvreux et al., 2024) or expansion of the extra-cellular matrix (Lamiré et al., 2020). FRAP is also used in material science, for instance to characterise pharmaceutical compound (Deschout et al., 2014; Lorén et al., 2015). Despite the practical importance of FRAP, a universal method to analyse and interpret FRAP data is still lacking (Lorén et al., 2015). Here, we contribute to tackling this issue.

The classical method to determine diffusion coefficient is based on the theoretical calculation of average concentration in the bleached region and fits to the recovery curve of fluorescence in that region (Axelrod et al., 1976; Kang et al., 2012). Although the classical method is easy to implement, it assumes the initial bleaching profile to be perfectly known, it does not use the information available in spatial variations, and it is difficult to distinguish diffusion from other processes based on this method (Axelrod et al., 1976). These limitations prompted the development of more sophisticated methods. Methods that do not require the knowledge of the bleaching profile are based on the decomposition of fluorescence level into Fourier modes and fit the temporal decay of mode amplitude to theoretical solutions, in linear (Elowitz et al., 1999; Zarabadi and Pawliszyn, 2015), in axisymmetric geometry (Jönsson et al., 2008), or without assumptions on geometry (Berk et al., 1993). Methods that use all spatial information to improve precision use fits of the spatiotemporal concentration field to analytical (Deschout et al., 2010) or numerical (Blumenthal et al., 2015; Papáček et al., 2013) of the diffusion equation, the former being restricted to rectangular initial bleaching profile and the latter allowing initial bleaching profile of arbitrary shape. Other studies built methods to account for the effect of boundary conditions on diffusion (Taylor et al., 2019), for diffusion on curved surfaces (Bläßle et al., 2018; Klaus, 2016), or for anomalous diffusion (Geiger, 2021; Yuste et al., 2014).

Several studies have addressed the use of FRAP to determine the kinetic parameters of chemical reactions, binding/unbinding dynamics, or exchanges between compartments, which all formally amount to chemical kinetics. In general, these studies directly deduce constants from average pre-bleaching fluorescence and recovery time of average fluorescence in the bleached area (Kourtis and Tavernarakis, 2017; Lele et al., 2006; McNally, 2008; Tsibidis, 2009), possibly accounting for rapid diffusion before the reactions take place. However, there are discrepancies between values of kinetic parameters according to the model used (Mueller et al., 2010) and it is difficult to disentangle reactions from diffusion (Sprague and McNally, 2005).

An another line of investigation has accounted for the coupling between reactions and diffusion. It is possible to solve numerically reaction-diffusion in complex realistic geometries to simulate FRAP and investigate changes in qualitative behaviour according to parameters (Cowan and Loew, 2023). To obtain kinetic parameters, one option is to use fluorescence recovery in the bleached area or in the region of interest and to fit analytical recovery curves of several experiments with varying sizes of bleached region, which provides enough information to derive several parameters (Goehring et al., 2010; Kang and Kenworthy, 2008; Kang et al., 2010). Another option is to use all spatial information and fit the spatiotemporal concentration field (fluorescence level) to analytical (Ciocanel et al., 2024; Geiger, 2021) or numerical (Montero Llopis et al., 2012; Röding et al., 2019; Tolentino et al., 2008; Wu et al., 2008) solutions of reaction-diffusion equations (for one or two species, according to the problem of interest). We note that these methods are constrained by the need to know the initial condition, i.e. of the profile of fluorescence following initial bleaching. Using Fourier coefficients of the fluorescence field (Berkovich et al., 2011) like in some of the methods to infer diffusivity already mentioned, it was possible to get rid of this constraint, at the price of averaging several experiments together to average out noise. Here we aim at going

beyond limitations by noise and the knowledge of the bleached profile. Indeed, the bleached profile is difficult to control experimentally (Berk et al., 1993) and discrepancies with the assumed profile generally lead to a misestimation of kinetic parameters (Goehring et al., 2010; Kang et al., 2012).

A few studies accounted for other couplings, such as advection (directed transport) and diffusion (Axelrod et al., 1976), advection-reaction (Saito et al., 2022), or advection-reaction-diffusion (Ciocanel et al., 2017), with similar limitations to those previously discussed. Here we limit ourselves to reaction-diffusion, but we note that our method is generalisable to any processes described by linear partial differential equations. In addition, we account for photobleaching during imaging, i.e. the bleaching of fluorophores due to their excitation for time-lapse imaging, following a few studies that inferred the rate of photobleaching during imaging from experimental data (Jönsson et al., 2008; Papáček et al., 2013; Röding et al., 2019).

Altogether, we aim at building a method to infer from FRAP the kinetic parameters of a process described by a reaction-diffusion equation from single experiments. We assume that experiments are noisy, that the initial bleaching profile is unknown, and that photobleaching occurs during imaging. We also account for diffraction-limited resolution of the optical setup. In the following, we formulate the problem and propose a systematic method to minimise the cost function. We validate and optimise the approach on synthetic data. Finally, we present the implementation of the approach as an ImageJ macro and illustrate it with experimental data on the Mtl2 membrane-localised protein in fission yeast (Cruz et al., 2013).

4.4 Results and Discussion

4.4.1 General framework in the case of pure diffusion

FRAP experiments involve imaging at regular intervals a region of interest containing the initially bleached (FRAPped) domain. The quantity of light emitted from the sample is proportional to the local concentration of fluorescent molecules, as long as saturation of detectors is avoided. However, imaging the sample also results in photobleaching, so that fluorescence is attenuated by a constant factor after each image, an effect that we call intrinsic bleaching in the following. The optical setup results in the spatial smoothing of the light pattern due to diffraction, which is characterised by the point-spread function of the microscope. The recorded signal results from three contributions. The first contribution is proportional to the concentration of fluorescent molecules, provided appropriate tuning of excitation laser and detector gain; it contains a noisy part due to the statistical fluctuations of the number of these molecules in a small volume. The second contribution originates in technical noise, mostly associated with the detector. The third contribution is a background homogeneous signal associated with the detector. Accordingly, the recorded signal is a smoothed version of the field of fluorophore concentration, combined with noise and shifted by a background intensity. In HiFRAP, we account for point-spread function, photobleaching during imaging due to imaging, background intensity, and noise. The time-lapse data are assumed to be a temporal sequence of square images. The signal to be analysed

is sampled n_t times after every time interval Δt, over $n_x \times n_x$ square pixels of side length Δx.

For the sake of simplicity, we introduce and validate HiFRAP assuming that the underlying dynamics is set by diffusion only. We generalise our approach to reaction-diffusion in Section 4.4.6. We illustrate our approach in 2 dimensions, although it is also applicable to other dimensions. The concentration of fluorophores $c(x, y, t)$ is a function of spatial coordinates (x, y) and of time t. It is a solution of the diffusion equation

$$\partial_t c = D_{\text{true}} \nabla^2 c, \tag{4.3}$$

where D_{true} is the true diffusion coefficient, ∂_t is the partial derivative and with respect to time and ∇^2 the Laplace operator. Our goal is to provide the best estimate D_{est} of the diffusion coefficient.

When photobleaching during imaging is not negligible, homogeneous regions of the sample (far from the FRAPped domain) show fluorescence decaying by a factor $\rho_i = \exp(-\varepsilon t_i/\Delta t)$, where ε is the decay rate per image, t_i is time, and Δt is the time interval between two consecutive images. Accordingly, the theoretical solution of the diffusion equation (4.3), $c(x, y, t_i)$ should be multiplied by this factor ρ_i. Photobleaching, however does not affect the background intensity. The background value is supposed to be perfectly known from the average signal of a sample-free area while the decay rate per image ε can be estimated either independently from the dynamical parameters in considering a control area distinct from the bleached (FRAPed) one as explained in section 4.4.7, or inferred altogether with the dynamical parameters as discussed in section 4.4.6.

Figure 4.4.1**A** shows an example of synthetic dataset generated by solving numerically the diffusion equation (4.3); concentration is spatially smoothed to mimic the effect of diffraction and account for the point-spread function, see Section 4.6.6 for details. The region of interest is a square of side length L and the FRAPped domain is a square of side length $\ell = L/3$ by setting the concentration of fluorophores is set to 0 at $t = 0$. The first row shows the simulated spatial profile of fluorophore concentration, which becomes smoother and converges to the initial density over time, as could be expected. The second row shows a microscope-like time-lapse imaging, obtained from the simulated (true) concentration field by adding an uncorrelated Gaussian random variable corresponding to technical noise and applying a Gaussian spatial filtering corresponding to the point-spread function of the optical setup, see Section 4.6.6. In the following, we use such synthetic data to test our method and estimate the precision of estimated diffusion coefficient, D_{est}, with respect to its true value, D_{true}.

4.4.2 A method to infer parameters from FRAP experiments

HiFRAP estimates kinetic parameters such as diffusion coefficient independently of any assumptions on the initial bleaching pattern. We use the $N_{\text{tot}} = n_x \times n_x \times n_t$ measurements of the FRAP time-lapse imaging. Because the amount of information contained in our data is finite while initial conditions are fields and belong to a space of infinite dimension, an infinity of initial conditions may give rise to the same measured data. Nevertheless, using singular value decomposition (SVD), we found that only a small number of degrees of freedom of the initial

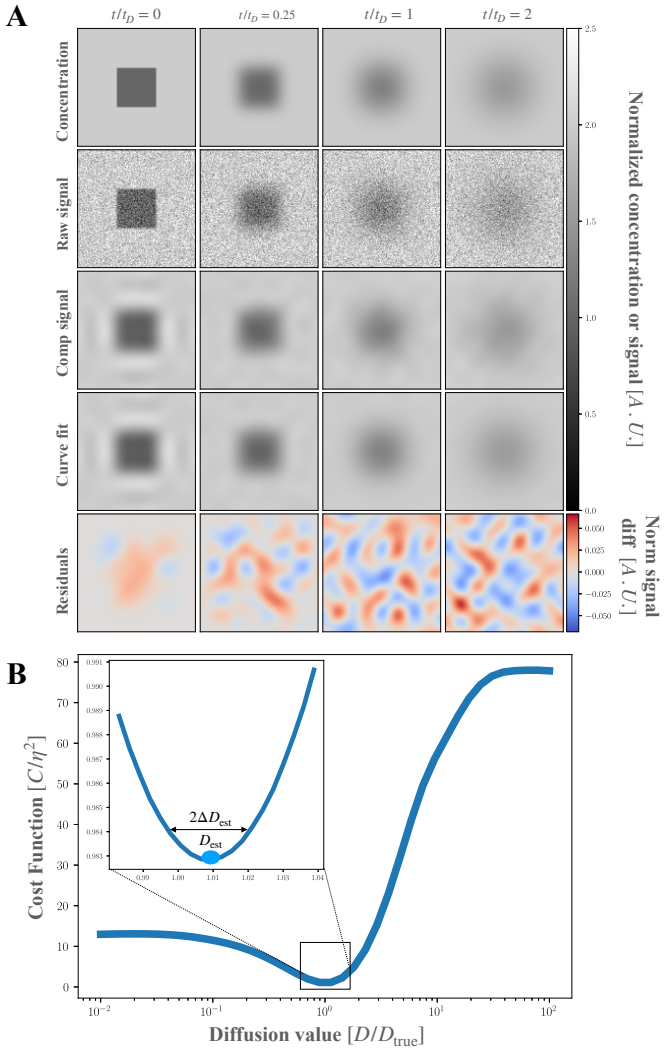

Figure 4.4.1: Inferring the diffusion coefficient from simulated FRAP. **A.** A square region of interest of side length L is tracked and a central square region of side length $\ell = L/3$ is FRAPped at $t = 0$. From top to bottom: concentration of fluorophores as predicted numerically, microscope-like synthetic data accounting for diffraction and technical noise, compressed synthetic data, concentration field fitted by HiFRAP, and residuals of the fit. From left to right: snapshots from $t = 0$ to $t = 2t_D$, where $t_D = \frac{\ell^2}{16 D_{\text{true}}}$ is taken as a unit of time. Gray- and color-scales indicate the concentration or signal intensity normalised by the drop in concentration ΔI at $t = 0$ in the FRAPped square. Dark (blue) to bright (red) indicate low to high concentration or signal. The number of pixels is $n_x \times n_x = 121 \times 121$, the number of time frames is $n_t = 15$, and the amplitude of noise is $\frac{\eta}{\Delta I} = 0.25$. For other parameters, default values are given in Section 4.6.6. **B.** Modified cost function C (normalised by noise amplitude η) as a function of fitting diffusion coefficient D (normalized by its true value D_{true}), with a magnification of the neighbourhood of the minimum of C in the inset. The cost function is minimal at D_{est}, which is close to D_{true}, up to an estimated error ΔD_{est}. The decay rate per image due to photobleaching is set to $\varepsilon = 0$.

pattern affects subsequent measurements. We used this property to fit a theoretical model to data by minimising a cost function related to the differences between observed dataset and theoretical solution. The model is built from the solution for (4.3) and accounts for the point-spread function (see Section 4.4.1 for more details). Optimisation is implemented in two steps: first fitting initial conditions and then estimating kinetic parameters (illustrated here with the diffusion coefficient).

In practice, the SVD is computationally expensive when directly used for datasets of size N_{tot} of the order of 10^5 to 10^7 because it is applied to matrices of size $N_{\text{tot}} \times N_{\text{tot}}$. To enable an interactive Fiji plugin, we reduced the computational cost by compressing the data. This is performed with the discrete Fourier transform and enables reducing the dataset size to $N = n_q \times n_q \times n_t$. We found that n_q in the range 5-9 is sufficient to obtain good estimates of kinetic parameters, as shown in Section 4.4.4, so that the compressed dataset has a size N of the order of 10^3 to 10^4. The compressed general solution to the diffusion equation (or to any linear partial differential equation such as reaction-diffusion, for given kinetic parameter) as a matrix G of size $N \times N$ multiplying the compressed initial condition (at $t = 0$), which has size $n_q \times n_q$. The SVD decomposition is applied to the matrix G, which yields ad-hoc modes, associated each to a singular value, and we neglect modes with a singular value smaller than a threshold related to machine precision. This allows to describe solutions for all initial conditions without unnecessary details (below machine precision). By using a least square minimisation of the difference between theoretical solution and observed data, we determine the best initial condition for given kinetic parameters (here diffusion coefficient D). The cost function is then given by the sum of squared residuals (difference between observed data and theoretical solution with the best initial condition) normalized by the effective degrees of freedom, see Section 4.6.2. We then minimize the cost function with respect to the kinetic parameters. In the case of diffusion only, minimisation with respect to D is performed using Brent's method (Brent, 2013). This numerical method requires a well-defined initial search interval to identify within this range a solution (see section 4.6.2 for details). Panel **A** of Figure D.9 illustrates how the diffusion value changes with each minimization step. The results highlight that a search interval spanning several orders of magnitude can lead the algorithm to converge at local minima, far from the true value. This is further evident in the cost function plot shown in Panel **B** of Figure D.9, where the diffusion value is approximately $D \sim 10^3 D_{\text{true}}$. For this reason, to choose a good search interval, we evaluate the cost function on a grid $D_{\text{grid}} = [0, 10^{-2}, 10^{-1}, 1, 10, 10^2]\frac{\ell^2}{T}$, where ℓ is the FRAPped domain side length and T is the total acquisition time. The chosen interval $[a, b]$ (with $a, b \in D_{\text{grid}}$) is the smallest interval such that $D_{min} \in [a, b]$, where D_{min} is the minimum value of the cost function along this grid ($D_{\text{min}} = a$ only if $D_{\text{min}} = 0$ and $D_{\text{min}} = b$ only if $D_{\text{min}} = 10^4\frac{\ell^2}{T}$). Notice that for the latter value of diffusion the recovery time would be much smaller of the time step ($t_D \sim 10^{-2}\Delta t$), hence the time resolution would not be sufficient to have a good estimation. The cost function minimisation of multiple kinetic parameters is described afterwards in section 4.4.6.

HiFRAP is illustrated with synthetic data in Figure 4.4.1. In panel **A**, the two first rows are the true concentration of fluorophores and the simulated microscope-like images. For our analysis, we compress the microscope-like images (third row)

to which we fit the model (fourth row), obtaining relatively small residuals (fifth row). In panel **B**, we plotted the cost function (after optimizing the initial condition) as function of the fitting parameter D for the diffusion coefficient. The estimated diffusion coefficient D_{est} is defined as the value of D that minimizes the cost. We use the curvature of the cost function (inset in panel **B**) and noise amplitude to estimate the uncertainty ΔD_{est} on the diffusion coefficient, see Section 4.6.2 for details. Here, the relative uncertainty $\Delta D_{\text{est}}/D_{\text{est}} = 0.01$ is small. Finally, we test the validity of the model by examining whether residuals are normally distributed, which is implemented using the Shapiro-Wilk and Kolmogorov-Smirnov tests (Berger and Zhou, 2014; Shapiro and Wilk, 1965), see Section 4.6.2. Here we find a pvalue from Shapiro and Kolmogorov test of 0.37 and 0.81 respectively, showing that diffusion model is a good model for these data, as could be expected.

4.4.3 Validation on synthetic data

To extensively test the validity of the inference method, we applied HiFRAP to a collection of 200 synthetic datasets for each of 6 values of noise, with exactly the same parameters as those in Figure 4.4.1 but with different realisations of noise. For each synthetic dataset, we estimated the coefficient D_{est} and its error ΔD_{est}. For the collection, we computed the average estimate $\langle D_{\text{est}} \rangle$ (the brackets $\langle\,\rangle$ stand for average over the collection) and the empirical error over $\Delta D_{\text{emp}} = \sqrt{\frac{n_{\text{ds}}}{n_{\text{ds}}-1}\langle (D_{\text{est}} - D_{\text{true}})^2 \rangle}$ (n_{ds} stands for the number of datasets), which assesses the statistical difference between estimated parameter and true parameter. The graphs in Appendix D (Figure D.8), where the average estimated diffusion value $\langle D_{\text{est}} \rangle$ and the empirical error ΔD_{emp} are plotted as function of the number of datasets n_{ds}, confirm that $n_{\text{ds}} = 200$ is sufficient to reach the convergence of these two parameters.
In Figure 4.4.2, we plotted the estimated diffusion coefficient D_{est} and estimated uncertainty ΔD_{est} as a function of noise strength. Panel **A** shows that the distribution D_{est} is well centered around its true value D_{true}. The standard deviation of this distribution increases with the noise amplitude η and the coefficient of variation $\Delta D_{emp}/D_{est}$ reaches values comparable to 1 for noise strengths such that $\eta/\Delta I \sim 10^{-2}\sqrt{N_{\text{tot}}} \simeq 4$, where ΔI is the amplitude of the drop in intensity following initial photobleaching. For such high noise, the distribution appears bimodal with a few estimates D_{est} gathering around $D_{\text{est}} = 0$, for which the estimation has clearly failed. This inefficacy is due to an incorrect choice of the initial search interval that does not include the true value, as well as the cost function being more jagged and less smooth under high noise conditions, as shown in Figure D.1 (Appendix D), making it more prone to getting trapped in local minima. In section 4.4.5, I present a more robust method for the choice of this search interval in order to avoid outliers around $D_{\text{est}} = 0$. Panel **B** shows that the estimated error ΔD_{est} agrees well with the empirical error ΔD_{emp}, validating the estimation of error from a single dataset. Outliers in the distribution of ΔD_{est} appear for high noise, consistent with the misestimation of diffusion coefficient at such noise levels. Overall, HiFRAP provides good estimates of the diffusion coefficient and of its error from a single experiment.

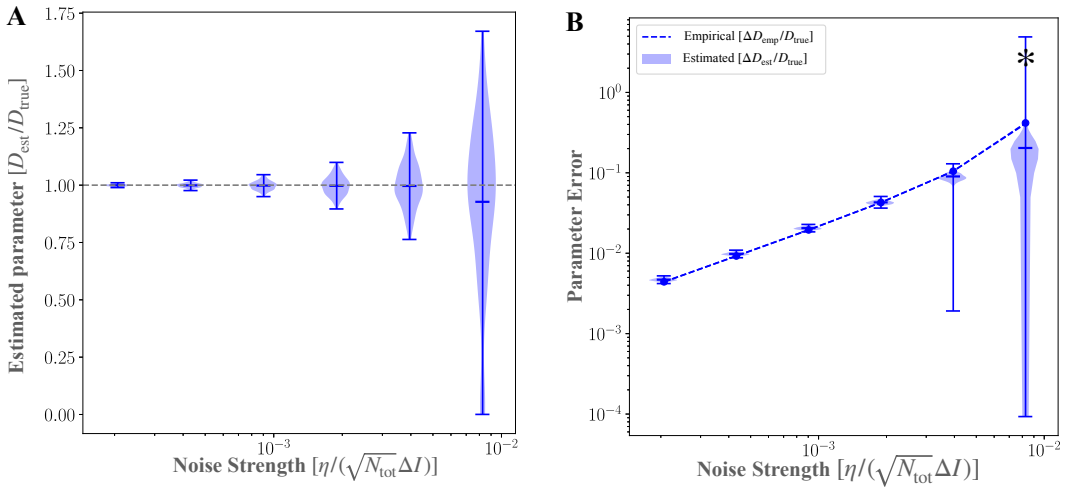

Figure 4.4.2: Validation of HiFRAP on a collection of synthetic data. A Estimated diffusion coefficient D_{est} and **B** estimated uncertainty ΔD_{est} and empirical error ΔD_{emp}. The quantities are all normalised by the true diffusion constant D_{true} and plotted as a function of the normalised noise amplitude $\eta/(\Delta I\sqrt{N_{\text{tot}}})$, where η is noise amplitude, ΔI is the drop-off intensity upon initial photobleaching, and N_{tot} dataset size (number pixels multiplied by number of time frames). The highest value of normalised noise corresponds to a noise to signal ratio of about 4.7. Violins represent distributions of D_{est} and ΔD_{est} while the ticks highlight average and extreme values. The dashed gray line in **A** represents the reference value $D_{\text{est}}/D_{\text{true}} = 1$, while the dashed blue line in **B** corresponds to ΔD_{emp}. The number of realisations is 200 for each value of noise strength and the decay rate per image due to photobleaching is set to $\varepsilon = 0$. Where an asterisk is present, the computation of the error was not possible for 7 out of 200 datasets.

4.4.4 Optimisation of experimental and analysis parameters

To optimize the estimates of kinetic parameters (here the diffusion coefficient), we aim at tuning accessible parameters in experiments — side length of FRAPed region ℓ, number of time frames n_t, and delay between frames Δt — and in analysis — number of modes n_q kept for the compression. We implicitly assume the space resolution, Δx, to be constrained by the microscope used and the side length of the region of interest, L, to be constrained by the size of the system and its spatial variations — the region of interest should be as big as possible while sufficiently homogeneous. The bleaching size ℓ and the number of modes n_q influence the amount of useful spatial information. To be optimal, ℓ should be large enough for the perturbation in fluorescence associated with FRAP to be of significant weight compared to noise, whereas ℓ comparable to L leads to a loss of spatial information associated with the boundaries of the FRAPed region. We found that the error on estimation of the diffusion coefficient is minimal around $\ell \sim L/3$ in the case of a square FRAPped region. Concerning the number of modes kept in the discrete Fourier transform, fair estimates are reached for $n_q \geq 5$ (Figure D.3). Accordingly, we took $\ell = L/3$ and $n_q = 9$ in all our analyses, except when specified otherwise.

The time resolution of experiments may be constrained by the sample im-

aged, for instance when there is phototoxicity. Here we only consider constraints due to the optical setup, which are mostly associated with photobleaching during imaging. The intensity of the observed signal decays with the number of images acquired, proportionally to $e^{-\varepsilon(n_t-1)}$, so that the signal quickly vanishes when n_t increases beyond $1/\varepsilon+1$. We therefore choose $n_t = 1/\varepsilon+1$. Concerning the choice of the time step Δt between two images, we note that the temporal decay rate due to photobleaching is $\varepsilon/\Delta t$, while the relaxation (to equilibrium) rate due to diffusion is the inverse of the diffusion time $t_D = \ell^2/D/16$ — defined as the time at which the standard deviation of the position of a Brownian particle reaches half the side length of the FRAPed region. If the decay due to photobleaching is high, then fluorescence disappears before it is observed diffusion is not observed, whereas if the decay rate due to photobleaching is low, most of the images are taken after diffusion has homogenised concentrations and these images are not informative. As a consequence, we expect the optimal delay between images to correspond to $\varepsilon/\Delta t \sim 1/t_D$. To further test this conclusion, we plotted in Figure 4.4.3 the normalized empirical error $\Delta D_{\text{emp}}/D_{\text{emp}}$ as function of dimensionless delay $\Delta t/(t_D\varepsilon)$. As expected, the plot shows that the error ΔD_{emp} has a minimum. This minimum occurs when $\Delta t \sim 10 t_D\varepsilon$, a value that we used in the remainder of this study.

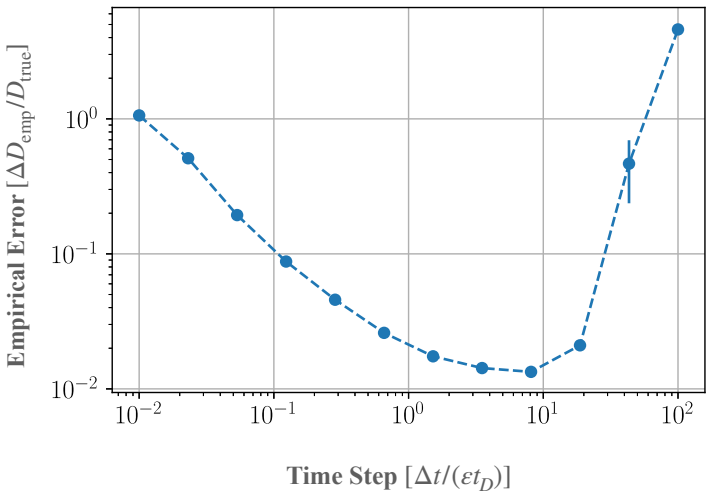

Figure 4.4.3: Optimization of imaging time step Δt. The empirical error ΔD_{emp}, normalised by the true diffusion coefficient D_{true}, is represented as function of relaxation time $\Delta t/\varepsilon$ due to photobleaching associated with imaging, normalized by the diffusive timescale $t_D = \ell^2/D_{\text{true}}/16$. Empirical error was computed as $\Delta D_{\text{emp}} = \sqrt{\frac{n_{\text{ds}}}{n_{\text{ds}}-1}\langle(D_{\text{est}} - D_{\text{true}})^2\rangle}$ from estimated values D_{est} and true value D_{true} of the diffusion coefficient from $n_{\text{ds}} = 200$ number of datasets. Estimated error on the empirical error approximated as the error on the square root of the second moment (Rao, 1973).

4.4.5 Benchmarking of HiFRAP

To test the efficiency of HiFRAP, we compared it to existing methods to obtain diffusion coefficient. Beforehand, we stress the versatility of our method because it makes no assumption on FRAP patterns nor on boundary conditions. This is

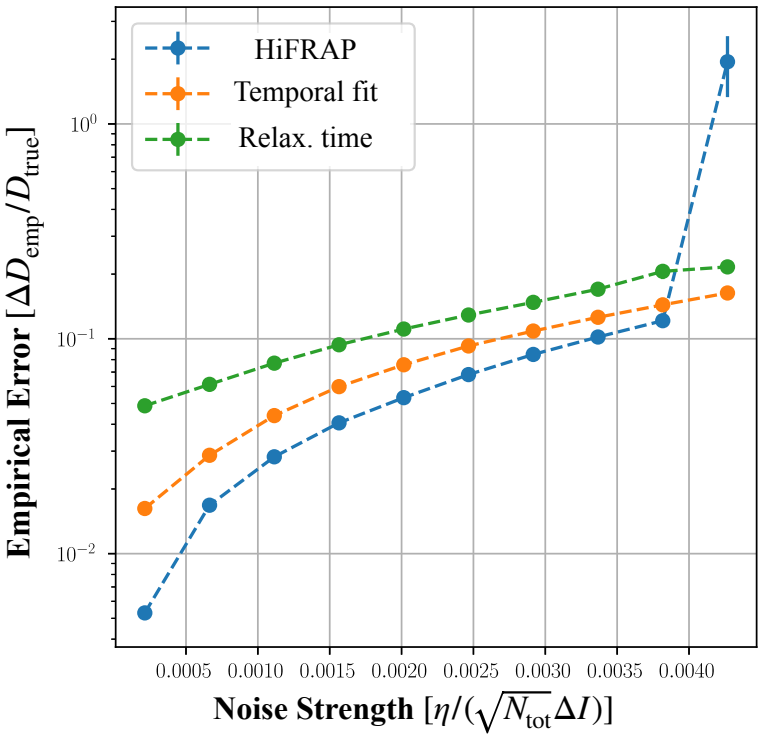

Figure 4.4.4: Benchmarking of HiFRAP. Empirical error ΔD_{emp} as function of the noise strength η, the noise amplitude, normalised in terms of signal drop upon bleaching ΔI and dataset size $N_{\text{tot}} = n_x^2 n_t$ (n_x the number of pixels per axis in the region of interest and n_t the number of images). The lines and relaxation-time-based (green), temporal-fit-based (orange), and HiFRAP (blue) methods. Empirical error was computed as $\Delta D_{\text{emp}} = \sqrt{\frac{n_{\text{ds}}}{n_{\text{ds}}-1}\langle(D_{\text{est}} - D_{\text{true}})^2\rangle}$ from estimated values D_{est} and true value D_{true} of the diffusion coefficient from $n_{\text{ds}} = 200$ number of datasets. Estimated error on the empirical error approximated as the error on the square root of the second moment (Rao, 1973).

illustrated in Figure D.4 (SI), where the region FRAPped is axisymmetric with a Gaussian profile, X-shaped, or E-shaped. Nevertheless, for the comparison with other methods, we had to assume the bleaching pattern to be known, in this case a square bleaching profile.

We have chosen to compare our method with two different approaches, inspired by classical methods in literature (Goehring et al., 2010; Kang et al., 2012). Both are based on spotting the bleaching profile first by fitting the post-bleach frame, and afterwards the diffusion coefficient is estimated by the analysis of the recovery curve, i.e. the spatial average curve inside the bleached region.

In our implantation to model the bleaching profile we used a square FRAPped profile, which accounts for smooth edges due to the PSF effect, as illustrated in (Goehring et al., 2010). From the fitting with post-bleach profile, it is possible to estimate the position of FRAPPed region, the side length, the depth and the smoothness. These parameters are then used to estimated the diffusion coefficient. In second step the two approaches differ. In the first one, referred as relaxation-time based method, the diffusion coefficient is obtained by estimating the half-recovery time of the recovery $\tau_{1/2}$, which is the time at the system recovers half of

the signal.(Kang et al., 2012). The diffusion coefficient is then estimated thanks to an analytic relation with the estimated bleaching size ℓ_{est} and half-recovery time $\tau_{1/2}$ obtained by solving PDE, yielding for a square bleaching $D_{\text{est}} = 0.92\frac{\ell^2}{16\tau_{1/2}}$. In the second approach instead, referred as temporal fit, the diffusion coefficient, it is obtained by fitting directly the recovery curve with its theoretical expression yielded by solving the PDE with the parameters of the FRAPped profile, side length, depth and smoothness previously, obtained. The final formula is found in the Goehring's article (Goehring et al., 2010).

The comparison between empirical errors of diffusion coefficient for the three methods is shown in Figure 4.4.4 for different amplitudes of noise. The errors are computed for 200 FRAP experiments for each noise strength. As could be expected, the discrepancy from estimate to real value increases with the noise strength. HiFRAP, which relies on a spatial-temporal fit, is considerably better than the two others, despite it does not make any assumption on the FRAPped bleaching profile. However, for strong noise for which HiFRAP sometimes fails to estimate the right diffusion coefficient as reported in Section 4.4.3, local minima appear in the cost function spectrum far from the true diffusion value. For this reason, a potential efficient method to minimise the cost function may consist in a two-step minimisation. First, the benchmarking method based on a temporal fit (Goehring et al., 2010) is applied to obtain a good initial diffusion value D_{bench}. Then, the cost function can be minimised by HiFRAP considering as initial bracketing $[D_{\text{bench}}/5, 5D_{\text{bench}}]$. In Appendix D (Figure D.10) I report the distribution of the estimated value with this double minisation procedure, as a function of the noise strength. Contrary to the results in section 4.4.3 where the distribution shows outliers around $D \approx 0$, here the estimated value is more robust.

4.4.6 Generalizing HiFRAP

Our method can be generalized to infer kinetic parameters of more complex dynamics. Besides diffusion, molecules may be synthesised, degraded, or undergo other chemical reactions. In addition, membrane-localised proteins or lipids may be exocytosed or endocytosed. As long as the changes in concentration are not too large, the dynamics of one chemical species can be modelled by a linear diffusion-reaction reaction,

$$\frac{\partial c}{\partial t} = D_{\text{true}}\frac{\partial^2 c}{\partial x^2} + \alpha_{\text{true}} - \beta_{\text{true}}c, \tag{4.4}$$

where α_{true} and β_{true} represent source strength and relaxation rate, respectively, both assumed to be constant. The interpretation of these reaction terms depends on context. For instance, α_{true} may correspond to a synthesis rate and β_{true} to a degradation rate. In the case of a membrane-localised molecule, α_{true} and β_{true} may correspond to the rates of exocytosis and endocytosis, respectively, of this molecule.

To extend HiFRAP to reaction-diffusion, we followed the same approach as in Section 4.4.2 with the difference that the cost to minimize now depends on multiple parameters. We therefore used the Nelder-Mead algorithm (Nelder and Mead, 1965) for multidimensional minimisation (see Section 4.6.5 for details) to minimise the cost function with respect to D and β and/or ε, while for α, the minimum can be computed analytically. This method requires an initial point to

start the minimisation. The choice of this parameter influences the minimisation procedure as is seen in plot D.9 (panel **C**), where for different starting points the minimisation for D and β converges at different values. Therefore, for this method, it is fundamental to set a proper starting point at the correct scale. Moreover, we add range constraints to ensure that the parameters remain within physically meaningful bounds during the minimization process. The parameter values are reported in the captions of Figures 4.4.5 and 4.4.6.

Afterwards, we extended Section 4.4.4 to optimize the imaging time step. Equation (4.4) involves two characteristic times, the diffusion time, $t_D \approx \ell^2/(16D_{\text{true}})$, and the relaxation time $t_\beta = \log(2)/\beta$. The typical recovery time t_r for the combined dynamics is expected to be $1/t_r = 1/t_D + 1/t_\beta$. Accordingly, the optimal time step is $\Delta t = \varepsilon t_r/10$.

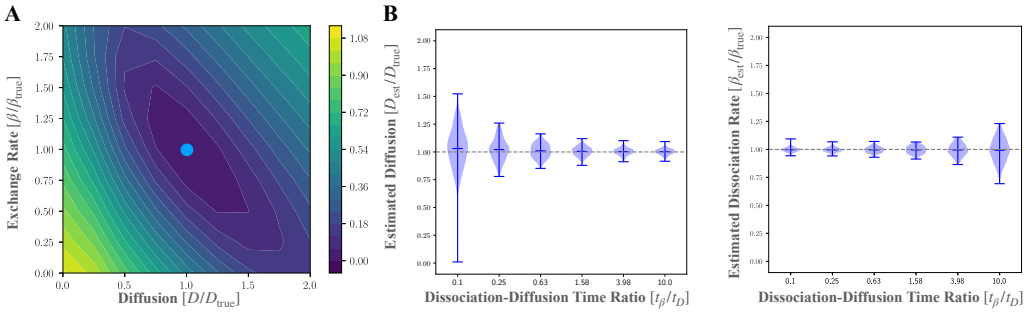

Figure 4.4.5: HiFRAP for estimating diffusion and reaction rates knowing the pre-FRAP concentration field and the rate of photobleaching during imaging. A Contour plot of the cost function ($\log_{10}[C/\eta^2]$, with η the amplitude of the noise) as function of the normalized fitting parameters D/D_{true} and $\beta/\beta_{\text{true}}$, where the cost has first been minimized with respect to the source term α. The colorscale is given on the right, with blue and yellow corresponding to low and high cost, respectively. The light blue point is at the minimum of the cost function; its coordinates give the estimates D_{est} and β_{est}. **B** Estimated dynamical parameters D_{est} and β_{est} as function of the relaxation-to-diffusion time ratio t_β/t_D. Violinplots show the distribution of the estimates and error bars stands for the maximum, the average and the minimum of the distribution. The dashed gray line represents the reference value at which the estimated parameter is equal to the true parameter of the system. Here, the stationary concentration $c_s = \alpha_{\text{true}}\beta_{\text{true}}$ is assumed to be known from the average pre-FRAP concentration field, so that $\alpha_{\text{est}} = c_s\beta_{\text{est}}$. The rate of photobleaching during imaging, ε is supposed to be known from a control area. The number of dataset analysed is 200. As initial starting point for the minimisation, we chose $D_0 = 0.2\ell^2/T$ and $\beta_0 = 1/T$, where ℓ is the FRAPped area side length and T is the total acquisition time. As experimentalists can tune the time step to have the total recovery time $t_\gamma = 1/t_\beta + 1/t_\beta$ at the optimal scale ($t_\gamma \sim 10^{-1}T$), we constrained the diffusion constant and the dissociation rate to be $D < 4L^2/T$ and $\beta < 15/T$ such that $t_\gamma > 10^{-2}T$. Furthermore, the theoretical solution exists only for non-negative values of diffusion, so we set $D \geq 0$, while the dissociation rate $t_\beta > -1/T$ since the negative value can arise when the empirical error $\Delta\beta_{\text{emp}} \sim \beta_{\text{true}}$ which corresponds to a diffusion-dominant system.

Figure 4.4.5 shows the results of our method applied to (4.4). We generated artificial data with the same square FRAP profile, as described in section 4.6.6. As first scenario, we consider the case in which the stationary solution c_s is perfectly known *a priori*. This value may derive from prebleaching images with a sufficient number of pixels. As described in section 4.6.5, if c_s is known, the cost function depends only on two parameters, α and β. In panel **A**, we show an example of this cost function to minimize. The estimate on α may be obtained *a posteriori* from the relation $\alpha_{est} = c_s\beta_{est}$. To explore the efficiency of our method, we would *a priori* need to vary D_{true}, α_{true} and β_{true}. However changing the ratio $\alpha_{true}/\beta_{true}$ only changes the stationary concentration without perturbations and so does not affect the uncertainty of the different estimates Changing the recovery time does not significantly affect the accuracy of the method since we adapt the time resolution of the experiment accordingly. Keeping $\alpha_{true}/\beta_{true}$ and t_r constant, we therefore varied the ratio t_β/t_D in figure 4.4.5. As could be expected (Ciocanel et al., 2024), the uncertainty on the diffusion coefficient becomes high when the fluorophore dynamics is dominated by relaxation and, reciprocally, the uncertainty on the relaxation coefficient becomes high when the dynamics is dominated by diffusion. Finally, we note that, like in the pure diffusion case, the curvature of the cost function yields a good estimate of the error on parameters, see Figure (D.2).

When the values of rate of photobleaching during imaging and stationary concentration are unknown, it is necessary to estimate them together with the kinetic parameters using optimisation in 4-dimensional space. 4.4.6 shows the results of our method in this case. Our estimates remain fairly good. The errors on diffusion and relaxation coefficients behave like in the previous case. The errors on the source strength and intrinsic bleaching rate increase when the fluorophore dynamics is dominated by diffusion, similar to the relaxation rate because all three parameters effectively relate to reactions.

4.4.7 HiFRAP applied to experimental data

We implemented HiFRAP as an ImageJ Macro and we illustrated its function with experiments in fission yeast. We considered a putative mechanosensitive transmembrane protein, Mtl2, which is homogeneously distributed around the cell (Cruz et al., 2013). Details about sample preparation and experimental setup are reported in section 4.6.7. Given that Mtl2 has very low cytoplasmic concentration, we assumed that over the timescale of experiments Mtl2 diffuses along the surface of the cell, and we aimed at testing this assumption and estimating the diffusion coefficient.

We implemented different modelling and experimental options in HiFRAP: diffusion or reaction-diffusion, pre-FRAP profile known or not, photobleaching during determined from a control area or optimised based on a region of interest. To use HiFRAP, it is necessary to select a region of interest (ROI) which includes the bleached area and its surroundings. Here, the ROI should be far enough from cell edges (as viewed from the top) to avoid the effects of cell curvature on signal intensity. It is also important to precisely quantify the photobleaching during imaging and the background intensity. Although this can be done using the inference method (see Section 4.4.6), it is better precise to make these estimates independently from the kinetics of fluorophores. We thus select two control areas, one

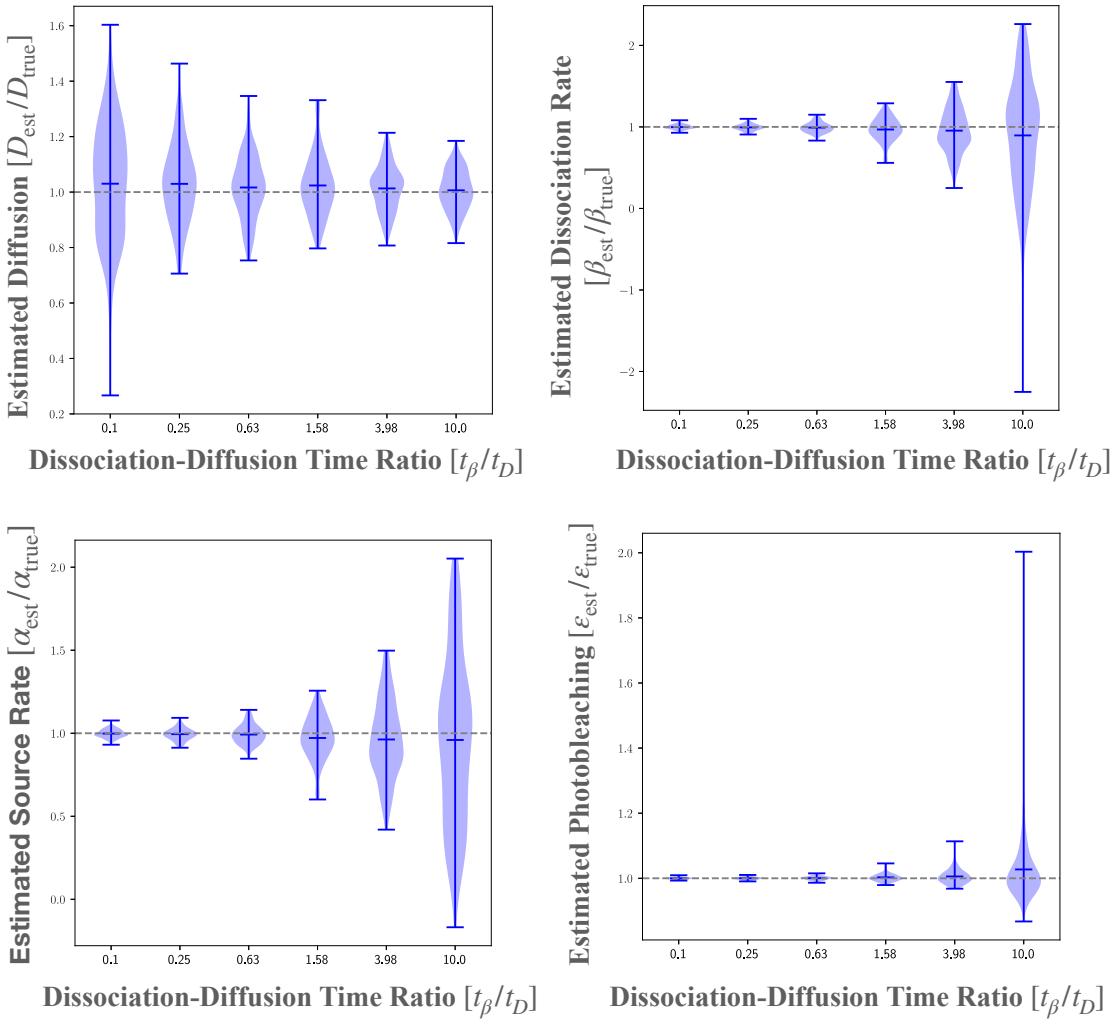

Figure 4.4.6: HiFRAP applied to diffusion-reaction when pre-FRAP concentration field and rate of photobleaching during imaging are unknown. Distribution on for the estimated parameter (normalized by the true values) of 200 datasets simulating reaction diffusion dynamics, as function of the relaxation-to-diffusion time ratio t_β/t_D. Violin plots are for the diffusion coefficient D_{est}, the relaxation rate β_{est}, the source rate α_{est} and the rate of photobleaching during imaging ε. The error bars stand for the maximum, the average and the minimum of the distribution. The dashed gray line represents the reference value at which the estimated parameters is equal to the true value of the system. As an initial starting point for the minimisation, we chose $D_0 = 0.2\ell^2/T$, $\beta_0 = 1/T$ and $\varepsilon_0 = 2/T$ where ℓ is the FRAPped area side-width and T is the total acquisition time. As experimentalists can tune the time step to have the total recovery time $t_\gamma = 1/t_\beta + 1/t_\beta$ at the optimal scale ($t_\gamma \sim 10^{-1}T$), we constrained the diffusion constant and the dissociation rate to be $D < 4L^2/T$ and $\beta < 15/T$ such that $t_\gamma > 10^{-2}T$. Furthermore, the theoretical solution exists only for non-negative values of diffusion, so we set $D \geq 0$, while the dissociation rate $t_\beta > -1/T$ since the negative value can arise when the empirical error $\Delta\beta_{\text{emp}} \sim \beta_{\text{true}}$ which corresponds to a diffusion-dominant system. Moreover, I constrain ε to be in the scale of the temporal window ($1/5/T < \varepsilon < 5/T$), as photobleaching during imaging is visibly detectable by experimentalists through signal fading over time.

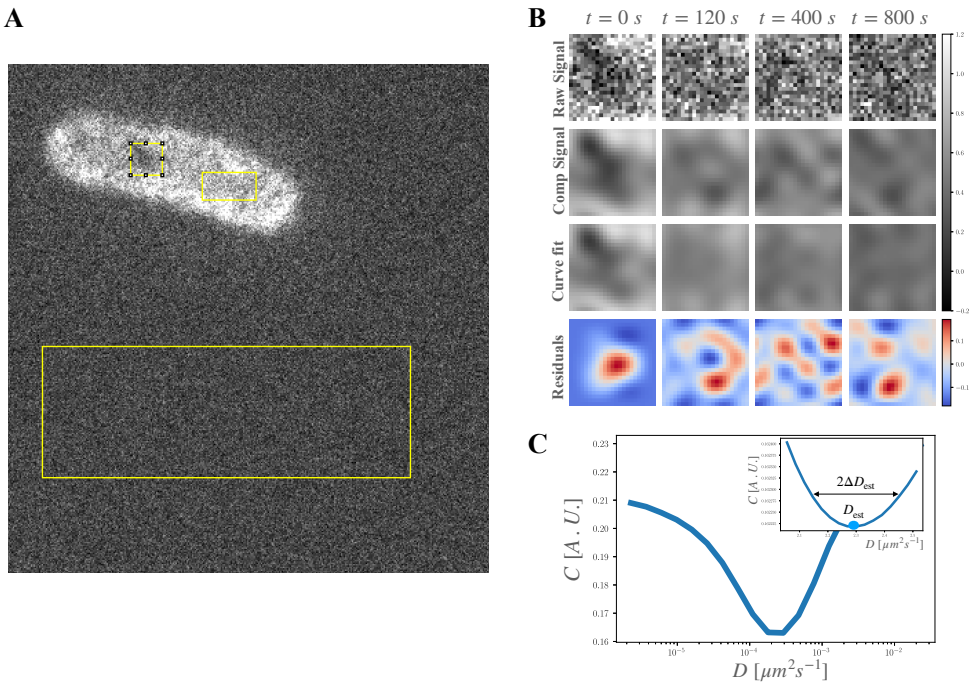

Figure 4.4.7: Inferring the diffusion coefficient from experimental data. **A** Fluorescent microscopy image of a yeast cell expressing Mlt2-GFP. The cell was bleached in a region close to the cell centre. Three regions were selected with FiJi. The square is the region of interest (containing the bleached region) whose side length is $L = 1.23\ \mu m$; the top rectangle is used to estimate intrinsic bleaching associated with imaging, while the bottom rectangle is used to estimate background signal intensity. **B** From experimental signal to fit; 2-dimensional data shown at 4 time points (time is in seconds). From top to bottom: experimental data inside the region (sidelength $L = 1.23\ \mu m$) with FRAP at $t = 0$; compressed experimental data; fit to compressed experimental data; residuals of the fit. The grayscale and colorscale are shown on the right. **C** Corresponding cost function C (in units of the squared signal intensity) as a function of fitting parameter D for the diffusion coefficient; the insert is a zoom-in on the cost's minimum.

free of fluorophores to get background intensity and one containing fluorophores far from the FRAPped region to get the rate of photobleaching during imaging. The background intensity is obtained as the spatiotemporal average of the signal intensity over the first control area. The intrinsic bleaching rate ε is obtained from an exponential least-square fit of the decay of the spatial average of the signal in the second control area. In Figure 4.4.7**A** we show the three regions selected to estimate the diffusion coefficient of Mtl2, where we tried to maximise the areas if selected regions within constraints previously mentioned. Figure 4.4.7**B** show gives an example of signal analysed, its compression, fit, and fit residuals. We estimated the diffusion coefficient and its uncertainty from the minimum and the curvature of the cost function in Figure 4.4.7**C**.

The parameters of the experiments were chosen as follows, based on section 4.4.4. The size of the region of interest (ROI) being limited by cell width; we chose to use square ROIs of side length $\sim 1.5\,\mu m$ and FRAPped square regions of side length $\ell \sim 0.5\,\mu m$. In practice, we found that the FRAP was imper-

fect; the reduction in signal intensity was inhomogeneous and did not occur over a perfect square, see $t = 0$ in Figure 4.4.7B. This may be caused by different factors such as the smallness of the FRAPped region, laser imprecision, or fluctuations in fluorophore concentration. To adjust the imaging time step Δt, we first estimated the order of magnitude of the diffusion coefficient and of photobleaching rate per image by applying HiFRAP to a preliminary experiment. We found $\varepsilon \sim 10^{-2}$ and $D_{\text{est}} \sim 10^4\ \mu m^2 s^{-1}$. Then, to optimize our analysis we chose $\Delta t = 5/8\varepsilon\ell^2/D \sim 10\,s$, and $n_t = 1/\varepsilon \simeq 100$. Finally, to limit computational cost, we set $n_q = 5$ modes for the compression. The initial diffusion value grid, used to determine the initial search interval as explained in section 4.4.2, was set to $D_{\text{grid}} = [0, 10^{-4}, 10^{-3}, 10^{-2}, 10^{-1}, 1, 10, 10^2, 10^3, 10^4]\frac{\ell^2}{T}$, with $\ell \approx 0.5\ \mu m$, $T \approx 700\ s$ the total acquisition time and $\frac{\ell^2}{T} \approx 0.3\ 10^{-4}\ \mu m^2/s$.
We FRAPped once each of 18 cells, see Table D.0.1 and figure D.7 in SI. We found an average value of the diffusion coefficient, $\langle D^{est} \rangle = 2.3\ 10^{-5} \mu m^2 s^{-1}$, lower than diffusion coefficients of proteins in cell membranes (Jacobson et al., 1987), but in agreement with the order of magnitude $10^{-4} - 10^{-2} \mu m^2 s^{-1}$ for membrane-localised proteins in yeast or in fission yeast (Bianchi et al., 2018; Ganguly et al., 2009; Neeli-Venkata et al., 2021; Ries et al., 2008; Valdez-Taubas and Pelham, 2003), likely owing to the presence of a cell wall (Martinière et al., 2012). Overall the purely-diffusive model is validated by the goodness of the fit in almost all cases (the p-value of rejection is smaller than 0.05 only twice out of 18, see Table D.0.1 in SI). The empirical error, or the standard deviation of the diffusion coefficient over all experiments $\Delta D_{\text{emp}} = 2.2\ 10^{-4} \mu m^2 s^{-1}$, is much greater than the estimated error in single experiments $\langle \Delta D_{\text{est}} \rangle = 0.2\, 10^{-4}\ \mu m^2 s^{-1}$. This reflects biological cell-to-cell variability in diffusion, which has already been observed in cultured animal cells based on single particle tracking (Wieser et al., 2009).

4.5 Conclusion

We have developed HiFRAP, a method to infer reaction (or exchange)-diffusion kinetic parameters from FRAP with imperfect conditions, and we have implemented it as a Fiji plugin. HiFRAP uses a whole time-lapse sequence and the variable projection approach to derive kinetic parameters, errors on these parameters, and a test of model validity — for instance whether pure diffusion is a good model for the data.

HiFRAP combines all useful features that have been developed separately in previous work. HiFRAP makes it possible to infer several parameters from a single FRAP experiment (Axelrod et al., 1976; Berkovich et al., 2011; Ciocanel et al., 2017; Cowan and Loew, 2023; Goehring et al., 2010; Kang and Kenworthy, 2008; Kang et al., 2010; Montero Llopis et al., 2012; Röding et al., 2019; Saito et al., 2022; Tolentino et al., 2008; Wu et al., 2008), as long as system dynamics is sufficiently sensitive to these parameters (Ciocanel et al., 2024). We make no assumption on the bleaching profile (Berk et al., 1993; Berkovich et al., 2011; Blumenthal et al., 2015; Elowitz et al., 1999; Jönsson et al., 2008; Röding et al., 2019; Zarabadi and Pawliszyn, 2015); it is thus therefore well-suited to experimental conditions in which it is unfeasible to bleach uniformly the target region. HiFRAP accounts for intrinsic photobleaching associated with repeated imaging,

either based on a control region or on inference of photobleaching rate (Jönsson et al., 2008; Papáček et al., 2013; Röding et al., 2019). Finally, HiFRAP integrates three features that do not seem to have been implemented before: errors on parameter estimation for a single experiment; diffraction in the microscopy setup — though the precise characteristics of the point-spread function are not required as long as its width is larger than pixel size; test of model goodness. We ran HiFRAP against a classical benchmark and found that HiFRAP provides significantly lower errors except for very noisy data.

Nevertheless, HiFRAP has a few limitations. As stated above, it fails for excessive amplitudes of noise, in which case the classical approach is more robust because it assumes the initial bleaching profile to be well-known. A limitation common to HiFRAP and other methods is that the same dynamics (diffusion, or reaction-diffusion) is implicitly assumed to hold outside the observational window. This is not necessarily true, as, for instance, there may exchange of molecules at the boundaries (Taylor et al., 2019). This issue needs to be addressed experimentally, making sure that FRAP is operated well inside into a region with homogeneous dynamics. Most available methods do not explicitly deal with noise. We were led to make the simplifying assumption that noise is homogeneous and stationary, which is not necessarily true (Hillsley et al., 2024; Röding et al., 2019). For example, the amplitude of the shot noise associated with photon counting is proportional to the square root of the signal. Such spatiotemporal variation of noise would likely affect error estimation but not parameter estimation.

In principle HiFRAP can be adapted to FRAP variants, involving for instance continuous photobleaching of a region or photoconversion of a fluorophore (Ishikawa-Ankerhold et al., 2014)), and to the FRAP analysis of other types of dynamics, such as advection by active transport (Ciocanel et al., 2017; Saito et al., 2022), sub-diffusion (Geiger, 2021; Yuste et al., 2014), multiple-species (Ciocanel et al., 2017, 2024; Röding et al., 2019), and non-flat geometries (Bläßle et al., 2018; Klaus, 2016). HiFRAP assumes linearity of underlying partial differential equations (PDEs), but this is not a strong limitations as the dynamics becomes quickly linear upon return of the system to its equilibrium state.

Our method is actually not restricted to FRAP and could be used for inference of parameters for any linear PDE based on the effects of a perturbation on the system. We can therefore expect applicability of our method to capillary isoelectric focusing (Liu et al., 2006) or to optogenetics (Ferenczi et al., 2019). Overall, our approach can be considered as a good alternative to machine learning approaches since it does not require training (Karnakov et al., 2024).

4.6 Theory and methods

4.6.1 Data sampling and compression

We consider a spatiotemporal signal collected at discrete positions $(X^{(1)}, X^{(2)})$ such that $X^{(1)} = X^{(2)} = [0, \Delta x, ..., (n_x - 1)\Delta x]$ and times $T = [0, \Delta t, ..., (n_t - 1)\Delta t]$, where Δx is spatial mesh size and Δt is the time interval between two 2D images, $n_x \times n_x$ is the number of pixels and n_t the number time frames. We arrange the measurements into a unique vector $\{I_k^{DATA}\}_{k=1}^{N_{tot}}$ composed of $N_{tot} = n_x^2 n_t$ elements, where the index $k = a + bn_x + cn_x^2$ is associated to the space-time triplet

$(x_k^{(1)}, x_k^{(2)}, t_k) = (X_a^{(1)}, X_b^{(2)}, T_c)$, $X_a^{(p)}$ and T_c being the a-th component of vectors $X_a^{(p)}$ and T_c, respectively. We assume that this empirical data corresponds to a theoretical spatiotemporal signal $c(x, y, t)$ that can be sampled into a theoretical data vector through the sampling operator $\mathcal{S} : c(x, t) \mapsto \{I_k^{TH}\}_{k=1}^{N_{tot}}$, defined such as $I^{TH}_{a+bn_x+cn_x^2} = c(X_a^{(1)}, X_b^{(2)}, T_c)$.

To save data storage space and computational time, we compress these vectors into smaller made of N elements ($N < N_{tot}$), defining the compression operator $\mathcal{C} : \{I_k^{DATA/TH}\}_{k=1}^{N_{tot}} \mapsto \{Y_i^{DATA/TH}\}_{i=1}^{N}$. In practice, we chose to compress in the space domain because $n_x \times n_x$ is in general much greater than n_t: We keep n_q spatial Fourier coefficient per axis, so that $N = n_q^2 n_t$. Accordingly, we define the compression operator as

$$\mathcal{C} : \quad Y_i^{DATA/TH} = \sum_{k,l=1}^{N} F_{i,k} I_k^{DATA/TH} \delta_{t_i/\Delta t, t_k/\Delta t} \tag{4.5}$$

where $\delta_{i,k}$ is Kronecker's delta and the Fourier matrix $F_{i,j} = \tilde{F}(q_1^{(p)}, x_1^{(p)})\tilde{F}(q_2^{(p)}, x_2^{(p)})$ with

$$\tilde{F}(q_i^{(p)}, x_i^{(p)}) = \frac{1}{\sqrt{N}} \begin{cases} \frac{1}{\sqrt{2}} \cos(q_i^{(p)} x_i^{(p)}) & \text{if } q_i^{(p)} < 0 \\ 1 \quad \text{if } q_i^{(p)} = 0 \\ \frac{1}{\sqrt{2}} \sin(q_i^{(p)} x_i^{(p)}) & \text{if } q_i^{(p)} > 0 \end{cases} \tag{4.6}$$

where the index $i = a + bn_q + cn_q^2$ is associated to the triplet $(q_i^{(1)}, q_i^{(2)}, t_i) = (Q_a^{(1)}, Q_b^{(2)}, T_c)$, where $Q^{(1)} = Q^{(2)} = \frac{\pi \Delta x}{n_x - 1}[-\frac{n_q - 1}{2}, ..., 0, ..., \frac{n_q - 1}{2}]$

Results in Figure D.3 shows that as long as $n_q \geq 3$, compression affects neither the accuracy —how close the mean of the distribution of the estimated parameter is to the true value — nor the precision of the estimation — the variance of the estimated parameter distribution. $n_q \geq 5$ is sufficient to reach 80% of the precision that would be obtained with no compression.

4.6.2 Inferring dynamical parameters

We aim at estimating the vector $\vec{\theta} = \{\theta_1, ..., \theta_n\}$ of the parameters of a linear PDE from an empirical signal $\{Y_i^{DATA}\}_{i=1}^{N}$. We consider system dynamics upon a linear perturbation $w(x)$. The theoretical, noiseless solution to the PDE takes the form

$$Y_i^{TH}\{\vec{\theta}, w\} = \int_{\mathbb{R}^2} \mathcal{G}_i(\vec{\theta}, y) w(y) dy + h_i(\vec{\theta}), \tag{4.7}$$

where the linear operator $\mathcal{G}$ and the shift vector h are specific of the PDE. As we will see later, it is also possible to include in $\mathcal{G}_i$ the effect of any linear operation on the signal, such as spatial filtering by the optical setup.

We consider experimental/technical noise, defined as the residual $e_i = Y_i^{DATA} - Y_i^{TH}(\vec{\theta}_{\text{true}}, w_{\text{true}})$, where θ_{true} and w_{true} are the true parameters and intial condition. We assume that e_i is delta correlated, i.e. $\langle e_i e_j \rangle = \delta_{i,j}\eta^2$, where $\delta_{i,j}$ is the Kronecker delta and η, the unknown noise amplitude. Under these hypotheses, we can estimate the vector $\vec{\theta}$ resorting to the least squares method which consists in minimizing the function $\sum_{i=1}^{N}(Y_i^{DATA} - Y_i^{TH}(\theta, w))^2$ with respect to w and $\vec{\theta}$. Since relation 4.7 for the theoretical signal is linear with respect w, we apply the

variable projection method approach (Golub and Pereyra, 1973) by which we first minimise with respect to w and then with respect to $\vec{\theta}$. Minimising with respect to w yields

$$\min_{w} \sum_{i=1}^{N} [Y^{DATA} - h_i(\theta) - \int_{\mathbb{R}^2} \mathcal{G}_i(\vec{\theta}, y) w(y) dy]^2 = \sum_{i=1}^{N} \sum_{j=1}^{N} [P_{i,j}(\theta)(Y_j^{DATA} - h_j(\vec{\theta}))]^2. \tag{4.8}$$

where P is the orthogonal projector associated with the kernel matrix

$$K_{i,j} = \int_{\mathbb{R}^2} dy \mathcal{G}_i(\vec{\theta}, y) \mathcal{G}_j(\vec{\theta}, y). \tag{4.9}$$

The projector can be estimated using the singular values decomposition (Koyano et al., 2018)

$$P_{i,j}(\vec{\theta}) = \sqrt{\frac{\lambda(\vec{\theta})}{\Sigma_i(\vec{\theta}) + \lambda(\vec{\theta})}} U_{j,i}(\vec{\theta}) \tag{4.10}$$

where $U_{:,i}$ is the matrix containing the i-th eigenvector of the kernel matrix K and Σ_i the associated eigenvalue. In this equation, the prefactor of $U_{i,j}$ acts as low-pass filter applied to the eigenvalues of the kernel matrix K. We preferred this continuous filter over a sharp Heaviside filter in order to obtain a smoother cost function. The true projector is obtained when $\lambda \to 0$. To avoid numerical instability appearing when computing very small quantities, we choose $\lambda = N\Sigma_0\epsilon$, where Σ_0 is the first eigenvalue and ϵ is the machine precision (Press et al., 2007). This yields typical values of $\lambda(\vec{\theta})$ in the range 10^{-11}-10^{-12}, so that the error in computing the cost function is negligible. Moreover, because the average contribution of the noise $\sum_{j=1}^{N}(P_{i,j}(\vec{\theta})e_j)^2 \sim \eta^2 \sum_{j=1}^{N} P_{j,j}(\vec{\theta})$ scales with the trace of the projector, we normalise the sum of residuals in Equation 4.8 by $\sum_{j=0}^{N}(P_{j,j})^2$ to obtain an unbiased estimation on $\vec{\theta}$. We therefore obtain the estimation of the parameter vector as

$$\vec{\theta}_{\text{est}} = \arg\min_{\vec{\theta}} \frac{\sum_{i=0}^{N}[\sum_{j=0}^{N} P_{i,j}(\vec{\theta})(Y_j^{DATA} - f_j(\vec{\theta}))]^2}{\sum_{j=0}^{N}(P_{j,j}(\vec{\theta}))^2}. \tag{4.11}$$

For numerical minimization, we chose Brent's method (a combination of the inverse parabolic interpolation and the golden section search method) for a single parameter and Nelder-Mead simplex method multidimensional minimization for multiple parameters, because these two methods do not require the computation of the gradient. A short description of these methods is reported in table 4.6.1. In practice, we used the scipy built-in function for scalar function scipy.optimize.minimize_scalar(method='bounded') for 1 parameter and minimize(method='Nelder-Mead') for multiparametric minimisation, where for this method an adaptive choice of the simplex parameters depending on the dimensionality of the problem was used (Gao and Han, 2012). However, both methods depend on the initial parameters of the optimisation. For Brent's method, a search interval—defined as the range within which the minimum is sought—must be provided. As described in Section 4.4.2, this choice affects the final estimation. In contrast, for the Nelder-Mead method, an initial value for the kinetic parameters is

necessary to define the vertex of the initial simplex. As discussed in Section 4.4.6, this initial parameter choice influences the final solution. Moreover, to avoid non-physical parameter values, e.g., negative diffusion values, the minimization was constrained within specified boundaries.

The covariance matrix of the estimated parameters can be estimated from the quadratic approximation of the cost function as

$$\langle(\vec{\theta}_{\text{est}} - \langle\vec{\theta}_{\text{est}}\rangle) \otimes (\vec{\theta}_{\text{est}} - \langle\vec{\theta}_{\text{est}}\rangle)\rangle \frac{2}{\sum_{i=0}^{N}(P_{i,i})^2} \mathcal{H}^{-1} C(\vec{\theta}_{\text{est}}), \tag{4.12}$$

where $\mathcal{H}$ is the Hessian of the cost function with respect to $\vec{\theta}$. The Hessian matrix was computed numerically by fitting the cost function with a paraboloid of the form:

$$\mathcal{P}(\theta) = \frac{1}{2}\vec{\theta}^T H \vec{\theta} + \vec{b}_p^T \vec{\theta} + c_p, \tag{4.13}$$

where H is a matrix with $n \times n$ parameters (n is the vector length of $\vec{\theta}$ which contains the kinetic parameters to estimate), $\vec{b}_p$ is a vector of n parameters and c_p is a scalar parameter. For this purpose, the cost function was sampled at multiple points around the minimum. In particular, we evaluate the cost function on linearly spaced arrays with 11 points in the range $[\theta_i^{\text{est}}(1-\Delta\Theta), \theta_i^{\text{est}}(1+\Delta\Theta)]$, with $\Theta = 0.05$ (typical relative error in the parameters) generated for each parameter θ_i, varying only the i-th parameter while keeping $\theta_j = \theta_j^{\text{est}}$ for all $j \neq i$. Furthermore, if $n > 1$ the cost function was sampled along circular paths around the estimated parameters as $\theta_i = (1 + \Delta\Theta\cos\phi)\theta_i^{\text{est}}$, $\theta_j = (1 + \Delta\Theta\sin\phi)\theta_j^{\text{est}}$ and $\theta_k = \theta_k^{\text{est}}$ for all θ_i and θ_j couples and $k \neq i, j$. The angle ϕ linearly spans the range $[0, 2\pi]$ with 21 points. This sampling allows for smoothing the cost function and get information about the second and mixed derivatives. Afterwards, all the coefficients of the paraboloid were obtained by solving the linear least-squares problem. From these coefficients, the Hessian matrix was directly derived as $\mathcal{H}_{ij} = H_{i,j}$.

Finally, if the hypothesis that the model represents well the data is correct, then the residuals approximately correspond to the projection of the noise vector, i.e. $r_i = \sum_j P_{i,j}(\theta_{\text{est}})(Y_j^{DATA} - f_j(\vec{\theta_{\text{est}}})) = \sum_j P_{i,j}(\theta_{\text{est}})(Y_j^{TH}(\vec{\theta}_{\text{true}}) + e_j - f_j(\vec{\theta_{\text{est}}})) \approx \sum_j P_{i,j}(\theta_{\text{est}})e_j$ for $\Sigma_i < \lambda$. Since $\vec{e}$ is uncorrelated noise, $\{r_i\}_{\Sigma_i<\lambda}$ should be normally distributed. Therefore, we can check the hypothesis that the model is compatible with data by applying the Shapiro-Wilk normality (more sensitive) or the Kolmogorov-Smirnov test $\{r_i\}_{\Sigma_i<\lambda}$, the null hypothesis being that residuals are normally distributed. These tests were implemented using the SciPy package, specifically with the functions scipy.stats.shapiro and scipy.stats.kstest. As it can be seen in Figure D.6, we obtain a p_{value} smaller than 0.05 only for 5% of simulations with both tests as expected when artificial data correspond to the model tested.

4.6.3 Modelling signal acquisition

Here we aim at accounting for two experimental features: photobleaching during imaging associated with imaging and diffraction in the optical setup. When the sample is imaged, photobleaching occurs at a rate ε per image. Diffraction implies that the detectors collect the true signal convolved by the point-spread function,

Table 4.6.1: Overview of the optimization method, their description and the number of parameters to minimize

Method	Description	Nr. Par.
Inverse Parabolic Interpolation	This method consists of minimizing the function by iterative quadratic approximation of its local behaviour. It fits a parabola through three points on the function and computes the abscissa where the minimum of the parabola occurs. This is repeated with updated triplets until convergence. It can rapidly find the solution if the function is parabolic near the minimum but may fail if points are nearly collinear or if the interval is not reduced sufficiently.	1
Golden Section Search	This method minimizes the cost function by reducing the search interval at each step. Starting with the initial boundaries, it evaluates the function at two internal points and discards the worst-performing side, keeping the minimum bracketed. To choose the two internal points, the method resorts to the golden ratio rule, for which the ratio between the distance of the two internal points respectively from the two extrema should be equal to $\frac{\sqrt{5}-1}{2} \approx 0.618$. While it is slower, it guarantees convergence even for non-smooth, irregular, or non-parabolic functions, making it useful when other methods fail.	1
Brent's Method	Brent's method combines the robustness of golden section search with the speed of inverse parabolic interpolation. Starting within an initial interval, it uses parabolic interpolation when the function is smooth and switches to golden section search when that step fails. Failures are detected when the new point lies outside the interval, the step size is not reducing sufficiently, or the points are nearly collinear. This makes it effective for both smooth and irregular functions.	1
Nelder-Mead Method	Nelder-Mead is a simplex-based optimization method that iteratively evaluates the cost function on a set of $n+1$ vertices. At each step, the points are updated towards the direction of the minimum by applying reflection, expansion, contraction, or shrinkage operations on the simplex. The parameters of these operations can be efficiently adapted to the dimensionality of the problem (Gao and Han, 2012). In general, Nelder-Mead method is effective when derivatives are not available, but it can be rather slow compared to other method, such as Newton-Gradient.	≥ 2

assumed to be a Gaussian of width μ as a point-spread function. The sampling

operator can then be expressed as

$$\mathcal{S}: \; c(x,t) \to I_k^{TH} = A \exp\left[-\varepsilon \frac{t_k}{\Delta t}\right] \int_{\mathbb{R}^2} d\tilde{x} g(\tilde{x} - x_k, \mu^2) c(\tilde{x}, t_k) + I_\mathrm{b}, \tag{4.14}$$

where the scaling parameter A can be set to 1 if the unit of intensity is arbitrary, the two-dimensional point-spread function is given by

$$g(x, \mu^2) = \frac{1}{\sqrt{2\pi\mu^2}} \exp\left[-\frac{(x^{(1)})^2 + (x^{(2)})^2}{2\mu^2}\right], \tag{4.15}$$

and I_b is the background signal.

4.6.4 Inference in the case of pure diffusion

Here we apply the variable projection method to the signal $\{Y_i^{DATA}\}_{i=1}^N$ in the case of a purely diffusive model. The only kinetic parameter to infer is D, the diffusion coefficient. rate of photobleaching during imaging ε and background signal I_b can be estimated separately from a control area from the sample and from a sample-free area, respectively. The analytical solution of diffusion PDE 4.3 with a generic initial condition $c(y, 0)$ can be expressed as

$$c(x,t) = \int_{\mathbb{R}^2} dy g(x - y, 2Dt) c(y, 0) \tag{4.16}$$

with g defined as in Equation 4.15. If we apply the sampling operator $\mathcal{S}$ to $c(x,t)$ and the compress the resulting vector $\{I_i^{TH}\}_{i=1}^N$, we obtain the theoretical compressed signal as

$$Y_i^{TH} = \sum_{k=0}^{N} \left\{ F_{i,k} \exp(-\varepsilon t_i) \int_{\mathbb{R}^2} dy g(x_k - y, 2Dt_k + 2\mu^2) c(y, 0) + F_{i,k} I_\mathrm{b} \right\} \tag{4.17}$$

By comparison with Equation (4.7), we identify the kernel matrix $\mathcal{G}_i(x,y) = \sum_k \exp(-\varepsilon t_i) g(x_k - y, 2Dt_k + \mu^2)$, and the shift vector $h_i = \sum_k F_{i,k} I_\mathrm{b}$ and $w(y) = c(y, 0)$. In practice, we set the width of the PSF, μ, to Δx. Indeed, we found that the average and the variance of the estimated parameter distribution are not affected by this choice as long as the true value of the system $\mu_\mathrm{true} \gtrsim 1$, see Figure D.5. Eventually, we obtain the kernel matrix from Equation (4.9) as

$$K_{i,j} = \sum_{k,l=0}^{N_{tot}} F_{i,k} F_{j,l} e^{-\varepsilon(t_k + t_l)} g(x_k - y_k, 2D(t_k + t_l) + \mu^2), \tag{4.18}$$

from which it is possible to compute the projector P from Equation (4.10) and minimised the cost function (Equation 4.11) to infer the diffusion coefficient D_est. If the rate of photobleaching during imaging, ε, is not known from a control area, then the cost function should be minimised with respect to both D and ε.

4.6.5 Inference in the case of reaction-diffusion

Now we consider the underlying model to be a linear reaction-diffusion PDE (Equation 4.4). Following the same approach as in the previous section, the theoretical compressed signal takes the form

$$Y_i^{TH} = \sum_{k=1}^{N_{tot}} \{F_{i,k} e^{-\varepsilon t_k} \left(\left(\alpha/\beta - e^{-\beta t_k} \right) + \int_{\mathbb{R}^2} dy \left(g(x_k - y, 2Dt_k + \mu^2)(c(y,0) - \alpha/\beta) \right) + F_{i,k} I_{\mathrm{b}} \} \quad (4.19)$$

By comparison with Equation (4.7), we identify Y_i^{TH} and we obtain the kernel from Equation (4.9)

$$K_{i,j} = \sum_{i,j=1}^{N_{tot}} F_{i,k} F_{j,k} e^{-(\varepsilon+\beta)(t_k+t_l)} g(x_k - x_l, 2D(t_k + t_l) + \mu^2) \quad (4.20)$$

and

$$f_i(\alpha, \beta) = \sum_{k=1}^{N_{tot}} \left\{ F_{i,k} \alpha/\beta (1 - e^{-\beta t_i}) e^{-\varepsilon t_i} + F_{i,k} I_{\mathrm{b}} \right\}. \quad (4.21)$$

We note that $f_i(\alpha, \beta)$ can be defined at $\beta = 0$ by continuity using $\lim_{\beta \to 0}(1 - \exp(-\beta t_i))/\beta = t_i$.

Finally, the cost function defined in Equation (4.11) can be minimised with respect to the kinetic parameters D, α and β. Since α is a linear parameter, the solution that minimise the cost for any fixed D and β, denoted as $\alpha_{\min}$, can be obtained analytically with the projector 4.10 as

$$\alpha_{\min} = \frac{\sum_{i,j,j'}^{N} P_{i,j} \tilde{f}_j P_{i,j'} Y_{j'}^{DATA}}{\sum_{i,j,j'}^{N} P_{i,j} \tilde{f}_j P_{i,j'} \tilde{f}_{j'}} \quad (4.22)$$

where $\tilde{f}_i = \frac{f}{\alpha}$. So, the cost in equation (4.11) is computed directly at $\alpha_{\min}$ and minimise numerically with respect to D and β with the Nelder-Mead's method, yielding the final estimations D_{est}, β_{est} and $\alpha = \alpha_{\min}(D_{\mathrm{est}}, \alpha_{\mathrm{est}})$.

In the simpler case in which the stationary protein concentration $c_{\mathrm{s}} = \alpha_{\mathrm{true}}/\beta_{\mathrm{true}}$ is perfectly known, then the theoretical compressed signal takes the form

$$Y_i^{TH} = \sum_{k,l=1}^{N_{tot}} \left\{ F_{i,k} e^{-\varepsilon t_k} \left(c_{\mathrm{s}} + \int_{\mathbb{R}^2} dy \left(g(x_k - y, 2Dt_k + \mu^2)(c(y,0) - c_{\mathrm{s}}) \right) + \right) + F_{i,k} I_{\mathrm{b}} \right\}. \quad (4.23)$$

The kernel $K_{i,j}$ keeps the same form as in Equation (4.20) and the shift vector becomes $h_i = \sum_{k=1}^{N_{tot}} F_{i,k}(c_{\mathrm{s}} \exp(-\varepsilon t_k) + I_{\mathrm{b}})$ and $w(y) = c(y,0) - c_s$. In this case the cost function (Equation 4.11) should be minimised with respect to D and β only since it is independent on α.

In either of the preceding two cases and in the absence of a control area to estimate photobleaching during imaging, the cost function needs to be minimised with respect to ε (in addition to D, β, and possibly α).

n_x	Number of pixels per axis
n_t	Number of time frames (of 2D images)
Δx	Pixel size
Δt	Time interval between two frames
$c(x,t)$	Concentration field (function of space and time)
I_k^{DATA}	Raw data vector
I_k^{TH}	Noiseless theoretical data vector
Y_i^{DATA}	Preprocessed (compressed) data vector
Y_i^{TH}	Noiseless theoretical preprocessed data vector
$\mathcal{S}$	Sampling operator, maps concentration field onto raw data vector
$\mathcal{C}$	Compression operator, maps raw data vector onto preprocessed vector
F	Spatial Fourier transform matrix
n_q	Number of spatial modes kept per axis after compression

Table 4.6.2: Notations for sampling and preprocessing

$\vec{\theta}$	Vector of kinetic parameters to be inferred
$\vec{\theta}_{\text{true}}$	Vector of true values of kinetic parameters
$\vec{\theta}_{\text{est}}$	Vector of estimated kinetic parameters
w	Spatial perturbation
$\mathcal{G}w + h$	The linear operator $\mathcal{G}$ and the shift vector h
e_i	Noisy part of the preprocessed vector
η	Amplitude of the noise
K	Kernel operator
P	Orthogonal projector matrix associated with kernel operator
U, Σ	Eigenvectors and eigenvalues of the kernel matrix
λ	Threshold on eigenvalues

Table 4.6.3: Notations for inference

4.6.6 Artificial Data

Artificial concentration fields $c(x,t)$ were obtained by solving analytically the reaction-diffusion equation (4.4) (or the diffusion equation 4.3), with known parameters D_{true}, α_{true}, β_{true}, and μ_{true}. The initial condition describes a square FRAPped profile,

$$c(x,y,0) = \begin{cases} c_{\text{s}} - \Delta c & \text{if} \quad |x - \frac{L}{2}| < \frac{\ell}{2} \text{ and } |y - \frac{L}{2}| < \frac{\ell}{2} \\ c_{\text{s}} & \text{else,} \end{cases} \tag{4.24}$$

where $\Delta c/c_{\text{s}}$ is the proportion of bleached fluorophores and ℓ is the square side length. photobleaching during imaging is readily accounted for by multiplying the solution by an exponentially decaying function with rate $\varepsilon_{\text{true}}$. The theoretical data vector takes the form

$$I_k^{DATA} = Ae^{-\varepsilon_{\text{true}} t_k} \left(c_{\text{s}} - \Delta I e^{-\beta_{\text{true}} t_k} \frac{1}{2} \psi(x_k^{(1)}) \psi(x_k^{(2)}) \right), \tag{4.25}$$

I_b	Background signal
μ	Width of point-spread function
ε	Rate of photobleaching during imaging
D	Diffusion coefficient
α	Source rate
β	Loss or exchange rate

Table 4.6.4: Parameters of signal acquisition model and of PDE

with

$$\psi(x_k^{(p)}) = \mathrm{erf}\left(\frac{x_k^{(p)} - \frac{\ell}{2}}{\sqrt{4D_\mathrm{true}t_k + 2\mu_\mathrm{true}x^2}}\right) - \mathrm{erf}\left(\frac{x_k^{(p)} + \frac{\ell}{2}}{\sqrt{4D_\mathrm{true}t_k + 2\mu_\mathrm{true}^2}}\right),$$

where the error function is defined as $\mathrm{erf}(x^{(p)}) = \frac{2}{\sqrt{\pi}}\int_0^{x^{(p)}} e^{-t^2}dt$. The reference concentration c_s is fixed for pure diffusion, whereas for reaction-diffusion, $c_\mathrm{s} = \alpha_\mathrm{true}/\beta_\mathrm{true}$. The same procedure was applied for a Gaussian bleaching profile, X-shape and E-shape (obtained by translation, rotation, extension and superposition of of square bleaching profile)

To obtain a realistic dataset we add noise to the deterministic solution,

$$I_k^{DATA} = I_k^{TH} + \eta\mathcal{N}_k, \tag{4.26}$$

where η is noise amplitude and $\mathcal{N}_k$ is sampled from a Gaussian random variable of mean zero and standard deviation 1. Finally, we compress the simulated vector 4.25 using the compression operator $\mathcal{C}$ (Equation 4.5).

Unless specified otherwise, we used the following default values: $n_x = 121$, $n_t = 16$, $\ell/(n_x\Delta x) = 3$, $\mu_\mathrm{true}/\Delta x = 1$, $\eta/\Delta c = 0.25$, $\varepsilon_\mathrm{true} = 1/(n_t - 1)$, $\Delta c/c_\mathrm{s} = 0.5$, $n_q = 9$, $D_\mathrm{true} = 13.33\frac{\Delta x^2}{\Delta t}$, $\frac{\alpha_\mathrm{true}}{\beta_\mathrm{true}A} = 1$, β_est=0 (for diffusion-only simulations) and $\beta_\mathrm{true}\Delta t = 0.0696$ (for diffusion-exchange simulations) with $\Delta x = 1$, $\Delta t = 1$, $A = 1$ in arbitrary units.

4.6.7 Experiments

The *Schizosaccharomyces pombe* strain *mtl2-GFP: ura4*$^+$ (identifier RN21, (Neeli-Venkata et al., 2021)) was used for experimental validation of the method. Standard fission yeast methods and media were used (Forsburg & Rhind, 2006). The cells were grown in YE5S liquid culture overnight at 25degC, diluted in fresh medium and grown to an optical density (OD_{600}) between 0.4 and 0.6 before live-imaging. Cells were imaged on EMM (minimal media) 2%-agarose pads at room temperature (22-25°C); EMM shows reduced background noise in comparison with YE5S agarose pads. Cells were imaged at their bottom surface, close to the coverslip. Images were acquired with a 100× oil-immersion objective (CFI Plan Apo DM 100×/1.4 NA, Nikon) on an inverted spinning-disk confocal microscope equipped with a motorized stage and an automatic focus (Ti-Eclipse, Nikon, Japan), a Yokogawa CSUX1FW spinning unit, a Prime BSI camera (Teledyne Photometrics,USA) and an iLas2 module (GATACA Systems, France) for FRAP. During FRAP, a 0.4 μ m square ROI was bleached with the 491nm laser

at 20-60 % power and 30 repetitions and the fluorescence recovery was monitored for a time interval ranging from $7 - 10$ s according to the experiment (see table D.0.1).

CHAPTER

FIVE

GENERAL CONCLUSION

5.1 Summary of the results

In this work, I presented a model and an inference methodology designed for the analysis and interpretation of experimental data. Specifically, in chapter 3, I established a theoretical framework to explain Wsc1 clustering in the compressed region of the cell wall. The dynamics of the model is set by reaction-diffusion equations incorporating both mobile and immobile species. The mobile species are characterized by their capacity to diffuse and be recruited from an external source, whereas the immobile species remains static. The model predicts that the introduction of a local activator field, which promotes the transition towards the immobile state, results in an increase in the total concentration within the system. The distribution of this concentration mirrors the profile of the activator field. In the regions where the activator field is more intense, there is a higher total concentration. Conversely, in areas with a weaker activator field, the total concentration remains lower. Additionally, I showed that in the limit in which the timescale of chemical reaction is shorter compared to diffusion and exchange with the reservoir, the two-species dynamics can be reduced into an effective reaction-diffusion equation of one single species, the total concentration. The dynamics in this case is ruled by two parameters, the effective diffusion constant and the effective exchange rate. These parameters decrease as the activator field increases. Indeed, in the more crowded regions the molecules transition more frequently into the immobile state, yielding a reduction of the effective mobility for the whole population.
This model is a good candidate to describe the fission yeast mechanosensor, the Wsc1 protein. In this context, the activator field can be represented by the thinning of the cell wall. Compression of this layer is supposed to enhance the binding affinity between the protein and the cell wall. In this way, proteins could get more frequently trapped and immobile by the surrounding environment. This hypothesis is supported by the potential presence of weaker interactions between the protein and the cell wall polysaccharides, which may become more pronounced in compressed regions due to increased molecular packing in tinier space. The mechanosensitive reaction-diffusion model for Wsc1 is consistent with FRAP experiment outcomes, which show that Wsc1 has a slower dynamics in the compressed regions of the cell wall. However, current data analysis does not distin-

guish between the two mechanisms of protein mobility: lateral diffusion along the cell wall and exchange with the cytoplasm.
To address this issue, chapter 4 introduces a novel inference method, HiFRAP, capable of estimating all diffusion-reaction parameters from a single time-lapse from FRAP experiment. For Wsc1 proteins, HiFRAP could quantify recovery due to cytoplasmic exchange rate with the cytoplasm and diffusion constant along the cell wall. Compared to existing methods, HiFRAP offers greater versatility. It does not rely on the initial shape of the bleaching, making it applicable in cases where the bleaching shape is unknown. This is particularly relevant for small cells, such as fission yeast, where protein fluctuations and optical limitations complicate precise control over bleaching shape. Additionally, HiFRAP addresses experimental artifacts, such the point spread function and intrinsic photobleaching, In Wsc1 dynamics, this effect is particularly relevant, since the signal is almost completely loss after only 20 frames.
Furthermore, HiFRAP provides error in the estimation of the parameters. This feature could help assess the validity of the reaction-diffusion model and discern whether variability among individuals is due to biological differences or experimental noise.

Beyond the application to Wsc1 protein, the binding sensitive reaction-diffusion model and HiFRAP can be utilized to gain quantitative insights into molecular dynamics within cells, revealing interactions between cellular components that are affected by external stimuli.

5.2 Perspectives

In this section, I discuss feasible developments of my work and possible issues that could drive future research.

5.2.1 Application of HiFRAP to Wsc1

Although an inference method has been developed, its application to the experimental data for Wsc1 has not yet been performed. Before proceeding with its use, several key issues must be addressed.
First, the HiFRAP method is only applicable if data are collected for at least three Fourier modes per axis. This requirement imposes a significant limitation: if data are collected on only one cross-sectional plane and a two-dimensional model is desired, the application of HiFRAP is not feasible. To overcome this limitation, two potential solutions can be considered.
One solution involves capturing a top-down view of the cell tip, rather than a cross-sectional view, during FRAP imaging (Dodgson et al., 2013). However, integrating cell wall thinning measurements with such a field of view would only be possible using a 3D scanning with a confocal microscope, which might slow down the process of image acquisition.

An alternative, and perhaps simpler, approach is to consider a quasi-one-dimensional dynamical system. If one dimension of the bleaching region is significantly larger than the other, it is possible to reduce the complexity of the

model by focusing on one-dimensional dynamics. In this case, HiFRAP can be implemented directly in a one-dimensional framework, providing the necessary results without the complexities of a two-dimensional analysis.

Furthermore, if more realistic models for Wsc1 dynamics are developed, for example taking care of the real curved dome shaped of the organism or heterogenous exoytosis process, this may be easily incorporated in the FRAP inference method as long as PDE remains linear. In this case, it would be sufficient to adapt the Green's function and the shift term computed in section 4.6.2.

5.2.2 Comparative studies with other mechanosensors

A comparative analysis of mechanosensors, particularly Wsc1 and other similar proteins, presents a valuable opportunity to enhance our understanding of how different protein structures contribute to mechanosensitive clustering dynamics. For example, researchers in Minc's Lab are currently cloning other fungal mechanosensors, such as Wsc2, Wsc3, and Wsc4 from *S. cerevisiae* into *S. pombe*. All of these proteins possess a cysteine-rich domain, a key structural feature that may facilitate interaction with the polysaccharides of the cell wall. In contrast, Mtl2, another mechanosensor in fission yeast, lacks this cysteine-rich domain. By comparing mobility parameters, such as the diffusion constant and cytoplasmic exchange rates, between these proteins at different cell wall thinning, will gain insights into the contribution of specific structural components. In particular, we would like to understand not only if cystein-riched domain is so essential for clustering but also how it is related to the mobility of the proteins.

5.2.3 Faster optimisation algorithms

In Chapter 4, I discussed one of the main limitations of our algorithm: its execution speed. The bottleneck arises primarily due to the use of singular value decomposition for evaluating the cost function, which can become very slow or even infeasible for large matrices encountered in the study of two-dimensional systems. This issue is further accentuated in three-dimensional systems, where the matrix size increases significantly. To address this challenge, we resorted to data compression transformations. So instead of working with the entire data set information, I keep just few modes, that are generally less noisy and contains most of the signal. This approach has proven to be relatively efficient, yielding good results in terms of accuracy and precision. However, even with these optimizations, the computation time remains in the order of minutes. So to further improve the speed, another possible approach is defining effective initial parameters x as a solution to a linear system. Indeed, the minimization 4.8 may be rewritten $||\vec{Y}^{DATA} - M\vec{v}_{est}||^2$, where $\vec{v}_{\text{est}}$ solves the problem $M\vec{v}_{\text{est}} = \vec{Y}^{TH}$, with $M = K + \lambda\mathbb{1}$, where K is the kernel 4.9, λ the penalty parameter and $\mathbb{1}$ is the identity matrix. The solution of this problem may be found with efficient algorithms, such as the prescribed conjugate gradient method (Baxter, 2002), which may exploit the property of the matrix M, which for example shift invariant in space.
This technique may hopefully reduce the computation time to the order of seconds,

enabling the processing of larger datasets and maybe a faster real-time analysis.

5.2.4 More robust inference method

As we remarked in chapter 4.4.5, the inference method fails for too strong noise amplitudes or if the number of parameters to infer is too high. This issue is less present in other methods, as inference is performed with more a priori information, such as the initial shape of the bleaching. So, one strategy to overcome this problem may be to add additional constraints to restrict the space of solutions and facilitate optimization.
For example, a feasible hypothesis would be considering the fact that the FRAP bleaching process cannot increase the intensity of fluorescent molecules. This means that the stationary concentration minus the initial profile, $c_s - w$, must be positive. So, it is possible to consider algorithms that consider the desired solution of a linear problem with nonnegative constraints (Vogel, 2002).
Another hypothesis to facilitate the algorithm would be to assume a restricted space for bleaching. Even if our approach is more general as I make any hypothesis on the fact that the area that I analyze contains all the bleached molecules, this situation is easily in reach in experimental condition. One way to consider this assumption would be to integrate the kernel in equation 4.9 into a smaller space (Albert and Rath, 2020).
Another improvement would be given by a better noise modeling. Indeed, linear least-squares estimation in 4.11 is unbiased, even in the presence of non-homogeneous noise, but it achieves minimal sampling variance compared to other estimators only if the errors on each data point have the same amplitude. Since, the amplitude noise in FRAP can be considered as the sum of two contributions, a uniform background noise, a_{BG} plus square root of signal dependent $b_I\sqrt{I_i}$, linear least square estimator is not the estimator with the lowest sampling error and alternatives should be considered. To tackle this problem, it would be possible to write a proper weighted contribution data point, $Y_i^{DATA} = I_i^{DATA}$ (for simplicity I omit the effect of compression), in the cost function as $\sum_i W_i (Y_i^{DATA} - Y_i^{TH})^2$, with $W_i = \frac{1}{a_{\mathrm{BG}} + b_I Y_i^{TH}}$ (Röding et al., 2019). The factor a_{BG} may be estimated from a priori calibration, looking to how the signal varies with intensities for a homogeneous stationary concentration. However, since Y^{TH} at the denominator contains the initial profile parameters w , the minimization problem 4.8 is non-linear and the variable projection method cannot be applied. To remedy such a difficulty, one may solve the non linear problem by iteration (Shen et al., 2011). Starting with a weighting vector $W_i \approx \frac{1}{a_{\mathrm{BG}} + b_I Y_i^{DATA}}$, a first estimate of the dynamical vector can be performed by cost function minimization 4.11. Once the first solution $Y^{TH}(\theta^{(1)_{\mathrm{est}}})$ is computed, the weighting vector can be updated, and a new optimization will yield $\theta_{est}^{(2)}$. We can continue this process until the value of θ_{est} converges.

5.2.5 Closing reflections

Cells exhibit an incredibly dynamic organization, where molecular crowding, membrane-bound compartments, and cytoskeleton elements create a highly complex and non-equilibrium system. These conditions often give rise to emergent behaviors, such

as collective dynamics and novel modes of molecular transport. Such behaviors are not easily captured by classical models, e.g. diffusion-reaction, making this a rich area for further investigation.
Advances in experimental techniques now allow us to track these intricate processes in unprecedented detail. However, the amount of volume and complexity of the data generated present significant challenges for interpretation. Moreover, the experimental devices come with numerous settings, whose variations could affect the results. Therefore, developing new theoretical models is fundamental to provide new lenses to observe phenomena and make comparisons between experiments obtained with different experimental conditions. This study may enable us to uncover more in-depth insights into the fundamental principles governing intricate motion of molecules inside the cell.

APPENDIX

A

HETEROGENEOUS EXOCYTOSIS

In this Appendix, I would like to generalize the model in chapter 3, when the incoming flux is heterogeneous. This heterogeneity can be due to the directed motion of the vesicles. I define $a(x) : x \to a(x)$ the local source rate coming from the cytoplasm for a given position of the cell wall x. In this way, I can rewrite equations 3.3

$$\begin{cases} \frac{\partial c_\mathrm{u}}{\partial t} = D\frac{\partial^2}{\partial x^2}c_\mathrm{u} - k_\mathrm{on}(x)c_\mathrm{u} + k_\mathrm{off}c_\mathrm{b} + a(x) - \beta c_u \\ \frac{\partial c_\mathrm{b}}{\partial t} = k_\mathrm{on}(x)c_\mathrm{u} - k_\mathrm{off}c_\mathrm{b} \end{cases} \tag{A.1}$$

where for sake of simplicity I include the cell wall thinning dependence in $k_\mathrm{on}(x)$. To look for stationary solution, I impose that

$$\begin{cases} 0 = D\frac{\partial^2}{\partial x^2}c^*_\mathrm{u} - k_\mathrm{on}(x)c^*_\mathrm{u} + k_\mathrm{off}c_\mathrm{b} + a(x) - \beta c^*_u \\ 0 = k_\mathrm{on}(x)c^*_\mathrm{u} - k_\mathrm{off}c^*_\mathrm{b} \end{cases} \tag{A.2}$$

The solution of the second equation is straightforward and gives

$$c^*_b = \frac{k_\mathrm{on}}{k_\mathrm{off}}c^*_u \tag{A.3}$$

Substituting this result in the first equation, it yields

$$0 = \frac{\partial^2}{\partial x^2}c^*_\mathrm{u} + a(x) - \beta c^*_u \tag{A.4}$$

To solve this equation, I can resort to Fourier transform. For a generic spatial function $f(x)$, we can express its Fourier components (denoted with the hat) as $\hat{f} = \frac{1}{2\pi}\int dx e^{-iqx}f(x)$. In this new space, equation A.2 gets simpler

$$0 = -q^2\hat{c}_\mathrm{u}(q) + \hat{a}(q) - \beta\hat{c}_u(q) \tag{A.5}$$

yielding $\hat{c}_\mathrm{u}(q) = \frac{\hat{a}(q)}{Dq^2+\beta}$. Getting back to real space, I arrive at the final solution

$$c^*_\mathrm{u} = \alpha\int_{-\infty}^{\infty} dq e^{iqx}\frac{\hat{a}(q)}{Dq^2+\beta} \tag{A.6}$$

In the case of homogeneous source rate α, $\hat{a} = \alpha\delta(q)$, where $\delta(q)$ is the Dirac delta. It is worthy to remark that only in the homogeneous case the diffusion flux

is zero, since $\partial_x c_{\mathrm{u}}^* = 0$. Conversely, in the heterogeneous case the diffusion flux is not zero, hence the system is never at equilibrium. However, the stationary state is reached when the contribution due to the exchange rate compensates for the diffusion fluxes.
If we look at the total concentration, here again it is possible to define the concentration enrichment as $\frac{c_{tot}^*(x)}{c_0(x)}$, where in this case the concentration when no compression is applied depends on the space position as

$$c_0(x) = \int_{-\infty}^{\infty} dq e^{iqx} \frac{\hat{a}(q)}{Dq^2 + \beta}(1 + \frac{k_{on}^0}{k_{off}}) \tag{A.7}$$

It yields the same final result as before

$$\frac{c_{tot}^*}{c_0(x)} = 1 + \kappa_{\mathrm{r}} h_{\mathrm{r}} \tag{A.8}$$

So the clustering behavior is maintained.

APPENDIX

B

FOURIER SOLUTION TO REACTION-DIFFUSION EQUATIONS

In this Appendix, my objective is to provide a solution to PDE 3.3 in the Fourier space. To simplify the calculation, I assume that the relative thinning is homogeneous. In this simple case, k_{on}, i.e. the activation rate, does not depend on x anymore and it is fixed by the compression value which is now constant in space. In this situation, if the domain of interest sufficiently big, I can rewrite the concentration as

$$c_{\mathrm{u/b}}(x) = \int_{-\infty}^{\infty} e^{iqx} \hat{c}_{\mathrm{u/b}}(q) dq \tag{B.1}$$

where $\hat{c}_{\mathrm{U/B}}(q)$ is the Fourier transform. In the Fourier space 3.3 gets

$$\frac{\partial}{\partial t} \begin{pmatrix} \hat{c}_{\mathrm{u}} \\ \hat{c}_{\mathrm{b}} \end{pmatrix} = \begin{pmatrix} -k_{on} - Dq^2 - \beta & k_{off} \\ +k_{on} & -k_{off} \end{pmatrix} \begin{pmatrix} \hat{c}_{\mathrm{u}} \\ \hat{c}_{\mathrm{b}} \end{pmatrix} + \begin{pmatrix} \alpha\delta(q) \\ 0 \end{pmatrix} \tag{B.2}$$

The solution of this equation have two contributions $A_1 \sim e^{\lambda_+ t}$ and $A_2 \sim e^{\lambda_- t}$, where $\lambda_{+/-}$ are eigenvalues of the previous matrix, which have the form

$$\begin{cases} \lambda_+ = \frac{1}{2}(\sqrt{(k_{\mathrm{tot}} + Dq^2 + \beta)^2 - 4(Dq^2 + \beta)k_{\mathrm{off}}} - (k_{\mathrm{tot}} + Dq^2 + \beta) \\ \lambda_- = -\frac{1}{2}(\sqrt{(k_{\mathrm{tot}} + (Dq^2 + \beta))^2 - 4(Dq^2 + \beta)k_{\mathrm{off}}} - (k_{\mathrm{tot}} + Dq^2 + \beta) \end{cases} \tag{B.3}$$

with $k_{\mathrm{tot}} = k_{\mathrm{on}} + k_{\mathrm{off}}$.
Now it is interesting to consider the limit in which $\theta = \frac{Dq^2+\beta}{k_{off}} << 1$. In this case in the zero-order approximation the eigenvalues gets

$$\begin{cases} \lambda_+ = -\frac{k_{off}}{k_{on}+k_{off}}(Dq^2 + \beta) + O(\theta^2) \\ \lambda_- = -k_{tot} + O(\theta) \end{cases} \tag{B.4}$$

The two modes λ_- and λ_+ relaxes back to equilibrium for different timescales. Indeed, λ_-, which represents the chemical reaction, is much faster, while λ_+, which represents the diffusion-exchange dynamics is slower. So first the chemical reaction reaches the equilibrium, without the effect of diffusion, then, the system evolves according to diffusion and exchange with the cytoplasm. On the other hand if $\theta = \frac{Dq^2+\beta}{k_{off}} >> 1$, the eigenvalues are

$$\begin{cases} \lambda_+ = -k_{off} + O(\theta^{-2}) \\ \lambda_- = -(Dq^2 + \beta) + O(\theta^{-1}) \end{cases} \tag{B.5}$$

So in this case, I have λ_- which is the fast mode representing the diffusion-exchange dynamics. Hence, in this approximation, the system achieves the diffusion-exchange equilibrium first and then at a different time scale, the chemical-reaction one.

APPENDIX

C

WEAK PROTEIN-PROTEIN INTERACTION

In this appendix, I study protein clustering dynamics in the context of reaction-diffusion equations with protein-protein interaction. More specifically, I suppose that the compression of the cell wall affects the protein conformation and favor protein-protein binding, as suggested by Kock (Kock et al., 2015). For notation simplicity, I suppose that the weak interactions with the cell wall do not contribute into getting the protein in the immobile state. The presence of both phenomena can be studied in future works.
In this case, the chemical reaction introduced in chapter 3 assumes the following form

$$\mathrm{U} + \mathrm{U} \underset{\gamma_{\mathrm{off}}}{\overset{\gamma_{\mathrm{on}}}{\rightleftharpoons}} \mathrm{B} \tag{C.1}$$

In this scenario two proteins can form a bound with an association rate γ_{on} and dissociation rate γ_{off}. The generalization of this interaction modelling to more complex links, such as multimer weak bounds, is straightforward and it is not proved here.
Supposing that the presence of a stress or compression on the cell wall affects the protein structure and favors the binding rate with a linear relation, γ_{on} can be expressed as

$$\gamma_{\mathrm{on}} = \gamma^0_{\mathrm{on}} + \bar{\gamma}_{\mathrm{on}} h_{\mathrm{r}}(x) \tag{C.2}$$

with $\gamma_0 \geq 0$, the association rate when no stress is applied and $\bar{\gamma}_{\mathrm{on}} > 0$ the binding increase a relative thinning equal to 1. With this assumption, the corresponding PDE gets

$$\begin{cases} \frac{\partial c_{\mathrm{u}}}{\partial t} = D\frac{\partial^2}{\partial x^2} c_{\mathrm{u}} - (\gamma^0_{\mathrm{on}} + \gamma h_{\mathrm{r}}(x)) c_{\mathrm{u}}^2 + \gamma_{\mathrm{off}} c_{\mathrm{b}} + \alpha - \beta c_{\mathrm{u}} \\ \frac{\partial c_{\mathrm{b}}^2}{\partial t} = (\gamma^0_{\mathrm{on}} + \gamma h_{\mathrm{r}}(x)) c_{\mathrm{u}}^2 - \gamma_{\mathrm{off}} c_{\mathrm{b}} \end{cases} \tag{C.3}$$

The main difference with PDE 3.3 is that PDE *C.3* is non-linear due to a quadratic term in c_{u}. Using the same procedure as chapter 3, it is easy to show that at the stationary state

$$\begin{cases} c^*_{\mathrm{u}} = \frac{\alpha}{\beta} \\ c^*_{\mathrm{b}} = \left(\frac{\alpha}{\beta}\right)^2 \frac{\gamma^0_{\mathrm{on}} + \bar{\gamma}_{\mathrm{on}} h_{\mathrm{r}}}{\gamma_{\mathrm{off}}} \end{cases} \tag{C.4}$$

So total the concentration ratio with the stress-free state is

$$\frac{c^*_{\text{tot}}}{c_0}(x) = (1 + \gamma_r h_r(x)) \tag{C.5}$$

where $\gamma_r = \frac{\bar{\gamma}_{\text{on}}}{\gamma^0_{\text{on}} + \gamma_{\text{off}}} \geq 0$. So, in correspondence to the compressed region of the cell wall, the protein concentration increases.

APPENDIX

D

SUPPLEMENTARY FIGURES

In this Appendix, it is reported the supplementary figures of article draft discussed in chapter 4.

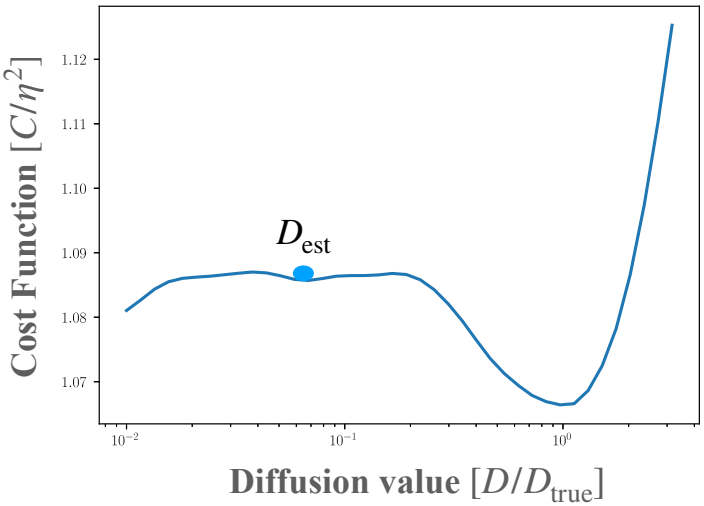

Figure D.1: Example of a jagged cost function with multiple local minima obtained for a large value of noise, $\frac{\eta}{\Delta I\sqrt{N_{tot}}} = 0.008264$, where η is the typical noise amplitude, ΔI the drop in signal upon FRAP and N_{tot} the total number of points. The estimated value, D_{est}, is incorrect, since the algorithm stops in a local minimum which is not the global minimum.

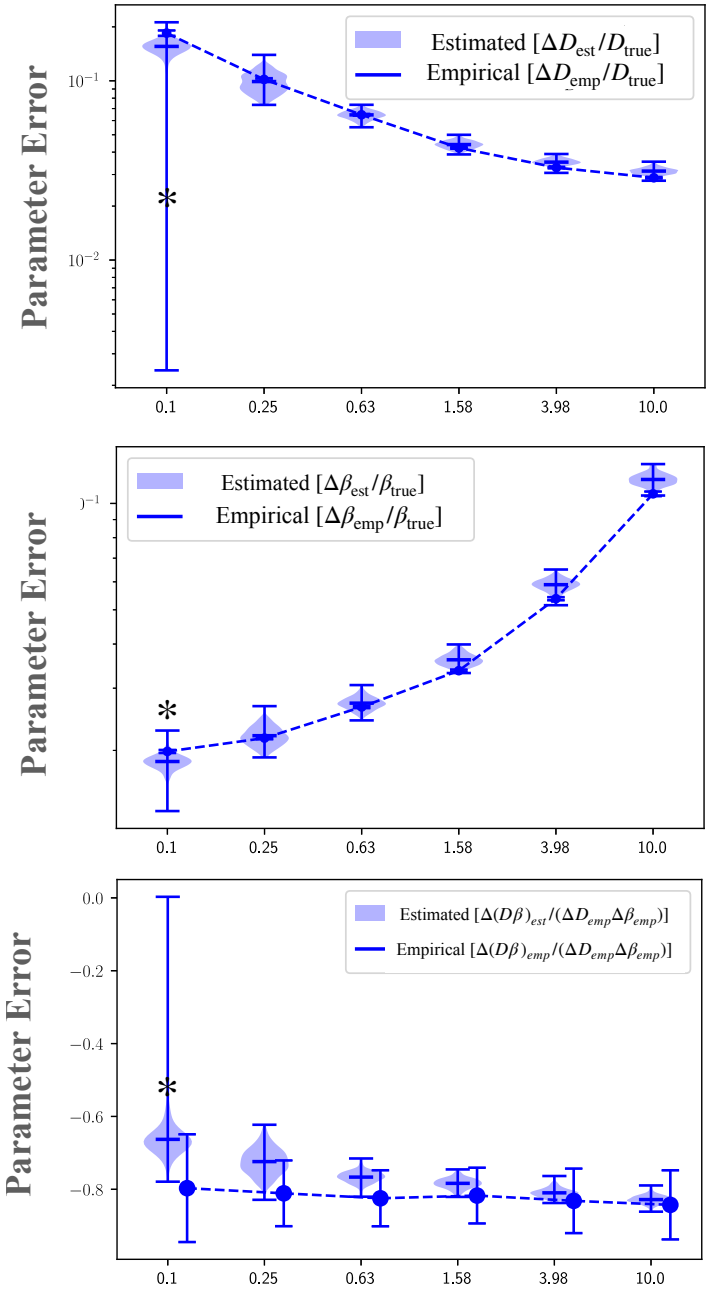

Figure D.2: Comparison between empirical error (measured over all realisation of noise) and estimated error (measured from single realisations) when inferring diffusion coefficient D and exchange coefficient β. From top to bottom: error on D, error on β, and correlation between D and β. Where an asterisk is present, the computation of the error was not possible for 1 out of 200 datasets

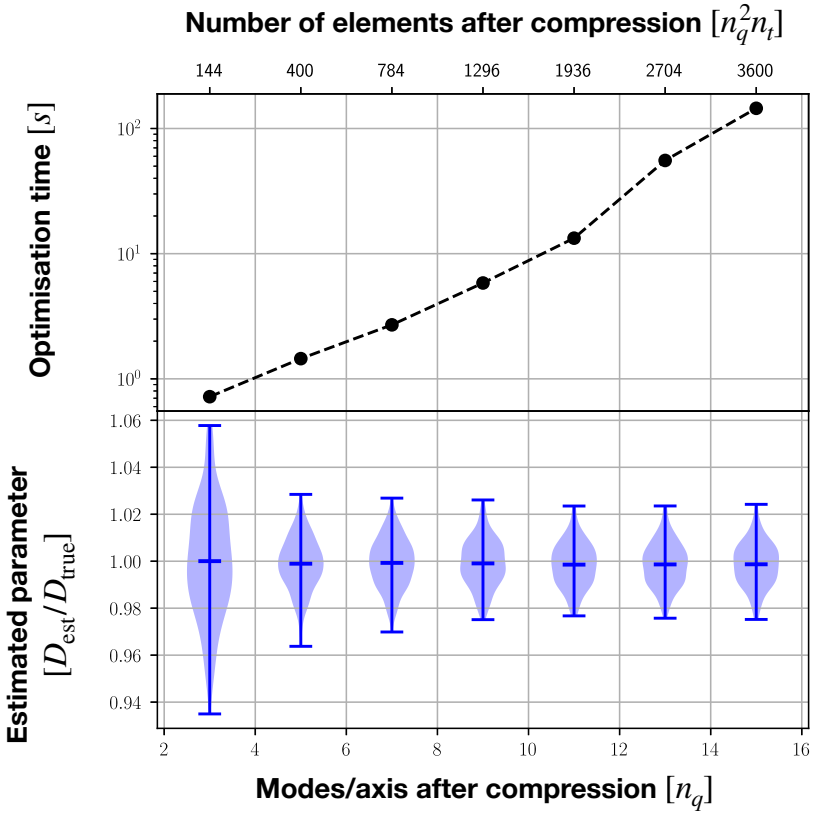

Figure D.3: Effect of compression. Panel on the top: time necessary to minimise numerically the cost function $C(D)$ as in figure 4.4.1 (panel B), with D the diffusion value, as a function of the number of elements kept after compression $N = n_q^2 n_t$, with n_q the number of modes per axis. Results are obtained only from one execution. Panel on the bottom: violin plot for 200 simulations which shows the estimated parameter distribution D_{est} (normalised with the true value D_{true}) as function of the number of modes kept per axis after compression, n_q

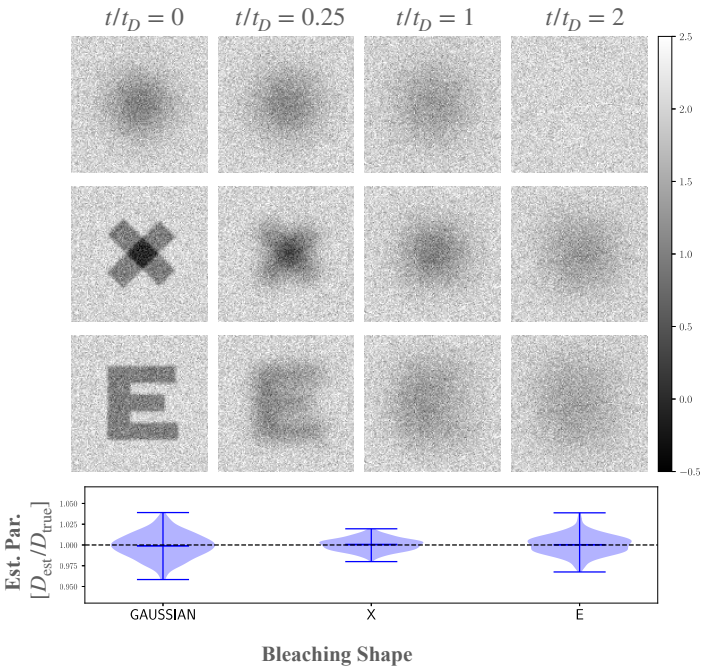

Figure D.4: Panel A: Simulation of different diffusive dynamics with different bleaching shapes. The results are shown at different time (normalised by $t_D = \frac{(L/3)^2}{16D}$, where L is the observation window size). The colorbar represents the intensity signal value normalised with respect to the typical signal drop-off ΔI. Pannel B: Violinplot of the estimated parameter distribution D_{est} (normalised with the true value D_{true})for different bleaching shape. The dashed gray line represents the reference value $D_{\text{est}}/D_{\text{true}} = 1$.

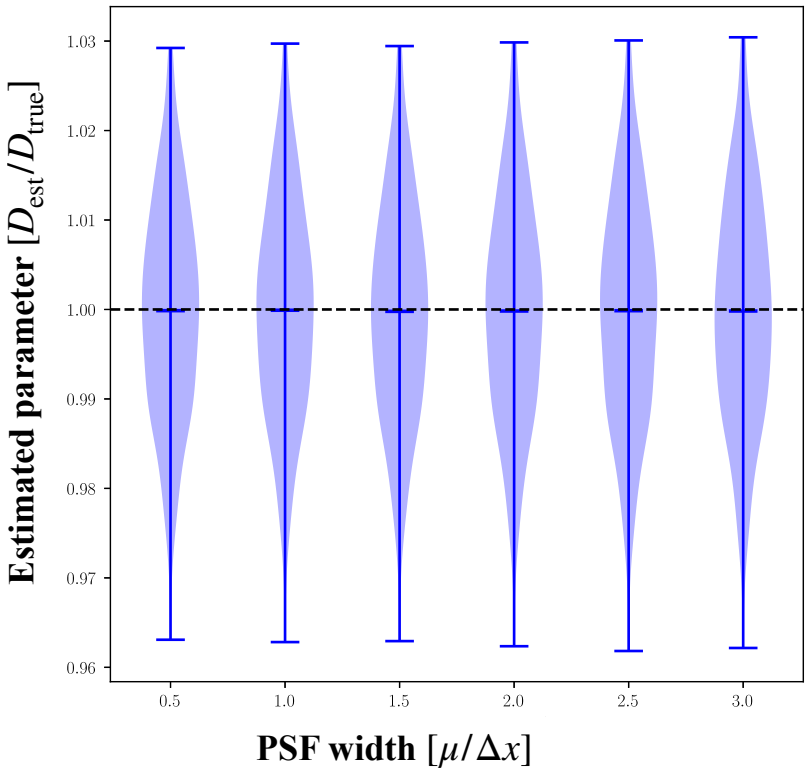

Figure D.5: Independence on the point-spread-function width: violinplot of the estimated parameter distribution D_{est} (normalised with the true value D_{true}) for different Point-Spread-Function width μ (normalised with the pixel size Δx). The dashed gray line represents the reference value $D_{\text{est}}/D_{\text{true}} = 1$.

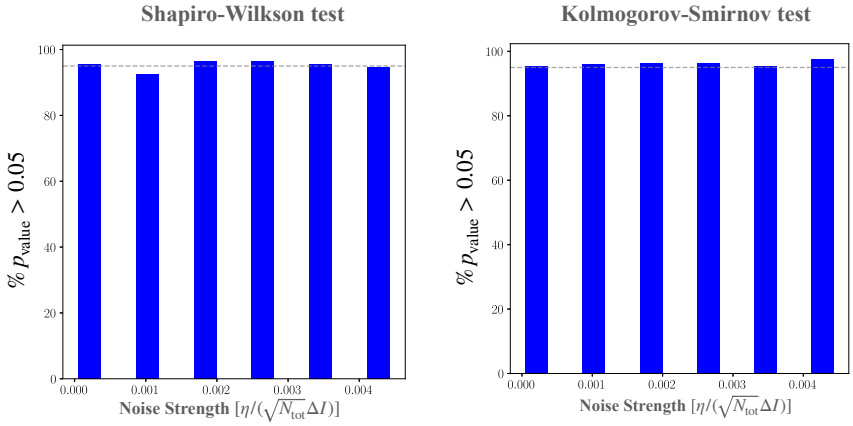

Figure D.6: Shapiro and Kolmogorov test: the bar represents the percentage of times we obtain a Shapiro or Kolmogorov p-value greater than 0.05 after fitting data with the estimated diffusion value

Experiment	$\Delta t[s]$	D_{est} $[\mu m^2/s]$	ΔD_{est} $[\mu m^2/s]$	SW p-value	KS p-value	ε
1	8	0.92×10^{-4}	3.33×10^{-6}	0.14	0.10	0.00774
2	8	2.28×10^{-4}	1.55×10^{-5}	0.7809	0.820	0.0068
3	8	1.41×10^{-4}	1.14×10^{-5}	0.36	0.88	0.00549
4	8	8.01×10^{-4}	1.09×10^{-4}	0.13	0.30	0.00619
5	8	1.02×10^{-4}	5.57×10^{-6}	0.26	0.72	0.0059
6	8	4.69×10^{-5}	3.62×10^{-6}	0.13	0.94	0.00593
7	8	1.30×10^{-4}	5.90×10^{-6}	0.79	0.14	0.00568
8	8	1.19×10^{-4}	7.85×10^{-6}	0.0061	0.4817	0.00659
9	8	3.05×10^{-4}	1.78×10^{-5}	0.525	0.90	0.005122
10	10	1.25×10^{-4}	9.55×10^{-5}	0.087	0.157	0.005106
11	10	4.40×10^{-4}	3.18×10^{-5}	0.19	0.19	0.00606
12	10	4.49×10^{-4}	3.18×10^{-5}	0.18	0.18	0.00602
13	10	3.94×10^{-4}	2.89×10^{-5}	0.0074	0.40	0.00372
14	10	1.08×10^{-4}	1.16×10^{-5}	0.88	0.99	0.003842
15	7	1.79×10^{-4}	0.91×10^{-5}	0.24	0.31	0.0025
16	7	2.87×10^{-4}	1.41×10^{-5}	0.212	0.99	0.003588
17	7	2.84×10^{-4}	1.41×10^{-5}	0.82	0.72	0.00253
18	7	4.84×10^{-5}	7.86×10^{-6}	0.14	0.67	0.00191

Table D.0.1: Experimental data: interval between images, estimated diffusion coefficient and error, p-values of the Shapiro-Wilk normality and the Kolmogorov-Smirnov tests.

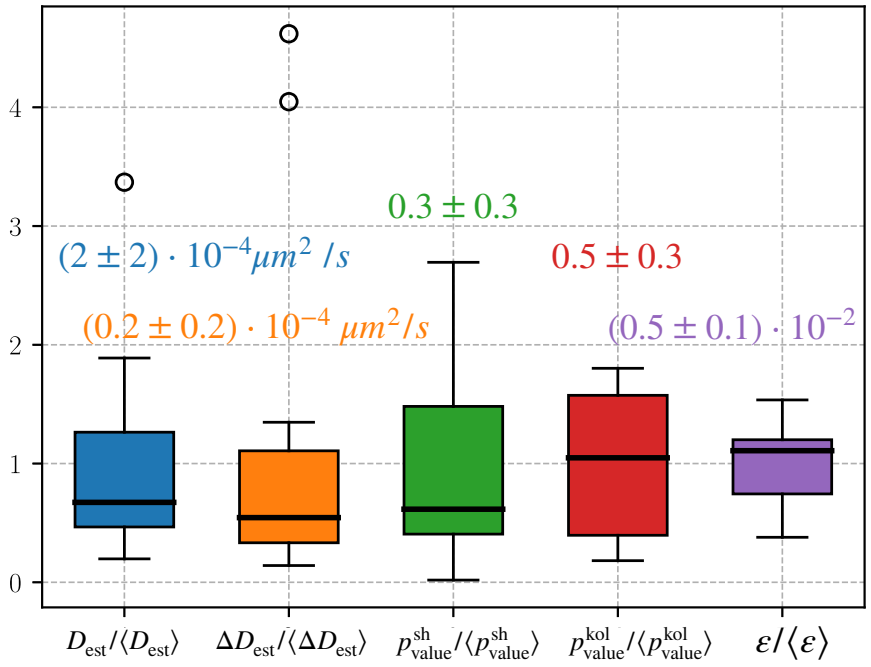

Figure D.7: Distributions of experimental results from table D.0.1 displayed as box plots. From the left to the right: estimated diffusion, estimated error, pvalue from shapiro test, pvalue from kolomogorov test, estimated photobleaching from the control area. Data are normalised with respect to the average of the distribution. The average value is reported above each boxplot with the same colour.

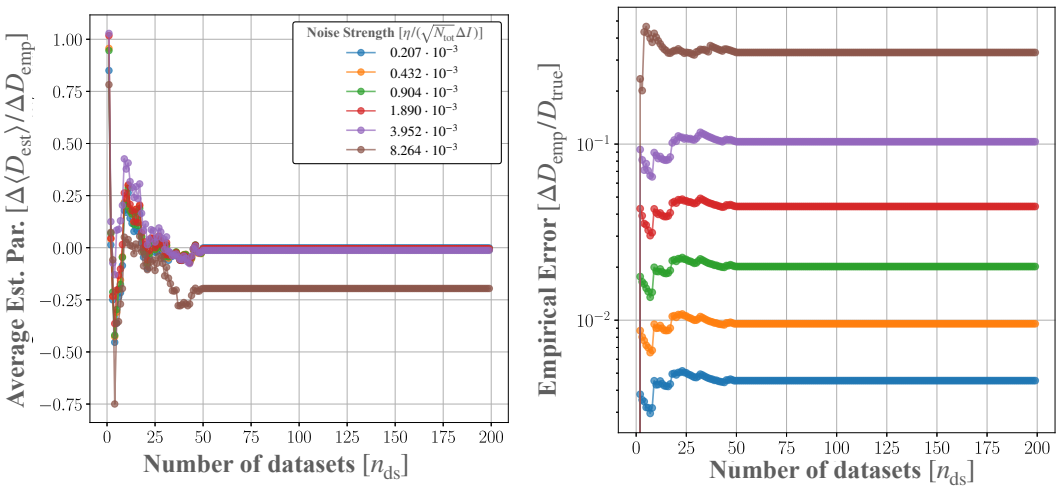

Figure D.8: Convergence of the average estimated value and the empirical error. On the left, it is shown the average estimated diffusion value $\langle D_{\text{est}}\rangle$ (normalised as $\Delta\langle D_{\text{est}}\rangle/\Delta D_{\text{emp}}$, with $\Delta\langle D_{\text{est}}\rangle = \langle D_{\text{est}}\rangle - D_{\text{true}}$, D_{true} the true diffusion value of the system and ΔD_{emp}, the empirical error computed as in section 4.4.2 for all 200 datasets) as a function of the number of simulations considered n_{ds}. The multiple colours refer to different amplitudes of the noise η, whose value is normalised with the typical signal drop-off ΔI and the total number of points $\sqrt{N_{\text{tot}}}$ per dataset. On the right, the figure represents the empirical error, ΔD_{emp}, computed as a function of the number of simulations considered. The different colours represent different noise strengths, as on the left panel.

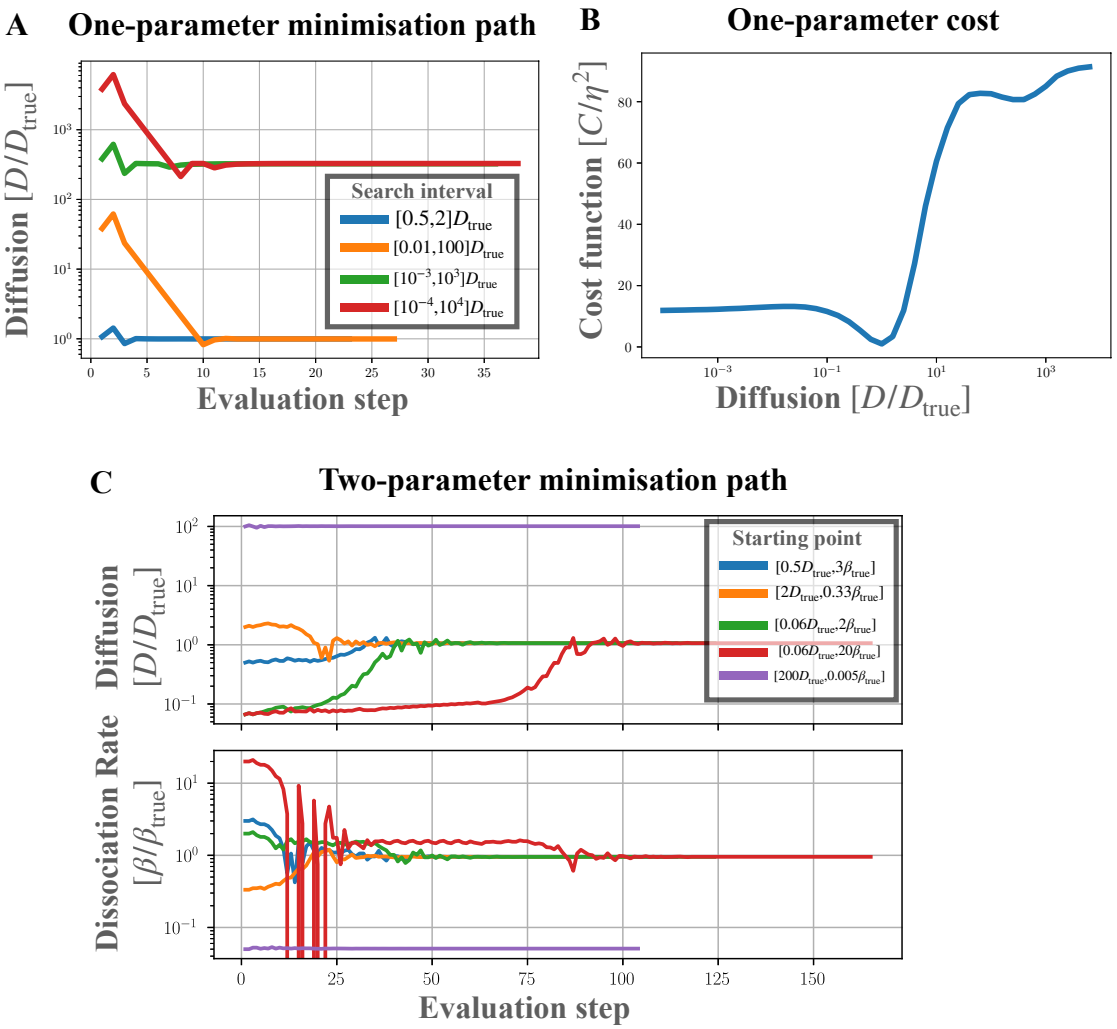

Figure D.9: Result of one-parameter (diffusion only) and two-parameter (diffusion and dissociation rate) minimisation methods for different initial parameters. Panel **A**: diffusion value (normalised with the true parameter of the system D_{true}) at different cost function evaluation steps during its minimization by the Brent's method. The different colours represent different initial search interval $[a, b]$. The first function evaluations are at $D_0 = b - 0.618(b - a)$ and $D_1 = a + 0.618(b - a)$, given by the golden rule as explained in table 4.6.1. Panel **B**: cost function (normalised with the amplitude of the noise η) for different diffusion value. Panel **C**: diffusion and dissociation rate value (normalised with the true parameter of the system D_{true} and β_{true}) at different cost function evaluation during its minimization by the Nelder-Mead's method. The different colours represent different initial starting points.

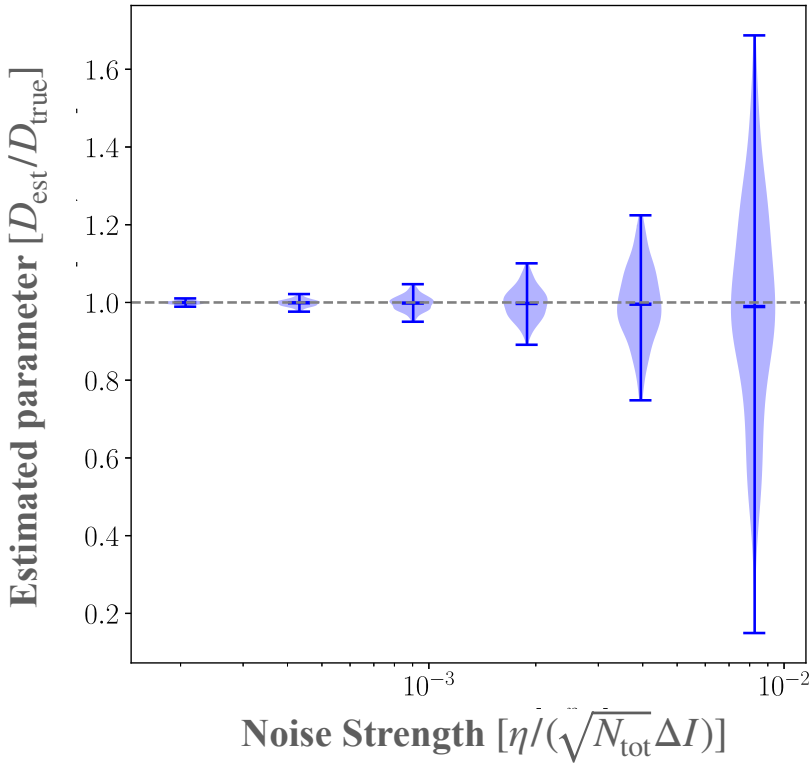

Figure D.10: HiFRAP combined with a benchmarking method. Violinplot of the estimated parameter distribution D_{est}/D_{true} for different noise strength (the typical amplitude η is normalised with respect to the square root of the total number of point $\sqrt{N_{\text{tot}}}$ and the typical signal drop-off ΔI). The estimated diffusion value D_{est} is obtained running HiFRAP minimisation in the interval $[D_{\text{bench}}/5, 5D_{\text{bench}}]$, where D_{bench} is obtained from the benchmarking method based on a temporal fit (Goehring et al., 2010). The dashed gray line represents the reference value $D_{\text{est}}/D_{\text{true}} = 1$.

REFERENCES

Abenza, J. F., Couturier, E., Dodgson, J., Dickmann, J., Chessel, A., Dumais, J., & Salas, R. E. C. (2015). Wall mechanics and exocytosis define the shape of growth domains in fission yeast. *Nature communications*, *6*(1), 8400.

Aggarwal, C. C., Aggarwal, L.-F., & Lagerstrom-Fife. (2020). *Linear algebra and optimization for machine learning* (Vol. 156). Springer.

Ahmed, W. W., & Saif, T. A. (2014). Active transport of vesicles in neurons is modulated by mechanical tension. *Scientific reports*, *4*(1), 4481.

Albert, C. G., & Rath, K. (2020). Gaussian process regression for data fulfilling linear differential equations with localized sources. *Entropy*, *22*(2), 152.

Alberts, B., Johnson, A., Lewis, J., Morgan, D., Raff, M., Roberts, K., & Walter, P. (2014). *Molecular biology of the cell* (6th). Garland Science.

Alberts, B., Johnson, A., Lewis, J., Raff, M., Roberts, K., & Walter, P. (2002). *Molecular biology of the cell* (4th). Garland Science. https://www.ncbi.nlm.nih.gov/books/NBK26910/

Ali, O., Guillou, H., Destaing, O., Albiges-Rizo, C., Block, M. R., & Fourcade, B. (2011). Cooperativity between integrin activation and mechanical stress leads to integrin clustering. *Biophysical journal*, *100*(11), 2595–2604.

Axelrod, D., Koppel, D. E., Schlessinger, J., Elson, E., & Webb, W. W. (1976). Mobility measurement by analysis of fluorescence photobleaching recovery kinetics. *Biophysical Journal*, *16*(9), 1055–1069. https://doi.org/10.1016/S0006-3495(76)85755-4

Baxter, B. (2002). Preconditioned conjugate gradients, radial basis functions, and toeplitz matrices. *Computers & Mathematics with Applications*, *43*(3-5), 305–318.

Berg, J. M., Tymoczko, J. L., Gatto, G. J., & Stryer, L. (2015). Peptide bonds: Building blocks of proteins [Describes the formation of peptide bonds and their role in protein structure and stability.]. *Biochemistry*, *8*, 70–72.

Berger, V. W., & Zhou, Y. (2014). Kolmogorov–smirnov test: Overview. *Wiley statsref: Statistics reference online*.

Berk, D. A., Yuan, F., Leunig, M., & Jain, R. K. (1993). Fluorescence photobleaching with spatial fourier analysis: Measurement of diffusion in light-scattering media. *Biophysical Journal*, *65*(6), 2428–2436. https://doi.org/10.1016/S0006-3495(93)81326-2

Berkovich, R., Wolfenson, H., Eisenberg, S., Ehrlich, M., Weiss, M., Klafter, J., Henis, Y. I., & Urbakh, M. (2011). Accurate quantification of diffusion and binding kinetics of non-integral membrane proteins by frap. *Traffic*, *12*(11), 1648–1657.

Besser, A., & Safran, S. A. (2006). Force-induced adsorption and anisotropic growth of focal adhesions. *Biophysical journal*, *90*(10), 3469–3484.

Bianchi, F., Syga, Ł., Moiset, G., Spakman, D., Schavemaker, P. E., Punter, C. M., Seinen, A.-B., van Oijen, A. M., Robinson, A., & Poolman, B. (2018). Steric exclusion and protein conformation determine the localization of plasma membrane transporters. *Nature Communications*, *9*(1), 501. https://doi.org/10.1038/s41467-018-02864-2

Bläßle, A., Soh, G., Braun, T., Mörsdorf, D., Preiß, H., Jordan, B. M., & Müller, P. (2018). Quantitative diffusion measurements using the open-source software PyFRAP [Number: 1 Publisher: Nature Publishing Group]. *Nature Communications*, *9*(1), 1582. https://doi.org/10.1038/s41467-018-03975-6

Blumenthal, D., Goldstien, L., Edidin, M., & Gheber, L. A. (2015). Universal approach to FRAP analysis of arbitrary bleaching patterns. *Scientific Reports*, *5*, 11655. https://doi.org/10.1038/srep11655

Brangwynne, C. P., Koenderink, G. H., MacKintosh, F. C., & Weitz, D. A. (2009). Intracellular transport by active diffusion. *Trends in cell biology*, *19*(9), 423–427.

Brent, R. P. (2013). *Algorithms for minimization without derivatives*. Courier Corporation.

Buda, R., Liu, Y., Yang, J., Hegde, S., Stevenson, K., Bai, F., & Pilizota, T. (2016). Dynamics of escherichia coli's passive response to a sudden decrease in external osmolarity. *Proceedings of the National Academy of Sciences*, *113*(40), E5838–E5846.

Cai, D., Verhey, K. J., & Meyhöfer, E. (2007). Tracking single kinesin molecules in the cytoplasm of mammalian cells. *Biophysical journal*, *92*(12), 4137–4144.

Cappelezzo, M., Capellari, C. A., Pezzin, S. H., & Coelho, L. A. (2007). Stokes-einstein relation for pure simple fluids. *The Journal of Chemical Physics*, *126*(22), 224516. https://doi.org/10.1063/1.2738063

Carl Zeiss Microscopy GmbH. (2019, May). *Principles of fluorescence and fluorescence microscopy* (tech. rep.). Carl Zeiss Microscopy GmbH.

Chen, Y., Lagerholm, B. C., Yang, B., & Jacobson, K. (2006). Methods to measure the lateral diffusion of membrane lipids and proteins. *Methods*, *39*(2), 147–153.

Chen, Y. e. a. (2017). Receptor-mediated cell mechanosensing. *Molecular biology of the cell vol. 28,23*.

Ciocanel, M.-V., Ding, L., Mastromatteo, L., Reichheld, S., Cabral, S., Mowry, K., & Sandstede, B. (2024). Parameter identifiability in PDE models of fluorescence recovery after photobleaching. *Bulletin of Mathematical Biology*, *86*(4), 36. https://doi.org/10.1007/s11538-024-01266-4

Ciocanel, M.-V., Kreiling, J. A., Gagnon, J. A., Mowry, K. L., & Sandstede, B. (2017). Analysis of active transport by fluorescence recovery after photobleaching. *Biophys. J.*, *112*(8), 1714–1725.

Cooper, G. (2009). *The cell: A molecular approach*. ASK PRESS.

Cowan, A. E., & Loew, L. M. (2023). Beyond analytic solution: Analysis of FRAP experiments by spatial simulation of the forward problem. *Biophys. J.*, *122*(18), 3722–3737.

Cruz, S., Muñoz, S., Manjón, E., García, P., & Sanchez, Y. (2013). The fission yeast cell wall stress sensor-like proteins mtl2 and wsc1 act by turning on

the gtp ase rho1p but act independently of the cell wall integrity pathway. *Microbiologyopen*, *2*(5), 778–794.

Das, S., Riest, J., Winkler, R. G., Gompper, G., Dhont, J. K., & Nägele, G. (2018). Clustering and dynamics of particles in dispersions with competing interactions: Theory and simulation. *Soft Matter*, *14*(1), 92–103.

Davì, V., Chevalier, L., Guo, H., Tanimoto, H., Barrett, K., Couturier, E., Boudaoud, A., & Minc, N. (2019). Systematic mapping of cell wall mechanics in the regulation of cell morphogenesis. *Proceedings of the National Academy of Sciences*, *116*(28), 13833–13838.

Davì, V., & Minc, N. (2015). Mechanics and morphogenesis of fission yeast cells. *Current opinion in microbiology*, *28*, 36–45.

Davì, V., Tanimoto, H., Ershov, D., Haupt, A., De Belly, H., Le Borgne, R., Couturier, E., Boudaoud, A., & Minc, N. (2018). Mechanosensation dynamically coordinates polar growth and cell wall assembly to promote cell survival. *Developmental cell*, *45*(2), 170–182.

Deschout, H., Hagman, J., Fransson, S., Jonasson, J., Rudemo, M., Lorén, N., & Braeckmans, K. (2010). Straightforward FRAP for quantitative diffusion measurements with a laser scanning microscope. *Optics Express*, *18*(22), 22886–22905. https://doi.org/10.1364/OE.18.022886

Deschout, H., Raemdonck, K., Demeester, J., De Smedt, S. C., & Braeckmans, K. (2014). FRAP in pharmaceutical research: Practical guidelines and applications in drug delivery. *Pharm. Res.*, *31*(2), 255–270.

Dodgson, J., Chessel, A., Yamamoto, M., Vaggi, F., Cox, S., Rosten, E., Albrecht, D., Geymonat, M., Csikasz-Nagy, A., Sato, M., et al. (2013). Spatial segregation of polarity factors into distinct cortical clusters is required for cell polarity control. *Nature communications*, *4*(1), 1834.

Dupres, V., Alsteens, D., Wilk, S., Hansen, B., Heinisch, J. J., & Dufrêne, Y. F. (2009). The yeast wsc1 cell surface sensor behaves like a nanospring in vivo. *Nature chemical biology*, *5*(11), 857–862.

Elowitz, M. B., Surette, M. G., Wolf, P.-E., Stock, J. B., & Leibler, S. (1999). Protein mobility in the cytoplasm of escherichia coli. *Journal of Bacteriology*, *181*(1), 197–203. Retrieved April 16, 2023, from https://www.ncbi.nlm.nih.gov/pmc/articles/PMC103549/

Erami, Z., Herrmann, D., Warren, S. C., Nobis, M., McGhee, E. J., Lucas, M. C., Leung, W., Reischmann, N., Mrowinska, A., Schwarz, J. P., Kadir, S., Conway, J. R. W., Vennin, C., Karim, S. A., Campbell, A. D., Gallego-Ortega, D., Magenau, A., Murphy, K. J., Ridgway, R. A., ... Timpson, P. (2016). Intravital FRAP imaging using an E-cadherin-GFP mouse reveals disease- and drug-dependent dynamic regulation of cell-cell junctions in live tissue. *Cell Rep.*, *14*(1), 152–167.

Erlykin, A., Lagutin, A., & Wolfendale, A. (2003). Properties of the interstellar medium and the propagation of cosmic rays in the galaxy. *Astroparticle Physics*, *19*(3), 351–362.

Ferenczi, E. A., Tan, X., & Huang, C. L.-H. (2019). Principles of optogenetic methods and their application to cardiac experimental systems. *Front. Physiol.*, *10*, 1096.

Fernandes, L. D., Guseva, K., & De Moura, A. P. (2017). Cooperative response and clustering: Consequences of membrane-mediated interactions among mechanosensitive channels. *Physical Review E*, *96*(2), 022410.

Ferrai, C., & Schulte, C. (2024). Mechanotransduction in stem cells. *European Journal of Cell Biology*, *103*(2), 151417.

Ferrand, P., Wenger, J., & Rigneault, H. (2011). Fluorescence correlation spectroscopy. *Single Molecule Analysis: Methods and Protocols*, 181–195.

Ferrari, C. C., & Hubinger, M. D. (2008). Evaluation of the mechanical properties and diffusion coefficients of osmodehydrated melon cubes. *International journal of food science & technology*, *43*(11), 2065–2074.

Frieden, E. (1975). Non-covalent interactions: Key to biological flexibility and specificity. *Journal of chemical education*, *52*(12), 754.

Fruleux, A., Verger, S., & Boudaoud, A. (2019). Feeling stressed or strained? a biophysical model for cell wall mechanosensing in plants. *Frontiers in Plant Science*, *10*, 757.

Ganguly, S., Singh, P., Manoharlal, R., Prasad, R., & Chattopadhyay, A. (2009). Differential dynamics of membrane proteins in yeast. *Biochemical and Biophysical Research Communications*, *387*(4), 661–665. https://doi.org/10.1016/j.bbrc.2009.07.054

Gao, F., & Han, L. (2012). Implementing the nelder-mead simplex algorithm with adaptive parameters. *Computational Optimization and Applications*, *51*(1), 259–277.

Geiger, A. C. (2021, April 28). *Fourier transform fluorescence recovery after photobleaching with patterned illumination* [thesis]. Purdue University Graduate School. https://doi.org/10.25394/PGS.14498592.v1

Giannini, S., Gutierrez, R., Maruccio, G., Kirczenow, G., & Cingolani, R. (2011). Molecular interactions in antibody-antigen complexes: Role of van der waals forces [Explores how Van der Waals forces contribute to the binding and release dynamics in antibody-antigen interactions.]. *Journal of Molecular Recognition*, *24*(1), 123–130. https://doi.org/10.1002/jmr.1051

Goehring, N. W., Chowdhury, D., Hyman, A. A., & Grill, S. W. (2010). FRAP analysis of membrane-associated proteins: Lateral diffusion and membrane-cytoplasmic exchange. *Biophysical Journal*, *99*(8), 2443–2452. https://doi.org/10.1016/j.bpj.2010.08.033

Golub, G. H., & Pereyra, V. (1973). The differentiation of pseudo-inverses and nonlinear least squares problems whose variables separate. *SIAM J. Numer. Anal.*, *10*(2), 413–432.

Góra, P. F. (2006). The theory of brownian motion: A hundred years' anniversary. *The 19th Marian Smoluchowski Symposium on Statistical Physics*, 52–57.

Goussis, D. A. (2012). Quasi steady state and partial equilibrium approximations: Their relation and their validity. *Combustion Theory and Modelling*, *16*(5), 869–926.

Greenfield, D., McEvoy, A. L., Shroff, H., Crooks, G. E., Wingreen, N. S., Betzig, E., & Liphardt, J. (2009). Self-organization of the escherichia coli chemotaxis network imaged with super-resolution light microscopy. *PLoS biology*, *7*(6), e1000137.

Hamant, O., & Haswell, E. S. (2017). Life behind the wall: Sensing mechanical cues in plants. *BMC biology*, *15*, 1–9.

Hardin, J. (2011). Chapter 14 - imaging embryonic morphogenesis in c. elegans. In J. H. Rothman & A. Singson (Eds.), *Caenorhabditis elegans: Molecular genetics and development* (pp. 377–412, Vol. 106). Academic Press. https://doi.org/https://doi.org/10.1016/B978-0-12-544172-8.00014-1

Hillsley, A., Stein, J., Tillberg, P. W., Stern, D. L., & Funke, J. (2024). A bayesian solution to count the number of molecules within a diffraction limited spot. *bioRxiv*. https://doi.org/10.1101/2024.04.18.590066

Hoebe, R., Van Oven, C., Gadella Jr, T., Dhonukshe, P., Van Noorden, C., & Manders, E. (2007). Controlled light-exposure microscopy reduces photobleaching and phototoxicity in fluorescence live-cell imaging. *Nature biotechnology*, *25*(2), 249–253.

Ishikawa-Ankerhold, H., Ankerhold, R., & Drummen, G. (2014, October). Fluorescence recovery after photobleaching (frap). In *Els*. John Wiley & Sons, Ltd. https://doi.org/10.1002/9780470015902.a0003114

Jacobson, K., Ishihara, A., & Inman, R. (1987). Lateral diffusion of proteins in membranes. *Annual Review of Physiology*, *49*, 163–175. https://doi.org/10.1146/annurev.ph.49.030187.001115

Javanainen, M., Martinez-Seara, H., Metzler, R., & Vattulainen, I. (2017). Diffusion of integral membrane proteins in protein-rich membranes. *The journal of physical chemistry letters*, *8*(17), 4308–4313.

Johnson, M. L., & Faunt, L. M. (1992). Parameter estimation by least-squares methods. In *Methods in enzymology* (pp. 1–37, Vol. 210). Elsevier.

Jönsson, P., Jonsson, M. P., Tegenfeldt, J. O., & Höök, F. (2008). A method improving the accuracy of fluorescence recovery after photobleaching analysis. *Biophysical Journal*, *95*(11), 5334–5348. https://doi.org/10.1529/biophysj.108.134874

Julien, J.-D. (2015). *Physical basis of morphogenesis: Coupling between mechanics and growth of plants and yeast* [Doctoral dissertation, Ecole normale supérieure de lyon-ENS LYON].

Kang, M., Day, C. A., DiBenedetto, E., & Kenworthy, A. K. (2010). A quantitative approach to analyze binding diffusion kinetics by confocal frap. *Biophysical journal*, *99*(9), 2737–2747.

Kang, M., Day, C. A., Kenworthy, A. K., & DiBenedetto, E. (2012). Simplified equation to extract diffusion coefficients from confocal FRAP data. *Traffic (Copenhagen, Denmark)*, *13*(12), 1589–1600. https://doi.org/10.1111/tra.12008

Kang, M., & Kenworthy, A. K. (2008). A closed-form analytic expression for frap formula for the binding diffusion model. *Biophysical journal*, *95*(2), L13–L15.

Karnakov, P., Litvinov, S., & Koumoutsakos, P. (2024). Solving inverse problems in physics by optimizing a discrete loss: Fast and accurate learning without neural networks. *PNAS Nexus*, *3*(1), gae005.

Klaus, C. J. S. (2016). Analysis of diffusion in curved surfaces and its application to tubular membranes.

Kock, C., Dufrêne, Y. F., & Heinisch, J. J. (2015). Up against the wall: Is yeast cell wall integrity ensured by mechanosensing in plasma membrane microdomains? *Applied and environmental microbiology*, *81*(3), 806–811.

Kourtis, N., & Tavernarakis, N. (2017). Protein synthesis rate assessment by fluorescence recovery after photobleaching (FRAP). *Bio Protoc.*, *7*(5).

Koyano, Y., Yatabe, K., & Oikawa, Y. (2018). Infinite-dimensional SVD for revealing microphone array's characteristics. *Appl. Acoust.*, *129*, 116–125.

Lamiré, L.-A., Milani, P., Runel, G., Kiss, A., Arias, L., Vergier, B., de Bossoreille, S., Das, P., Cluet, D., Boudaoud, A., & Grammont, M. (2020). Gradient in cytoplasmic pressure in germline cells controls overlying epithelial cell morphogenesis. *PLOS Biology*, *18*(11), 1–30. https://doi.org/10.1371/journal.pbio.3000940

Lebon, G., Warne, T., Edwards, P. C., Bennett, K., Langmead, C. J., Leslie, A. G., & Tate, C. G. (2012). Agonist-bound adenosine a2a receptor structures reveal common features of gpcr activation. *Nature*, *482*(7384), 549–555. https://doi.org/10.1038/nature10753

Lele, T., Wagner, S. R., Nickerson, J. A., & Ingber, D. E. (2006). Methods for measuring rates of protein binding to insoluble scaffolds in living cells: Histone h1-chromatin interactions. *Journal of Cellular Biochemistry*, *99*(5), 1334–1342. https://doi.org/10.1002/jcb.20997

Li, H., Ye, F., Ren, J.-Y., Wang, P.-Y., Du, L.-L., & Liu, J.-L. (2018). Active transport of cytoophidia in schizosaccharomyces pombe. *The FASEB Journal*, *32*(11), 5891.

Lippincott-Schwartz, J., Snapp, E. L., & Phair, R. D. (2018). The development and enhancement of frap as a key tool for investigating protein dynamics. *Biophysical Journal*, *115*(7), 1146–1155. https://doi.org/10.1016/j.bpj.2018.08.007

Liu, Z., Lemma, T., & Pawliszyn, J. (2006). Capillary isoelectric focusing coupled with dynamic imaging detection: A one-dimensional separation for two-dimensional protein characterization. *J. Proteome Res.*, *5*(5), 1246–1251.

Long, M., Lü, S., & Sun, G. (2006). Kinetics of receptor-ligand interactions in immune responses. *Cell Mol Immunol*, *3*(2), 79–86.

Lorén, N., Hagman, J., Jonasson, J. K., Deschout, H., Bernin, D., Cella-Zanacchi, F., Diaspro, A., McNally, J. G., Ameloot, M., Smisdom, N., Nydén, M., Hermansson, A.-M., Rudemo, M., & Braeckmans, K. (2015). Fluorescence recovery after photobleaching in material and life sciences: Putting theory into practice. *Quarterly Reviews of Biophysics*, *48*(3), 323–387. https://doi.org/10.1017/S0033583515000013

Lorenzetti, E. (2021). *Modelling mechanosensor dynamics in fission yeast*. https://hdl.handle.net/20.500.12608/3768

MacKintosh, F. C., & Schmidt, C. F. (2010). Active cellular materials. *Current opinion in cell biology*, *22*(1), 29–35.

Mannam, V., Zhang, Y., Yuan, X., Ravasio, C., & Howard, S. S. (2020). Machine learning for faster and smarter fluorescence lifetime imaging microscopy. *Journal of Physics: Photonics*, *2*(4), 042005.

Martinac. (2004). Mechanosensitive ion channels: Molecules of mechanotransduction.

Martinière, A., Lavagi, I., Nageswaran, G., Rolfe, D. J., Maneta-Peyret, L., Luu, D.-T., Botchway, S. W., Webb, S. E. D., Mongrand, S., Maurel, C., Martin-Fernandez, M. L., Kleine-Vehn, J., Friml, J., Moreau, P., & Runions, J. (2012). Cell wall constrains lateral diffusion of plant plasma-membrane

proteins. *Proceedings Of The National Academy Of Sciences Of The United States Of America*, *109*(31), 12805–12810. https://doi.org/10.1073/pnas.1202040109

McNally, J. G. (2008). Quantitative FRAP in analysis of molecular binding dynamics in vivo. *Methods in Cell Biology*, *85*, 329–351. https://doi.org/10.1016/S0091-679X(08)85014-5

Merchant, F. A., & Periasamy, A. (2008). Chapter 12 - fluorescence imaging. In Q. Wu, F. A. Merchant, & K. R. Castleman (Eds.), *Microscope image processing* (pp. 247–297). Academic Press. https://doi.org/https://doi.org/10.1016/B978-0-12-372578-3.00012-X

Mishra, R., Minc, N., & Peter, M. (2022). Cells under pressure: How yeast cells respond to mechanical forces. *Trends in Microbiology*, *30*(5), 495–510.

Monod, J., Wyman, J., & Changeux, J. P. (1965). On the nature of allosteric transitions: A plausible model. *Journal of Molecular Biology*, *12*(1), 88–118. https://doi.org/10.1016/S0022-2836(65)80285-6

Monshausen, G. B., & Gilroy, S. (2009). Feeling green: Mechanosensing in plants.

Montero Llopis, P., Sliusarenko, O., Heinritz, J., & Jacobs-Wagner, C. (2012). In vivo biochemistry in bacterial cells using FRAP: Insight into the translation cycle. *Biophys. J.*, *103*(9), 1848–1859.

Mueller, F., Mazza, D., Stasevich, T. J., & McNally, J. G. (2010). Frap and kinetic modeling in the analysis of nuclear protein dynamics: What do we really know? *Current opinion in cell biology*, *22*(3), 403–411.

Muller, N., Piel, M., Calvez, V., Voituriez, R., Gonçalves-Sá, J., Guo, C.-L., Jiang, X., Murray, A., & Meunier, N. (2016). A predictive model for yeast cell polarization in pheromone gradients. *PLoS computational biology*, *12*(4), e1004795.

Municio-Diaz, C., Muller, E., Drevensek, S., Fruleux, A., Lorenzetti, E., Boudaoud, A., & Minc, N. (2022). Mechanobiology of the cell wall - insights from tip-growing plant and fungal cells. *Journal of Cell Science*, *135*(21), jcs259208. https://doi.org/10.1242/jcs.259208

Nam, K., & Wolf-Watz, M. (2023). Protein dynamics: The future is bright and complicated! *Structural Dynamics*, *10*(1).

Neeli-Venkata, R., Diaz, C. M., Celador, R., Sanchez, Y., & Minc, N. (2021). Detection of surface forces by the cell-wall mechanosensor wsc1 in yeast. *Developmental Cell*, *56*(20), 2856–2870.e7. https://doi.org/10.1016/j.devcel.2021.09.024

Nelder, J. A., & Mead, R. (1965). A simplex method for function minimization. *The computer journal*, *7*(4), 308–313.

Nicolas, A., Geiger, B., & Safran, S. A. (2004). Cell mechanosensitivity controls the anisotropy of focal adhesions. *Proceedings of the national academy of sciences*, *101*(34), 12520–12525.

Odermatt, P. D., Miettinen, T. P., Lemière, J., Kang, J. H., Bostan, E., Manalis, S. R., Huang, K. C., & Chang, F. (2021). Variations of intracellular density during the cell cycle arise from tip-growth regulation in fission yeast. *Elife*, *10*, e64901.

Oide, S., Tanaka, Y., Watanabe, A., & Inui, M. (2019). Carbohydrate-binding property of a cell wall integrity and stress response component (wsc) do-

main of an alcohol oxidase from the rice blast pathogen pyricularia oryzae. *Enzyme and microbial technology*, *125*, 13–20.

Ongie, G., Jalal, A., Metzler, C. A., Baraniuk, R. G., Dimakis, A. G., & Willett, R. (2020). Deep learning techniques for inverse problems in imaging. *IEEE Journal on Selected Areas in Information Theory*, *1*(1), 39–56.

Orr, A. W., Helmke, B. P., Blackman, B. R., & Schwartz, M. A. (2006). Mechanisms of mechanotransduction. *Developmental cell*, *10*(1), 11–20.

Papáček, Š., Kaňa, R., & Matonoha, C. (2013). Estimation of diffusivity of phycobilisomes on thylakoid membrane based on spatio-temporal FRAP images. *Math. Comput. Model.*, *57*(7-8), 1907–1912.

Paraschiv, A., Hegde, S., Ganti, R., Pilizota, T., & Šarić, A. (2020). Dynamic clustering regulates activity of mechanosensitive membrane channels. *Physical Review Letters*, *124*(4), 048102.

Pérez, P., Cortés, J. C., Cansado, J., & Ribas, J. C. (2018). Fission yeast cell wall biosynthesis and cell integrity signalling. *The Cell Surface*, *4*, 1–9.

Piasecki, J. (2007). Centenary of marian smoluchowski's theory of brownian motion. *Acta Physica Polonica B*, *38*(5).

Pilling, A. D., Horiuchi, D., Lively, C. M., & Saxton, W. M. (2006). Kinesin-1 and dynein are the primary motors for fast transport of mitochondria in drosophila motor axons. *Molecular biology of the cell*, *17*(4), 2057–2068.

Prabhune, M., Rehfeldt, F., & Schmidt, C. F. (2017). Molecular force sensors to measure stress in cells. *Journal of Physics D: Applied Physics*, *50*(23), 233001.

Press, W. H., Teukolsky, S. A., Vetterling, W. T., & Flannery, B. P. (2007). *Numerical recipes*. Cambridge University Press.

Qian, J., Tang, J., & Stahl, P. D. (2000). Disulfide bonds and the stability of proteins: Implications for protein function [Discusses the role of disulfide bonds in stabilizing protein structures, including extracellular proteins such as insulin.]. *Journal of Biological Chemistry*, *275*(16), 10383–10386. https://doi.org/10.1074/jbc.M000852200

Quemeneur, F., Sigurdsson, J. K., Renner, M., Atzberger, P. J., Bassereau, P., & Lacoste, D. (2014). Shape matters in protein mobility within membranes. *Proceedings of the National Academy of Sciences*, *111*(14), 5083–5087.

Radhakrishnan, K., Halász, Á., McCabe, M. M., Edwards, J. S., & Wilson, B. S. (2012). Mathematical simulation of membrane protein clustering for efficient signal transduction. *Annals of biomedical engineering*, *40*, 2307–2318.

Rao, C. R. (1973). *Linear statistical inference and its applications* (2nd). John Wiley & Sons.

Récamier, V. (2013, November). *Single particle imaging in the cell nucleus : a quantitative approach* (Publication No. 2013PA05T091) [Theses]. Université René Descartes - Paris V. https://theses.hal.science/tel-00998389

Recouvreux, P., & Lenne, P.-F. (2016). Molecular clustering in the cell: From weak interactions to optimized functional architectures. *Current opinion in cell biology*, *38*, 18–23.

Recouvreux, P., Pai, P., Dunsing, V., Torro, R., Ludanyi, M., Mélénec, P., Boughzala, M., Bertrand, V., & Lenne, P.-F. (2024). Transfer of polarity information via diffusion of wnt ligands in c. elegans embryos. *Curr. Biol.*, *34*(9), 1853–1865.e6.

Reits, E. A. J., & Neefjes, J. J. (2001). From fixed to FRAP: Measuring protein mobility and activity in living cells [Number: 6 Publisher: Nature Publishing Group]. *Nature Cell Biology*, *3*(6), E145–E147. https://doi.org/10.1038/35078615

Renn, J. (2005). Einstein's invention of brownian motion. *Annalen der Physik*, *517*, 23–37.

Ries, J., Klose, C., Walch-Solimena, C., & Schwille, P. (2008). How to measure slow diffusion in yeast cell membranes. *Biophotonics: Photonic Solutions for Better Health Care*, *6991*, 136–143. https://doi.org/10.1117/12.787043

Rodicio, R., & Heinisch, J. J. (2010). Together we are strong—cell wall integrity sensors in yeasts. *Yeast*, *27*(8), 531–540.

Röding, M., Lacroix, L., Krona, A., Gebäck, T., & Lorén, N. (2019). A highly accurate pixel-based FRAP model based on spectral-domain numerical methods. *Biophys. J.*, *116*(7), 1348–1361.

Ronceray, P. (2024). Learning dynamical models from stochastic trajectories. *arXiv preprint arXiv:2406.02363*.

Saffman, P., & Delbrück, M. (1975). Brownian motion in biological membranes. *Proceedings of the National Academy of Sciences*, *72*(8), 3111–3113.

Saito, T., Matsunaga, D., & Deguchi, S. (2022). Long-term molecular turnover of actin stress fibers revealed by advection-reaction analysis in fluorescence recovery after photobleaching. *PLoS One*, *17*(11), e0276909.

Sánchez, A. D., & Wio, H. (1997). Trapping kinetics in diffusion-limited bimolecular reactions sources within the galanin model. *Physica A: Statistical Mechanics and its Applications*, *237*(3-4), 452–470.

Schavemaker, P. E., Boersma, A. J., & Poolman, B. (2018). How important is protein diffusion in prokaryotes? *Frontiers in molecular biosciences*, *5*, 93.

Schwarz, U. S., Erdmann, T., & Bischofs, I. B. (2006). Focal adhesions as mechanosensors: The two-spring model. *Biosystems*, *83*(2-3), 225–232.

Secomb, T., Hsu, R., & Pries, A. (2001). Motion of red blood cells in a capillary with an endothelial surface layer: Effect of flow velocity. *American Journal of Physiology-Heart and Circulatory Physiology*, *281*(2), H629–H636.

Segre, P. S., & Taylor, E. D. (2019). Large ants do not carry their fair share: Maximal load-carrying performance of leaf-cutter ants (atta cephalotes). *Journal of Experimental Biology*, *222*(12), jeb199240.

Shapiro, S. S., & Wilk, M. B. (1965). An analysis of variance test for normality (complete samples). *Biometrika*, *52*(3-4), 591–611.

Sharan, M., Yadav, A. K., Singh, M., Agarwal, P., & Nigam, S. (1996). A mathematical model for the dispersion of air pollutants in low wind conditions. *Atmospheric Environment*, *30*(8), 1209–1220.

Shen, Y., Li, B., & Chen, Y. (2011). An iterative solution of weighted total least-squares adjustment. *Journal of geodesy*, *85*, 229–238.

Singer, S. J., & Nicolson, G. L. (1972). The fluid mosaic model of the structure of cell membranes: Cell membranes are viewed as two-dimensional solutions of oriented globular proteins and lipids. *Science*, *175*(4023), 720–731.

Sitarska, E., & Diz-Muñoz, A. (2020). Pay attention to membrane tension: Mechanobiology of the cell surface. *Current opinion in cell biology*, *66*, 11–18.

Skalak, R., & Brånemark, P. (1969). Deformation of red blood cells in capillaries. *Science*, *164*(3880), 717–719.

Skou, J. C. (1998). The identification of the sodium pump. *Bioscience reports*, *18*(4), 155–169.

Sprague, B. L., & McNally, J. G. (2005). FRAP analysis of binding: Proper and fitting. *Trends in Cell Biology*, *15*(2), 84–91. https://doi.org/10.1016/j.tcb.2004.12.001

Straub, H., Bigger, C. M., Valentin, J., Abt, D., Qin, X.-H., Eberl, L., Maniura-Weber, K., & Ren, Q. (2019). Bacterial adhesion on soft materials: Passive physicochemical interactions or active bacterial mechanosensing? *Advanced healthcare materials*, *8*(8), 1801323.

Taheri-Talesh, N., Xiong, Y., & Oakley, B. R. (2012). The functions of myosin ii and myosin v homologs in tip growth and septation in aspergillus nidulans. *PloS one*, *7*(2), e31218.

Taylor, N. O., Wei, M.-T., Stone, H. A., & Brangwynne, C. P. (2019). Quantifying dynamics in phase-separated condensates using fluorescence recovery after photobleaching. *Biophys. J.*, *117*(7), 1285–1300.

Thompson., D. (1917). *On growth and form*. Cambridge University Press.

Tolentino, T. P., Wu, J., Zarnitsyna, V. I., Fang, Y., Dustin, M. L., & Zhu, C. (2008). Measuring diffusion and binding kinetics by contact area frap. *Biophysical journal*, *95*(2), 920–930.

Tsibidis, G. D. (2009). Quantitative interpretation of binding reactions of rapidly diffusing species using fluorescence recovery after photobleaching. *Journal of Microscopy*, *233*(3), 384–390. https://doi.org/10.1111/j.1365-2818.2009.03132.x

Valdez-Taubas, J., & Pelham, H. R. B. (2003). Slow diffusion of proteins in the yeast plasma membrane allows polarity to be maintained by endocytic cycling. [Place: England]. *Curr Biol*, *13*(18), 1636–1640. https://doi.org/10.1016/j.cub.2003.09.001

Verbruggen, S. (2018). *Mechanobiology in health and disease*. Academic Press.

Vesga-Castro, C., Aldazabal, J., Vallejo-Illarramendi, A., & Paredes, J. (2022). Contractile force assessment methods for in vitro skeletal muscle tissues. *Elife*, *11*, e77204.

Viljoen, E. C., & Uebing, C. (1997). Diffusion of interacting lattice gases on heterogeneous surfaces. *Langmuir*, *13*(5), 1001–1009.

Vogel, C. (2002). Computational methods for inverse problems. *Frontiers in Applied Mathematics/SIAM*.

Wawra, S., Fesel, P., Widmer, H., Neumann, U., Lahrmann, U., Becker, S., Hehemann, J.-H., Langen, G., & Zuccaro, A. (2019). Fgb1 and wsc3 are in planta-induced β-glucan-binding fungal lectins with different functions. *New Phytologist*, *222*(3), 1493–1506.

Weber, A., Braybrook, S., Huflejt, M., Mosca, G., Routier-Kierzkowska, A.-L., & Smith, R. S. (2015). Measuring the mechanical properties of plant cells by combining micro-indentation with osmotic treatments. *Journal of experimental botany*, *66*(11), 3229–3241.

Welf, E. S., Naik, U. P., & Ogunnaike, B. A. (2012). A spatial model for integrin clustering as a result of feedback between integrin activation and integrin binding. *Biophysical journal*, *103*(6), 1379–1389.

Wieser, S., Weghuber, J., Sams, M., Stockinger, H., & Schütz, G. J. (2009). Cell-to-cell variability in the diffusion constants of the plasma membrane proteins CD59 and CD147. *Soft Matter*, *5*(17), 3287.

Wiggins, P., & Phillips, R. (2004). Analytic models for mechanotransduction: Gating a mechanosensitive channel. *Proceedings of the National Academy of Sciences*, *101*(12), 4071–4076.

Wiggins, P., & Phillips, R. (2005). Membrane-protein interactions in mechanosensitive channels. *Biophysical journal*, *88*(2), 880–902.

Wikström, M., Sharma, V., Kaila, V., & Hosler, J. (2015). New perspectives on proton pumping in cellular respiration. *Chemical Reviews*, *115*(5), 2196–2220. https://doi.org/10.1021/cr500448t

Wojcieszyn, J. W., Schlegel, R. A., Wu, E.-S., & Jacobson, K. A. (1981). Diffusion of injected macromolecules within the cytoplasm of living cells. *Proceedings of the National Academy of Sciences*, *78*(7), 4407–4410.

Wu, J., Fang, Y., Zarnitsyna, V. I., Tolentino, T. P., Dustin, M. L., & Zhu, C. (2008). A coupled diffusion-kinetics model for analysis of contact-area frap experiment. *Biophysical journal*, *95*(2), 910–919.

Yuste, S. B., Abad, E., & Lindenberg, K. (2014). A reaction–subdiffusion model of fluorescence recovery after photobleaching (FRAP). *J. Stat. Mech.*, *2014*(11), P11014.

Zarabadi, A. S., & Pawliszyn, J. (2015, February 4). *Accurate determination of the diffusion coefficient of proteins by fourier analysis with whole column imaging detection* [ACS publications] [Archive Location: world Publisher: American Chemical Society]. https://doi.org/10.1021/ac503069g

Zhang, F., Feustel, M. K., Skoda, M. W., Jacobs, R. M., Roosen-Runge, F., Seydel, T., Sztucki, M., & Schreiber, F. (2024). Effective interactions in protein solutions with and without clustering. *Physica A: Statistical Mechanics and its Applications*, 129995.

Zhang, G., Duan, Y., Pan, G., Chen, Q., Yang, H., & Zhang, Z. (2023). Parameter identification for partial differential equations with spatiotemporal varying coefficients. *arXiv preprint arXiv:2307.00035*.

ECOLE DOCTORALE

Title: Modélisation et Analyse de Données de la Dynamique des Protéines appliquées à un Mécanosenseur de la Levure Fissipare
Keywords: Protéines, inférence, mécanosensation, réaction-diffusion, biomécanique, modélisation
Abstract: La dynamique intracellulaire des molécules est fondamentale pour que les cellules maintiennent l'homéostasie et répondent aux stimuli environnementaux. Parmi ceux-ci, les forces mécaniques peuvent constituer une source potentielle de dommages en compromettant l'intégrité de la cellule. Pour faire face à ce risque, les organismes vivants sont dotés de mécanosenseurs, des récepteurs subcellulaires capables de déclencher une voie de signalisation biologique par un signal mécanique. Chez la levure à fission fissipare, un mécanosenseur, la protéine Wsc1, peut percevoir une contrainte excessive sur la paroi cellulaire et activer la synthèse de glucane pour renforcer la paroi. Notablement, la concentration de Wsc1 augmente dans la région comprimée de la paroi, formant des agrégats. Ce travail de thèse explore ce comportement de formation d'agrégat mécanosensible en développant des modèles et des méthodes d'inférence pour les données expérimentales de dynamique des protéines.
En établissant un cadre mathématique basé sur des équations aux dérivées partielles déterministes, je décris la dynamique de Wsc1 le long de la paroi cellulaire. Dans ce modèle, je considère deux mécanismes possibles de recrutement des protéines pour former des agrégats : soit par diffusion le long de la paroi cellulaire, soit par exocytose depuis le cytoplasme. De plus, en suivant des considérations chimiques, je suppose que l'affinité entre la paroi et la protéine Wsc1 augmente avec la compression de la paroi. Les équations de réaction-diffusion résultant de ce modèle reproduisent la formation d'agrégats après compression de la paroi cellulaire. De plus, le modèle prédit une échelle de temps plus longue pour la dynamique dans la région comprimée de la paroi cellulaire, en accord avec les résultats de l'expérience FRAP (Fluorescence Recovery After Photobleaching, redistribution de fluorescence après photoblanchiment), dont l'analyse est basée sur l'étude des images en temps réel reflétant la concentration spatio-temporelle de la molécule. Cependant, il n'est pas encore clair si le recrutement des protéines est dû à la diffusion, à l'échange avec le cytoplasme, ou aux deux. Pour cette raison, dans mon travail, je développe également une nouvelle méthode d'inférence pour l'expérience FRAP capable de distinguer différents types de dynamique. Mon analyse vise à quantifier les paramètres cinétiques, tels que le coefficient de diffusion et le taux d'échange, en minimisant la distance entre la prédiction du modèle de réaction-diffusion et les données réelles. La spécificité de mon approche réside dans l'utilisation de la réduction dimensionnelle pour calculer efficacement les paramètres sans avoir connaissance du profil initial après photoblanchiment. Cette nouvelle méthode est ensuite testée et validée sur des données artificielles. Les résultats montrent que cette méthode d'analyse est flexible, car elle peut fonctionner avec des données imparfaites où le rapport signal/bruit est faible, le nombre d'images est réduit et la fenêtre spatiale est restreinte. De plus, cette approche peut potentiellement être généralisée à des géométries complexes, telles que les surfaces courbées. Cette polyvalence est bien adaptée pour étudier la dynamique des protéines dans la paroi cellulaire de la levure fissipare. La méthode d'inférence est appliquée aux données expérimentales d'un autre mécanosenseur dans la paroi cellulaire, Mtl2, fournissant des valeurs raisonnables de coefficient de diffusion. Cependant, elle doit encore être testée sur des données réelles de la protéine Wsc1.
Dans l'ensemble, cette étude propose des méthodologies novatrices pour quantifier et comprendre la dynamique complexe des protéines au sein des cellules et des tissus.

Title : Modelling And Data Analysis of Protein Dynamics applied to a Fission Yeast Mechanosensor
Keywords : Proteins, inference, mecanosensing, reaction-diffusion, biomechanics, modelling
Abstract : Intracellular dynamics is fundamental for cells to maintain homeostasis and respond to environmental stimuli. Among these, mechanical forces can be a potential source of damage as they can compromise the integrity of the cell. To cope with this risk, living organisms are endowed with mechanosensors, i.e. receptor at the sub-cellular level able to trigger a biological pathway by a mechanical signal. In fission yeast, a mechanosensor, Wsc1 protein, perceives excessive stress on the cell wall and activates the glucan synthesis to keep this layer reinforced. More interestingly, Wsc1 concentration increases in the compressed region of the cell wall forming clusters. This work investigates this mechanosensitive clustering behaviour advancing models and inference method for experimental data of protein dynamics.
By setting a mathematical framework based on deterministic partial differential equations, I describe the Wsc1 dynamics along the cell wall. In this model, I consider two possible protein recruitment mechanisms for shaping clusters, either from the sides due to diffusion along the cell wall and from the cytoplasm by exocytotosis. Moreover, following chemical considerations, I suppose an affinity between the cell wall and the protein that increases with the cell wall compression. The resulting reaction-diffusion equations obtained by this model are able to reproduce the clustering behaviour after cell wall compression. In addition, the model correctly predicts a longer time-scale of the dynamics in the compressed region of the cell wall. This result is in agreement with the outcomes of FRAP (Fluorescence Recovery After Photobleaching) experiment, whose analysis is based on the study of time-lapse images that reflects the spatial-temporal concentration of the molecule. However, it is not clear yet if the protein recruitment is due to diffusion, exchange with cytoplasm, or both. For this reason, in my work I also develop a new inference method for FRAP experiment capable of discerning different types of dynamics. My analysis aims at quantifying the dynamical parameters, such as diffusion coefficient and exchange rate, by minimising the distance between the reaction-diffusion model prediction and actual data. The specificity of my approach is the use of dimensional reduction to efficiently perform computation without having knowledge of the initial bleached profile. This new method is then tested and validated on artificial data. The results show that this analysis is flexible since it can work with imperfect data, where the signal-to-noise ratio is low, the number of frames is reduced and the spatial window is restricted. Moreover, this approach can be potentially generalised to complex geometries, for instance curved surface. This versatility is well-suited for studying protein dynamics in the fission yeast cell wall. The inference method is applied to experimental data of another mechanosensor in the cell wall, Mtl2, yielding reasonable values of diffusion coefficient. Nevertheless, it still needs to be tested on real data of Wsc1 protein. Overall, this study offers novel methodologies for quantifying and understanding intricate protein dynamics within cells and tissues.

Institut Polytechnique de Paris
91120 Palaiseau, France